Spectroscopic Analysis of Red Fluorescent Proteins and Development of a Microfluidic Cell Sorter for the Generation of Improved Variants

by

Jennifer L. Lubbeck

B.S., Wake Forest University, 2007

A thesis submitted to the

Faculty of the Graduate School of the

University of Colorado in partial fulfillment

of the requirements for the degree of

Doctor of Philosophy

College of Arts and Sciences Department of Chemistry and Biochemistry

2013

This thesis entitled:
Spectroscopic Analysis of Red Fluorescent Proteins and Development of a Microfluidic Cell Sorter for the Generation of Improved Variants
written by Jennifer L. Lubbeck
has been approved for the College of Arts and Sciences Department of Chemistry and Biochemistry

_____

Prof. Ralph Jimenez

_____

Prof. Amy E. Palmer

Date _____

The final copy of this thesis has been examined by the signatories, and we find that both the content and the form meet acceptable presentation standards of scholarly work in the above mentioned discipline.

Lubbeck, Jennifer L. (Ph.D., Physical Chemistry)

Spectroscopic Analysis of Red Fluorescent Proteins and Development of a Microfluidic Cell Sorter for the Generation of Improved Variants

Thesis directed by Prof. Ralph Jimenez

The discovery of the green fluorescent protein (GFP) launched the development of a wide variety of fluorescent protein (FP) mutants whose spectral and photophysical diversity revolutionized *in vivo* imaging. The excitation and emission spectra of red fluorescent proteins (RFPs), in particular, have been ideally tuned to a window optically favorable for *in vivo* work. However, their quantum yields, photostabilities and fluorescence intermittency properties require improvement if they are to be broadly employed for low-copy or single-molecule measurements. Attempts to engineer improved RFPs often result in optimization of one photophysical property at the expense of others. We developed a microfluidic-based cytometer for screening HeLa cell-based genetic RFP-libraries simultaneously on the basis of fluorescence lifetime (a proxy for quantum yield), photostability, and brightness. Ten 532 nm excitation beams interrogate each cell in flow. The first is electro-optically modulated (30 MHz) to enable lifetime measurement with phase fluorimetry. The remaining beams act as a pulse sequence for isolating the irreversible photobleaching time constant. Optical-force switching is employed to sort cells based on any combination of the photophysical parameters. Screening with this instrument enables identification of regions of the structure that synergistically affect quantum yield and photostability and the sorting capability provides a new tool for accelerating the development of next generation RFPs.

Dedication

To all the individuals who have helped shape me into the person I am today.

Acknowledgements

I would like to acknowledge past and present friends, family, colleagues, and advisors without whom, I would not be where I am today. I would like to first thank my parents who instilled in me the value of knowledge and education from a very young age. Their support allowed me to always put my education first and obtain my undergraduate degree. They have always put me first and helped me pursue my dreams, even halfway across the country. My sister, Kristin, has given me unwavering encouragement and help, for which I am truly thankful.

A great deal of thanks is due to my past and present advisors who have shaped my career, mind, and future. I want to thank my high school chemistry teacher, Mrs. Jordan, for providing me a solid foundation in chemistry. Paramount to my early research-education was my undergraduate research advisor, Prof. Christa Colyer, who helped me learn the successes and failures of conducting research as well as helping me to navigate my way though a challenging undergraduate curriculum and applying to graduate school. I thank Prof. Bruce King for letting me try my hand at organic synthesis in his lab and introducing me to the wider chemistry community at my first national conference. I thank Prof. Tahei Tahara for allowing me to round out my knowledge of ultrafast spectroscopy in his lab and introducing me to the scientific community at the world-scale. I would also like to acknowledge my undergraduate and graduate professors who provided me with a thorough, superior knowledge of chemistry, physics, math, and biology. I have yet to feel limited by my core education and they always had extra time in their office hours to answer every last one of my questions. I acknowledge my lab, the Jiminez lab, and the Palmer lab for their support and help throughout the years and, lastly, I would like to thank my current advisors Ralph Jimenez

and Amy Palmer for supporting my work on such an amazing project. It is rare that a student finds a project and an advisor that are truly outstanding, and in this case, my project was headed by two outstanding individuals. I thank Amy for her willingness to act as my advisor whenever the occasion presented itself. I thank Ralph for providing me with the optimal graduate career in which to flourish. In his lab, as his advise, my only limitations were my own. I am grateful for his advice, guidance, and his willingness to inform and instruct as well as to let me make my own mistakes and choose my own path. I am grateful that Ralph and Amy have always had or made time for me and this project.

My friend and partner throughout this roller coaster is Kevin Dean. I could not have asked for a better collaborator. I hold him in great esteem and am grateful for our successful team and everything I have learned from him. I hope that many more shop-talks over beer lie ahead of us, even if late-night data sessions do not. I thank Geoff Bee for his support and encouragement throughout the good and bad times. Lastly, I thank my friends who helped me keep perspective throughout these past several years and celebrated the ups and downs of the pursuit of a Ph.D.

Contents

Chapter

Tables

Table

Figures

Figure

Chapter 1

Introduction

1.1 Discovery and Development of Fluorescent Proteins

The use of the green fluorescent protein (GFP) from the jellyfish, *Aequorea victoria* [1, 2], revolutionized *in vivo* imaging [3] when it was demonstrated that the GFP gene contained all of the information necessary to express and fold the fluorescent protein (FP) into a functional state in other organisms, thus making it a fluorescent reporter of unparalleled biological compatibility [1, 3, 4].

Subsequent discovery of new FPs from marine organisms other than *A. victoria* launched the evolution of FPs with a wide range of excitation-emission wavelengths and photophysical properties [5–7]. Additionally, this new fluorescent toolbox has enabled researchers to explore cellular dynamics with unprecedented spatiotemporal resolution [5–8] by genetically fusing FPs to a protein of interest and targeting them to specific regions within cells. Furthermore, genetically-encodable probes based on FPs permit the investigation of diverse analytes and enzymatic processes in living cells [8–10]. This increasing importance of new FPs has been accentuated by tremendous advances in fluorescence imaging including *in vivo* and super-resolution techniques [11–13].

The chromophores of all known FPs form autocatalytically during protein folding and consist of three contiguous amino acids which cyclize and oxidize to form the conjugated chromophore. This chromophore is attached to an α-helix which is threaded through a β-barrel (Figures 1.1 and 1.2). The β-barrel is a cylindrical structure formed from 11 β-sheets or strands that shields the chromophore from the solvent, as evidenced by the non-fluorescence of the isolated chromophore in solution [14]. The β-barrel also tunes the chromophore's photophysical properties, as will be

discussed later in detail. All FPs, with the notable exception of *A. victoria* GFP (AvGFP) and AvGFP variants, are naturally occurring dimers or tetramers, which necessitated extensive mutagenesis efforts to disrupt the oligomeric interfaces, jeopardizing the barrel integrity, to create monomers. The two main RFP families (derived from different marine organisms), the mFruits and the TagRFP-variants, originated from a tetramer (DsRed) and a dimer (eqFP578) respectively. As each oligomeric interface was broken, quantum yields and/or extinction coefficients decreased as summarized in Figures 1.3 and 1.4. The development of this photophysically-diverse but structurally-related FP family has provided researchers with a basis set to study the effects of structural changes on spectroscopic properties.

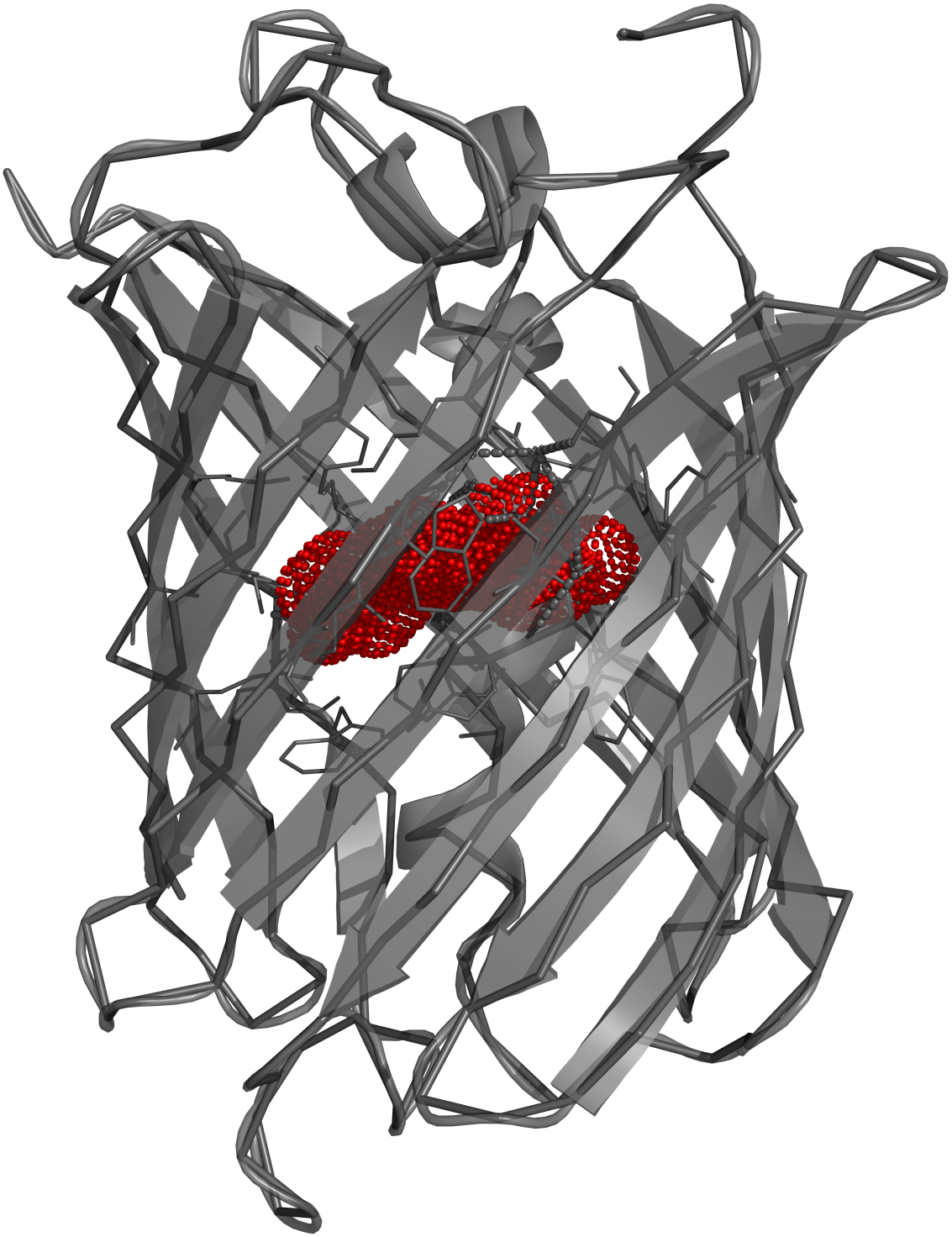

Figure 1.1: mCherry, a red fluorescent protein. The β-barrel and α-helix are depicted in grey and the chromophore in red. (PDB 2H5Q)

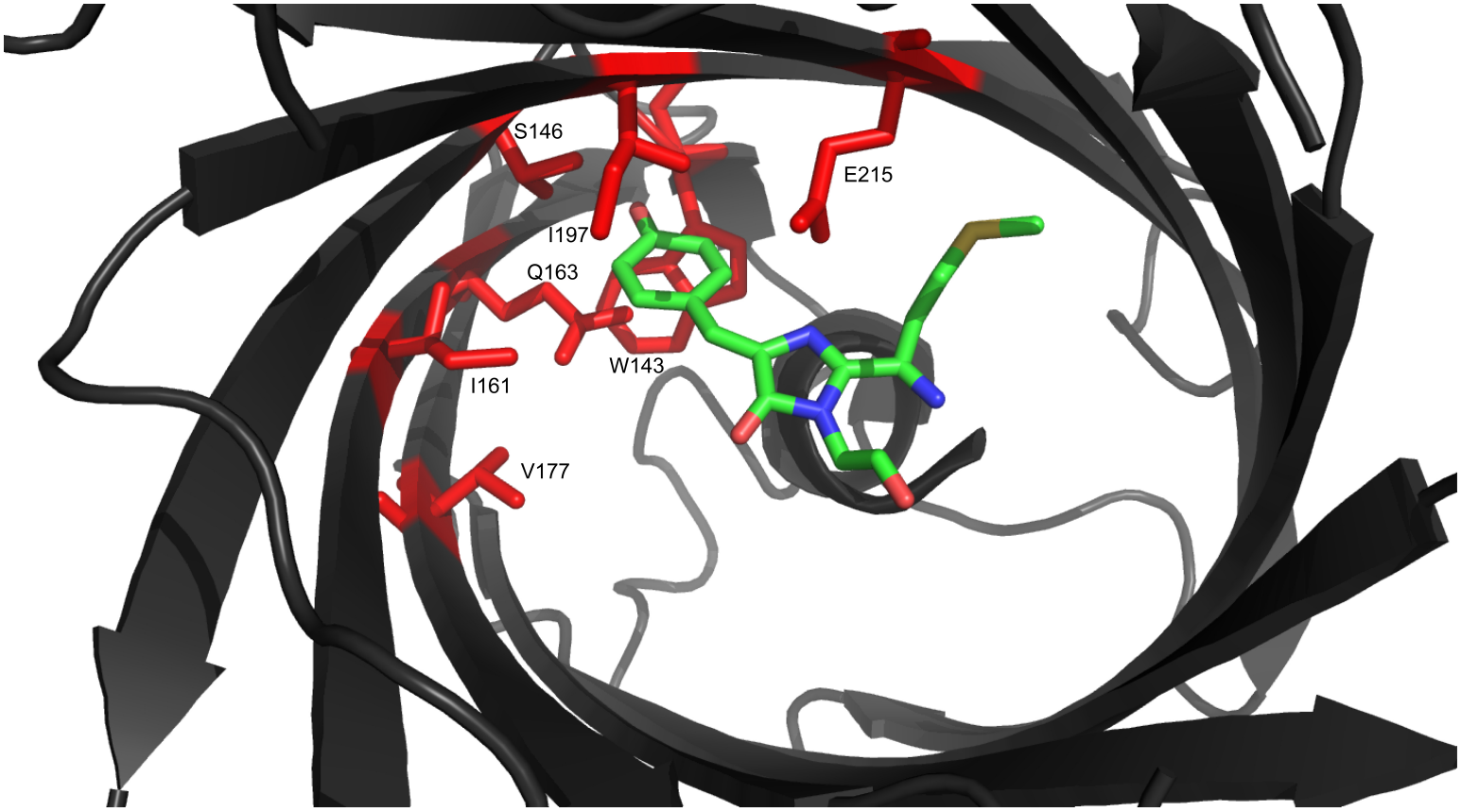

Figure 1.2: Chromophore environment of mCherry. The β-barrel and α-helix are depicted in grey and the chromophore in color where carbon is green, nitrogen is blue, sulfur is yellow, and oxygen is red. Example inward facing residues, which possibly tune the photophysics, are also depicted in red. (PDB 2H5Q)

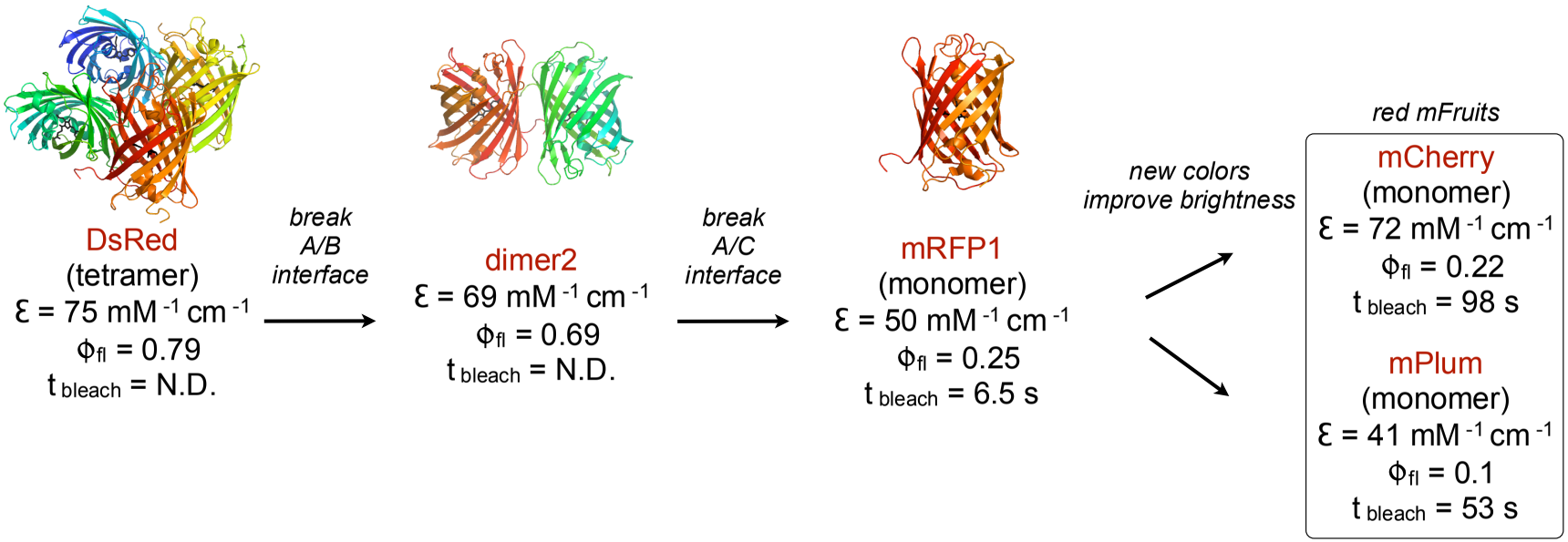

Figure 1.3: mFruit family tree. Bleaching half-lives (t_{bleach}) are reported for wide field illumination. All information is taken from references [6, 15].

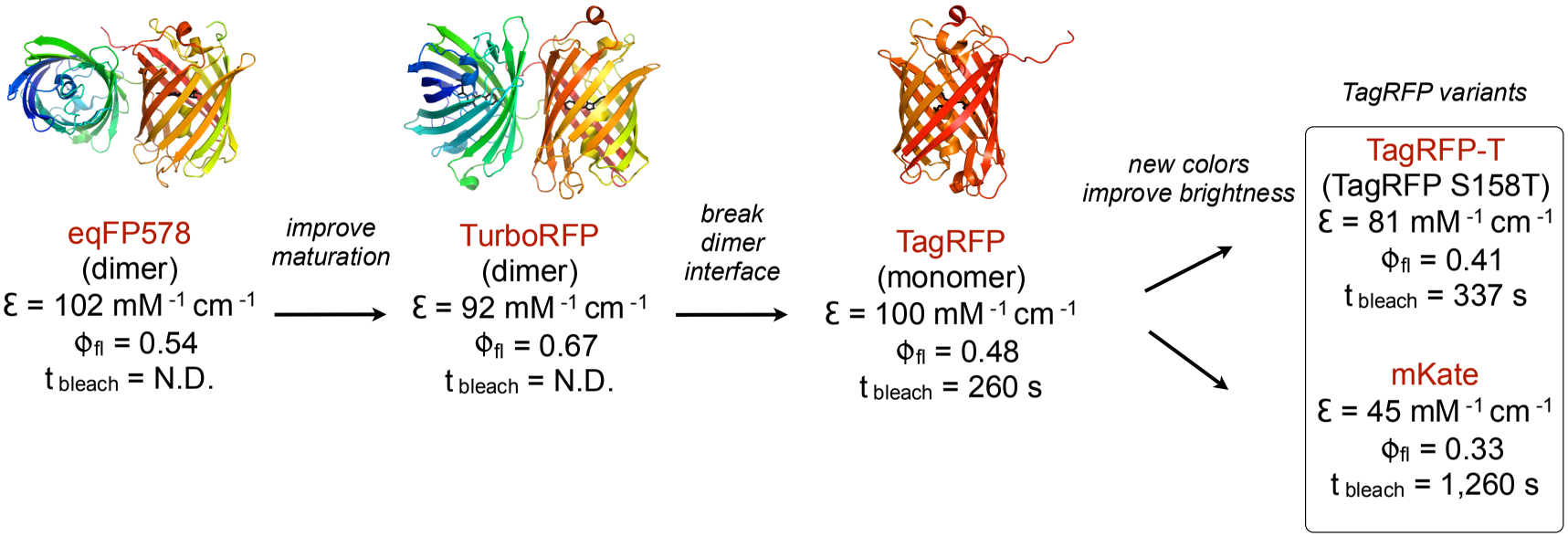

Figure 1.4: TagRFP family tree. Bleaching half-lives (t_{bleach}) are reported for wide field illumination. All information is taken from references [16–18]

1.2 Spectroscopy of Fluorescent Proteins

1.2.1 The Links Between Spectroscopy and Structure

Due to the chromophore being buried inside the barrel, the protein structure plays a crucial role in tuning the chromophore's photophysical properties. Early FP-engineering efforts resulted in significant improvements to the biochemical and optical properties of AvGFP (reviewed in [2, 19]). However, most early engineering efforts were targeted at improving maturation and folding at 37° C. Later it was established that mutations directly to, or around, the chromophore narrow the excitation spectrum, increase the extinction coefficient [20], diversify FP wavelengths (blue, cyan, and yellow) [21, 22], and reduce halide and pH sensitivity [23].

Beyond the first few solvation shells of the chromophore, the β-barrel continues to play a key role in the photophysics because it acts as a barrier between the chromophore and solvent. Protein engineering efforts to disturb the oligomeric interfaces have lead to large decreases in photostability, extinction coefficient, and quantum yield. These properties were partially restored by subsequent engineering [24, 25] and illustrate the photophysical influences of the barrel. More recently, this point has been further illustrated by directed evolution efforts of the AvGFP family by Nguyen and Daugherty. Improved versions of cyan fluorescent protein (CFP) and yellow fluorescent protein (YFP) (named CyPet and YPet) were generated using error-prone PCR and gene assembly mutagenesis [26]. Six of 7 mutations in CFP and 7 of the 11 mutations in YFP were amino acids on the outer surface of the barrel or in the loop regions that cap the barrel.

Given these unique fluorescent attributes, FPs have been the subject of intense theoretical and experimental analysis. For example, spectroscopic work on FPs has revealed an intricate chromophore environment, exhibiting excited-state proton transfer (ESPT) [27], a β-barrel mediated dynamic Stokes shift [28], and a quadratic Stark effect that shifts the absorption wavlengths of the red mFruits [29]. Despite this wealth of information, it remains poorly understood why FPs routinely emit 10-100-fold fewer photons than small-molecule fluorescent dyes [17, 30]. RFPs are of special interest as their excitation-emission maxima lie in an optically favorable spectral window of

reduced scattering and exclusive of water absorption and cellular autofluorescence. Unfortunately, RFPs especially suffer from decreased brightness and both accelerated irreversible and reversible photobleaching [8, 17, 30]. These properties limit the use of RFPs in many imaging applications that require prolonged imaging times, high excitation intensities, or low expression levels [17, 30] and are discussed in further detail below.

1.2.2 Dark State Conversion and Photobleaching

The two main mechanisms that contribute to diminished photon output are photobleaching and dark-state conversion (DSC). When single FP molecules are observed, DSC is manifested as blinking of the fluorescence intensity due to formation of a long-lived (10's of μs to minutes) dark state that temporarily removes the FP from the excitation-emission cycle [31–33]. On the ensemble level, DSC (also known as blinking or reversible photobleaching-these terms will be used interchangeably) results in decreased brightness. Reversible photobleaching is distinct from irreversible photobleaching (typically referred to as simply photobleaching), which is photodestruction of the chromophore, resulting in complete and sudden loss of fluorescence at the single molecule level and exponential decrease of fluorescence with time at the ensemble level.

In GFP and its yellow-emitting variants, two DSC processes that occur on the 0.01-1 ms timescale have been identified. One, which is pH-dependent, is attributed to protonation of the p-hydroxybenzylidene moiety and the other, which is pH-independent, is attributed to a conformational change of the chromophore and/or its environment into a non-radiative configuration [32, 34, 35]. This latter result is supported by more recent studies which reveal that blinking can be altered by changes to the immediate chromophore environment, particularly those affecting chromophore crowding (Figure 1.2). In particular, studies which examined point mutations on three positions in AvGFP revealed that increased space around the chromophore positively correlates with the magnitude of internal conversion and mutations which are designed to rigidify the chromophore impede internal conversion as determined by absorption spectroscopy, as well as steady-state and time-resolved fluorescence spectroscopy [36]. Additional crystallography and

single-molecule fluorescence studies on photoconvertable FPs show that molecular crowding and hydrogen-bonding networks influence the probability of isomerization based on the flickering rates of single molecules and the observed isomerization in the crystal structure of these proteins upon excitation [37–39].

A separate sub-μs process has been identified in GFP, likely involving intersystem crossing to the triplet state. With 100-picosecond one-photon, or 100-femtosecond two-photon pulsed excitation of GFP, an increase of the inter-pulse interval from ≈10 ns to 2 μs, to allow relaxation between pulses, leads to decreased irreversible photobleaching and an increase in the total photon yield by a factor of 5-25 [40]. In RFPs, DSC can be both pH-sensitive [37, 41] and pH-insensitive [32, 42, 43], with photophysical processes taking place on the μs (*e.g.*, the triplet state) and 0.1 ms (conformational dynamics) timescales [44].

There are multiple mechanisms by which photobleaching can occur. However a prominent mechanism in many FPs likely involves reaction with oxygen as singlet oxygen has been detected upon irradiation of GFP [44], and photobleaching is typically minimized by treatment of the sample with singlet oxygen scavengers such as sodium azide [45]. Although, as previously mentioned, the β-barrel shields the chromophore from the solvent, several studies indicate that shielding effects of the barrel are sub-optimal, especially in RFPs. For example, when EGFP was embedded in a polyelectrolyte matrix, its photostability was doubled [46]. This observation suggests that ionic screening effects decrease photobleaching by excluding diffusible ions from the chromophore. Furthermore, as mentioned above, mutations to the barrel of AvGFP and DsRed-derived proteins lead to increases in photostability, indicating that they are not optimally-shielding the chromophore [26]. Lastly, recent molecular dynamics simulations show a larger, more dynamic gap between β-strands 7 and 10 (denoted the "β-bulge") of a DsRed-derived protein (mCherry) relative to the other strands. These studies also compared the gap between mCherry's strands 7 and 10 with that of its GFP-homologue (citrine), and found it to be larger and more dynamic in mCherry than in citrine [47, 48].

The pathways and kinetics for DSC and photobleaching are poorly understood but in general

are linked. The linking of the kinetics arises because irreversible photobleaching often results from absorption of light from an excited state, such as a triplet state or a dark state. Conversion to a dark state is also found to accentuate irreversible photobleaching, but by an amount that varies for different RFPs [49]. The magnitudes and time-constants of both reversible and irreversible photobleaching depend on the fluorophore, excitation intensity, and excitation wavelength [17, 33, 49, 50].

1.2.3 Quantum Yield and Fluorescence Lifetime

Quantum yield (ϕ_{fl}) is defined as the fraction of photons radiatively emitted relative to the number of photons absorbed (Figure 1.5). The fluorescence lifetime (τ) of a fluorophore is the average time a fluorophore spends in the excited state ($S_{n>0}$) before relaxing back to the ground state. The fluorescence lifetime is directly related to the quantum yield because the lifetime determines how much time the excited-state fluorophore has to interact with its environment. Mathematically, the quantum yield and lifetime are defined as:

$$\phi_{fl} = \frac{k_{rad}}{k_{rad} + k_{nr}} \tag{1.1}$$

$$\tau = (k_{rad} + k_{nr})^{-1} \tag{1.2}$$

Where k_{rad} is the emissive rate of the fluorophore and k_{nr} is the sum of the rates of all non-radiative relaxation pathways. These equations, when combined, linearly relate the quantum yield and lifetime by:

$$\phi_{fl} = \tau \times k_{rad} \tag{1.3}$$

Small molecule dyes such as rhodamines have quantum yields approaching 1, and have the brightest emissions, where brightness is defined as the product of the quantum yield and extinction coefficient [51].

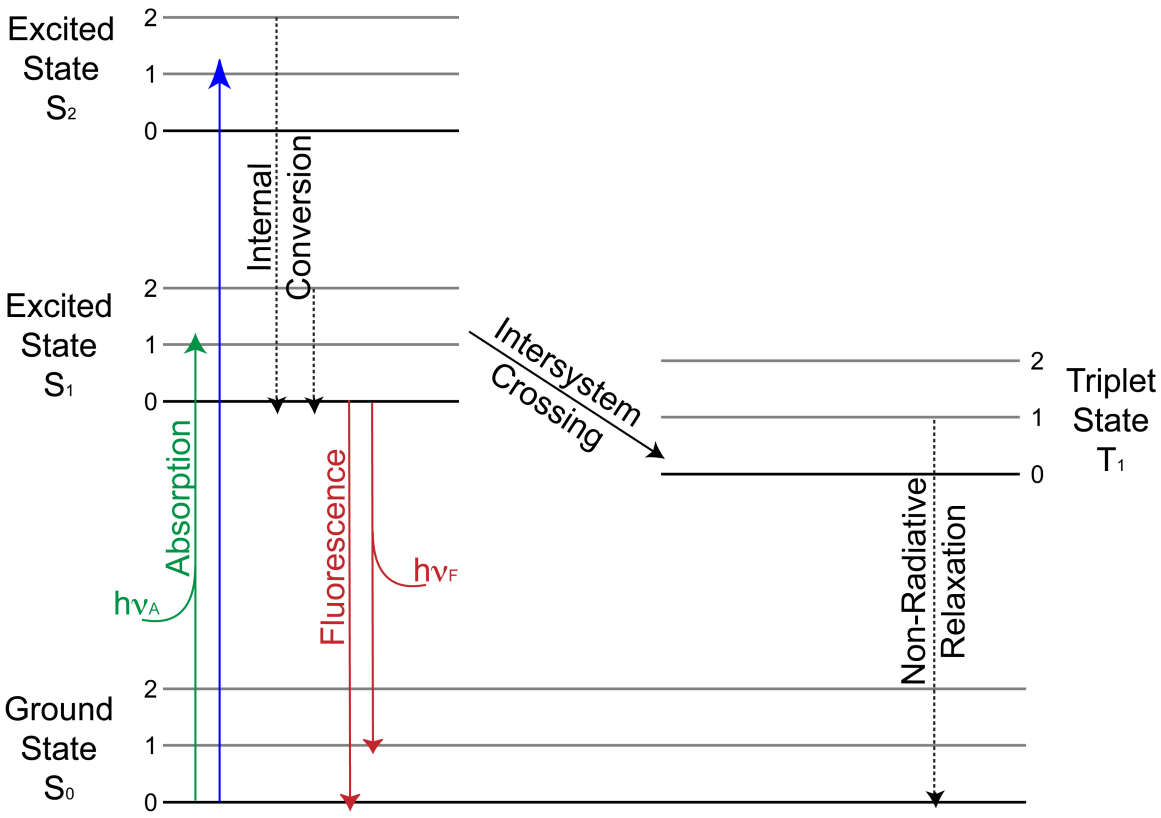

Figure 1.5: Jablonski diagram illustrating the main processes affecting quantum yield. Quantum yield is the ratio of photons radiatively emitted versus photons absorbed. Fluorescence lifetime is the average time the chromophore spends in the emissive-excited states. In addition to intersystem crossing to triplet states, other processes, such as conformational transitions or excited state proton transfer can lead to dark-state formation and, therefore, decreased quantum yield.

Although fluorescence lifetime linearly correlates with quantum yield, the longer a fluorophore remains in the excited state, the more time is available for it to undergo excited state reactions (possibly resulting in photobleaching) or collisional quenching. Consider molecular oxygen which is a known collisional quencher and photobleaching agent (as discussed above). The diffusion coefficient (D) of oxygen in water at 25° C is 2.5×10^{-5} cm^2/s. The height and diameter of the GFP barrel are approximately 40 Å and 30 Å respectively [52]. This means that the oxygen molecule can diffuse across the average of the barrel axes (Δ x = 35 Å) in 2.5 ns (t) according to the Einstein equation [51]:

$$\Delta x^2 = 2Dt \tag{1.4}$$

The fluorescence lifetimes of TagRFP and mCherry are 2.42 ns and 1.87 ns respectively [49] meaning that any increase in fluorescence lifetime (or quantum yield) would leave these proteins even more vulnerable to photobleaching or fluorescence quenching. This example illustrates why improving the photostability and quantum yield are synergistic as they both rely heavily on the permeability of the β-barrel. Furthermore, it illustrates why optimization of one parameter can result in decreases in the other parameter due to the implications of a longer or shorter lifetime.

1.3 Fluorescent Protein Development

1.3.1 Library Development

The procedures by which improved FPs are being developed have recently been reviewed [53]. A common workflow involves rational design of amino-acid replacements at key positions in the protein to influence a spectral phenotype followed by directed evolution to find combinations of residues at supporting positions to tune the photophysical properties. Usually this process is achieved by *in vitro* random mutagenesis coupled with bacterial expression and screening to isolate high-performing mutants. Alternatively, site-directed mutagenesis coupled with expression in mammalian cells automatically selects proteins readily expressible by the eukaryotic machinery

and should thus provide advantages for developing mutants with low cytotoxicity that are optimized for expression and stability within these cells [53]. Several successive rounds of mutagenesis and selection are generally required and hence selected cells must be capable of proliferation.

Our library design closely resembles that described above. We designed hypothesis-driven, targeted libraries of RFPs and expressed these libraries in mammalian cells to ensure that engineered proteins fold and mature *in vivo* at 37° C. However, previous selection strategies to improve mFruit proteins were restricted to manual screening (as discussed below) of 10^4 clones [15, 24]. To accelerate FP photostability improvements, larger library sizes are necessary. In this work, we present the development of an instrument capable of sorting hypothesis-driven libraries on the order of 10^5 clones. As an example, saturated mutagenesis on 4 residues results in $20^4 = 1.6\times10^5$ clones. However, saturated mutagenesis at just one more residue results in a library size of 3.2×10^6 clones. Therefore, some amino acid positions are chosen to be more restricted in diversity to maintain manageable library sizes. We also recognize that longer-range or synergistic effects of amino acids are difficult to predict and so error-prone libraries and additional rounds of mutagenesis between sorts are also incorporated.

1.3.2 Selection Methods

Currently, the major high-throughput screening approach in use for directed evolution is sorting of bacterial libraries using a fluorescence activated cell sorter (FACS). FACS instrumentation is limited to detection of three parameters: fluorescence intensity, wavelength, and light scatter. Suggestions for new modalities of FACS that would be useful in developing new RFPs include fluorescence emission spectrum, brightness with two-photon excitation, fluorescence polarization anisotropy, and fluorescence lifetime [53]. Further to these suggestions, the microfluidic sorter development and operation, which is presented in this thesis, provides a different and new capability that directly addresses an essential requirement for applying selection pressure to improve photostability in advanced RFPs - namely sorting of cells on the basis of reduced irreversible photobleaching, measured while minimizing the concomitant decrease in fluorescence signal from

reversible DSC.

In previous work by Tsien and coworkers, directed evolution of orange and red fluorescent proteins with increased photostability was achieved by manual selection of colonies of bacterial cells that maintained fluorescence following prolonged (10-120 min) wide-field exposure to illumination [17]. Similarly, manual sorting of *E. coli* colonies in a petri dish following fluorescence lifetime measurements has been used to screen a structure-guided library of the Cerulean FP, which has a quantum yield of ≈49%, to develop a cyan fluorescent protein with an almost 2-fold gain in fluorescent quantum efficiency [54]. While the decreasing of photobleaching could potentially yield a far larger gain in total photon signal, technology for sorting individual cells based on photobleaching has not been previously available.

It is known that mutations which improve one photophysical property of FPs often diminish another [15, 55]. Therefore, in addition to sorting cells on the basis of photostability, efforts to pursue multi-parametric sorts (which sort mutants on the basis of photobleaching and quantum yield) are also presented herein.

1.4 Conclusion

FPs have become invaluable tools in modern Biophysics and, as such, have enabled revolutionary microscopy and imaging techniques. However, to facilitate further advancements, new FPs with higher photostability and brightness must be developed. The work presented in this thesis provides us with important new tools and insight to further this goal. Throughout this project, an effort has been made to not only develop new methods and technologies to meet the challenges detailed above, but also to analyze and interpret experimental results to guide future FP and instrumentation development. In this way, the technology, as well as the proteins, is subject to its own form of directed evolution. While many more rounds of evolution are still required to achieve the next generation of fluorescent probes, this work outlines the foundation of one novel approach and discuses its strengths, weaknesses, and future directions.

Chapter 2

Analysis of Red-Fluorescent Proteins Provides Insight into Dark-State Conversion and Photodegredation

2.1 Abstract

Fluorescent proteins (FPs) are powerful tools that permit real-time visualization of cellular processes. The utility of a given FP for a specific experiment depends strongly on its effective brightness and overall photostability. However, the brightness of FPs is limited by DSC and irreversible photobleaching, which occur on different timescales. Here, we develop *in vivo* ensemble assays for measuring DSC and irreversible photobleaching under continuous and pulsed illumination. Analysis of closely related red-FPs reveals that DSC and irreversible photobleaching are not always connected by the same mechanistic pathway. DSC occurs out of the first-excited singlet state, and its magnitude depends predominantly on the kinetics for recovery out of the dark-state. The experimental results can be replicated through kinetic simulations of a four-state model of the electronic states. The methodology presented allows light-driven dynamics to be studied at the ensemble level over six orders of magnitude in time ($\mu s - s$ timescales).

2.2 Publication Status and Author Contributions

Dean, K.M., Lubbeck, J.L., Binder, J.K., Schwall, L.R., Jimenez R, and Palmer, A.E. Analysis of Red-Fluorescent Proteins Provides Insight into Dark-State Conversion and Photodegradation. Biophys. J. 2011. Aug 17; 101(4)961-9.

K.M.D., J.L.L., R.J, and A.E.P. designed the research. K.M.D. and J.L.L. performed re-

search. K.M.D. performed data analysis and numerical simulations. J.K.B. and L.R.S. provided reagents and assisted in research. K.M.D., R.J., and A.E.P wrote the paper.

2.3 Introduction

Despite work on a variety of RFPs, published models are in disagreement and provide little insight into irreversible photobleaching. As a result, it is not clear if irreversible photobleaching occurs out of transient and/or long-lived dark-states. In this chapter we analyze multiple closely related proteins to explore how diverse photophysical properties coevolve with one another. Our goal is to provide a model that combines DSC and irreversible photobleaching in the context of additional photophysical properties (quantum yield, extinction coefficient, etc.), and to shed light on how these properties change upon mutation of the protein structure.

TagRFP, and a closely-related variant, mKate, are ideal candidates for evaluating how photophysical properties vary within a series of FPs [16]. mKate was derived from TagRFP by directed evolution with selection pressure for red-shifted emission and is characterized by incorporation of 4 mutations (R67K, N143S, F174L, H197R) [16, 18]. Subsequent studies identified a single mutation in TagRFP, S158T, that improved its photostability 9-fold and is referred to here as TagRFP-T [17]. In mKate, an S158A mutation, hereafter referred to as mKate2, improved the brightness (defined as the product of the extinction coefficient and quantum yield) 2.8-fold [17, 56]. Given the limited number of mutations necessary to evaluate this pathway, its diverse phenotypes, and the sensitivity to modest structural perturbations (*e.g.*, S158T), we characterized the photophysics of this system and introduce a pulsed photoexcitation method that separately resolves the magnitudes of irreversible photobleaching and DSC.

2.4 Materials and Methods

2.4.1 *in vitro* Fluorescent Protein Characterization

TagRFP-T was cloned into pBAD and mutations were introduced using overlap extension mutagenesis. Upon commercial DNA sequencing, mutants were transformed into Top10 *E. coli*, induced with 0.02% arabinose for 24 hours at room temperature, purified using His-tag/Ni-NTA chromatography, and buffer exchanged into 15 mM MOPS, 100 mM KCl, pH=7.0. UV-Visible spectroscopy was performed in a dual-beam reference mode spectrometer with baseline correction. Excitation and emission spectra were collected for dilute fluorescent protein solutions (≈ 1 μM) on a fluorimeter and corrected for temporal and spectral lamp intensity fluctuations with a beam splitter and photodiode prior to the sample cuvette. The observed emission intensity was corrected for the wavelength dependent PMT quantum efficiency. Extinction coefficients were determined using the dynamic alkaline denaturation method which permits one to distinguish between red and immature (*i.e.*, blue, teal, and green) chromophores [57]. In all cases, an isosbestic point was observed between the red chromophore and the alkaline denatured green chromophore (λ_{abs} =447 nm, $\epsilon = 44,000$ M^{-1} cm^{-1}), and the average change in absorption was used to determine the extinction coefficient of the red chromophore [58]. Quantum yields were measured in two steps. First, the optical density was determined within a 40 mm cuvette to improve instrument accuracy for weakly absorbing solutions. The resulting solution, which had an optical density well below 0.1 per 10 mm of cuvette pathlength to minimize secondary absorption artifacts, was transferred into a clean 10 mm fluorescence cuvette and the integrated fluorescence intensity was immediately measured. All calculations included corrections for the refractive indices of solvents and were cross-calibrated using rhodamine 101 in absolute ethanol [59], and cresyl violet in absolute methanol [60], as reference standards. Experimental uncertainty was assessed from the cross-calibration of rhodamine 101 and cresyl violet, and the error was kept below 10 percent.

2.4.2 Mammalian Cell Culture

HeLa cells were cultured in minimum essential medium supplemented with Earles salts, 10% fetal bovine serum (FBS), and 1% penicillin-streptomycin. FPs were localized to the nucleus by fusing a nuclear localization signal peptide (KPKKKRKVEDA) to the C-terminus of the FP. Nuclear localized FPs in a pcDNA3 mammalian expression vector were transiently transfected using commercially available reagents 48 hours prior to imaging, and the cells were placed in HEPES-Buffered (4-(2-hydroxyethyl)-1-piperazineethanesulfonic acid) Hanks Balanced Salt Solution (HHBSS, pH 7.4) prior to all imaging experiments.

2.4.3 *in vivo* Photobleaching Measurements

To eliminate diffusion artifacts, all photobleaching measurements were performed on freely diffusing FPs within the nucleus of living adherent HeLa cells. Laser based photobleaching measurements on the microsecond timescale were performed by directing a 532 nm continuous wave (CW) laser through an acousto-optic modulator (AOM). Undesired light scattering originating from AOM optical heterogeneities were eliminated with a spatial filter, and the resulting first-order diffracted light was directed into an inverted microscope, reflected off of a dichroic mirror, and focused onto the adherent cell by a 10x, 0.40 Numerical Aperture (NA) air-objective. At the focus, the laser beam had a Gaussian profile with a full-width half-max (FWHM) of 9.1 μm, thereby completely illuminating the nucleus of the cell (diameter ≈ 5 μm). Due to the Gaussian beam waist profile, the excitation intensity at the periphery of the nucleus was 19% less than the intensity at the center of the nucleus. The resulting fluorescence emission was collected in epi-mode through the same objective, separated from the excitation light with a dichroic mirror and a long-pass filter, and detected by a red-optimized photomultiplier tube (PMT). The resulting photocurrent was converted into a voltage without any additional signal processing, and recorded using custom software. To avoid PMT saturation effects, *i.e.*, PMT blinding [61], the applied PMT voltage was decreased, enabling operation in a low-gain mode. Furthermore, the observed photophysical responses of cells did not

change with cellular brightness, and no fluorescence recovery was observed for analogous photobleaching assays performed on commercially available fluorescent beads of comparable brightness (data not shown).

Wide-field photobleaching measurements were performed on a commercial epi-fluorescence microscope equipped with a Xe arc lamp, a 540/25 excitation filter, 590 nm dichroic, and 630/60 emission filter, CCD camera, and 40x 1.3 N.A. oil-immersion objective. Wide-field measurements were performed without neutral density filters, resulting in an excitation intensity of $\approx$100 W/cm^2.

2.4.4 Photobleaching Data Analysis

To compare FPs with different excitation profiles and molar absorptivities, all photobleaching spectra were normalized for the rate of excitation. For laser-based measurements, the rate of excitation was calculated by multiplying the absorption cross-section at 532 nm with the laser intensity, defined throughout as the average laser intensity at FWHM. For wide-field photobleaching measurements, the rate of excitation was determined by integrating the product of the lamp spectral output, excitation filter transmission, dichroic reflectivity, FP excitation profile, and light intensity at the objective focus.

Laser-based photobleaching measurements at intensities of 25.0 kW/cm^2 and 2.5 kW/cm^2 were collected with 1 and 10 μs temporal resolutions, respectively, and each data set spanned 6 orders of magnitude in time. To weight the data equally and avoid a bias in subsequent exponential fits, a smoothing spline was applied to the data and values were interpolated at equally spaced log-time intervals. For each data set, a minimum number of exponentials were used to fit the data, and an optimal global fit was found after iteratively optimizing the exponential decays for the fast monoexponential ($<$ 3 ms) and slow biexponential ($>$ 10 ms) phases independently. For each fit the confidence intervals, coefficient of determination (R^2), and residuals were evaluated, and many fits showed unavoidable and minor oscillations ($<$ 3%) in the residuals. Analysis of the confidence intervals for the multiexponential fit suggested accurate time constants, yet unsatisfactory pre-exponential amplitudes for direct comparison of the fast and slow photobleaching phases. As a

result, the amplitude of the initial decrease in fluorescence intensity was determined by fitting the initial phase to a single-exponential decay with a constant offset. Subtraction of the offset from the normalized fluorescence intensity provided the amplitude of the fast process. mApple and mKate2 were excluded from analysis given their complicated photobleaching kinetics, *i.e.*, rapid DSC followed by photoactivation and subsequent photobleaching. All data analysis was performed using MATLAB.

2.4.5 *in vitro* Fluorescence Lifetime Measurements

The experimental setup used here has been described elsewhere [62]. Briefly, dilute solutions ($\approx$ 100 nM) of purified protein were excited with 1 kW/cm^2 of light originating from a diode-pumped solid-state 532 nm laser. Fluorescence was collected in the epi direction and separated from the excitation light using a dichroic mirror, focused through a 50 μm pinhole, detected with avalanche photodiodes, and binned into 1064 channels using a commercial time-correlated photon counter. All signals were background corrected, and the resulting fluorescence decay was subjected to a single or biexponential fit, and the initial 1 ns of the decay was omitted to avoid artifacts originating from deconvolution.

2.5 Results

2.5.1 Spectral Changes Associated with Mutations

To characterize the photophysical properties of a series of closely related FPs, we generated variants of TagRFP with combinations of the 4 mutations that convert TagRFP into mKate (R67K, N143S, F174L, H197R). These mutations are illustrated in Figure 2.1, which depicts the chromophore environment of TagRFP and mKate. We also incorporated additional mutations (S158A/C/T and H197I/Y) to explore the influence of these amino acid substitutions on photostability and red shift, respectively [65]. 27 proteins were generated, purified and compared to six mFruits: mApple [17], mCherry [15], mOrange [15], mOrange2 [17], mStrawberry [15], and

mPlum [66]. Table 2.1 lists the excitation and emission wavelength, extinction coefficient, quantum yield, and fluorescence lifetime measured for each protein. Not surprisingly, these parameters varied widely across the proteins and the influence of each individual mutation on the photophysical properties was strongly context dependent, (*i.e.* dependent on the other mutations present). For example, incorporation of F174L into TagRFP R67K S158T caused a dramatic reduction in the quantum yield from 0.36 to 0.04, but the same mutation introduced into TagRFP N143S S158T caused a slight increase in the quantum yield from 0.25 to 0.40.

It was previously shown that TagRFP and mKate crystal structures reveal trans and cis chromophore configurations, respectively (Figure 2.1) [56, 67], consistent with spectroscopic and electronic structure calculations that suggested trans-to-cis isomerization of the p-hydroxybenzylidene moiety into a negatively charged electrostatic environment would cause a red-shift in the excitation [68,69]. For the mutant proteins examined here, the maximum excitation wavelength generally clustered in two groups, perhaps corresponding to proteins with chromophores in either the trans or cis configuration (Figure 2.1c). However, there were proteins whose excitation spectrum exhibited a bimodal distribution (*i.e.*, Figure 2.1d, TagRFP N143S S158T), suggesting that a mixture of two chromophore configurations exist throughout the transformation of TagRFP-T to mKate2. These results suggest that the change in free energy between the cis and trans ground-state configurations may be relatively small and acutely sensitive to the mutational context in TagRFP-T variants.

2.5.2 Ensemble Photobleaching: Differentiating DSC and Irreversible Photobleaching

Photobleaching, *i.e.* the gradual decay of fluorescence upon exposure to light, significantly limits the photon output of FPs, yet the mechanisms of fluorescence decay remain poorly characterized. To examine photobleaching for a panel of FPs *in vivo*, freely diffusing, nuclear localized FPs were expressed in HeLa cells and continuously illuminated using a Xe arc lamp or continuous-wave laser. Figure 2.2 provides a representative image of FP localization and the extent of photobleaching observed. TagRFP-T mutants were selected from the previous section to include well-maturing

Table 2.1: *in vitro* Spectral Properties of Fluorescent Proteins

Fluorescent Protein	Ex/Em (nm)	Extinction Coefficient (M^{-1} cm^{-1})	Quantum Yield	Fluorescence Lifetime (ns)
TagRFP	555/579	95,000	0.48±.04	2.42
TagRFP S158T (TagRFP-T)	555/580	104,000	0.47±.08	2.71
TagRFP S158C	570/589	77,000	0.24±.01	
TagRFP S158A	556/589	70,000	0.1±. 01	
TagRFP R67K S158T	550/579	105,000	0.36±.09	
TagRFP N143S S158T	569/590	110,000	0.25±.06	
TagRFP S158T F174L	584/590	89,000	0.05±.01	
TagRFP S158T H197R	548/559	N.D.	0.45±.10	
TagRFP R67K N143S S158T	580/602	100,000	0.41±.12	
TagRFP R67K N143S S158A	578/607	120,000	0.30±.12	
TagRFP R67K N143S S158C	580/608	100,000	0.39±.16	
TagRFP R67K N143S	576/596	115,000	0.30±.10	2.36
TagRFP R67K S158T F174L	577/593	93,000	0.04±.01	
TagRFP R67K S158T H197R	556/580	N.D.	N.D.	
TagRFP N143S S158T F174L	582/594	100,000	0.40±.12	
TagRFP N143S S158T H197R	578/609	N.D.	0.17±.04	
TagRFP S158T F174L H197R	N.D.	N.D.	N.D.	
TagRFP R67K N143S S158T H197Y	589/623	72,000	0.11±.04	
TagRFP R67K N143S S158T F174L	578/601	93,000	0.34±.12	
TagRFP R67K S158T F174L H197R	576/616	N.D.	N.D.	
TagRFP R67K N143S S158T H197R	578/617	N.D.	0.20±.05	
TagRFP N143S S158T F174L H197R	580/610	N.D.	N.D.	
TagRFP R67K N143S S158T F174L H197R	566/621	77,000	0.25±.06	
TagRFP R67K N143S F174L H197R (mKate)	586/619	105,000	0.25±.02	
TagRFP R67K N143S S158C F174L H197R	583/615	115,000	0.22±.03	
TagRFP R67K N143S S158A F174L H197R (mKate2)	585/618	89,000	0.38±.16	2.79
TagRFP R67K N143S S158T F174L H197Y	588/618	100,000	0.08±.01	
mApple	569/590	88,000	0.49±N.D.	3.11
mCherry	586/606	97,000	0.16±.02	1.87
mOrange	547/562	100,000	0.67±N.D.	3.62
mOrange2	550/564	110,000	0.55±.04	3.28
mPlum	583/633	75,000	0.08±.02	
mStrawberry	575/594	98,000	0.35±.04	2.04

N.D. = Not Determined. Accurate extinction coefficient and quantum yield could not be obtained due to protein misfolding and/or lack of red chromophore formation.

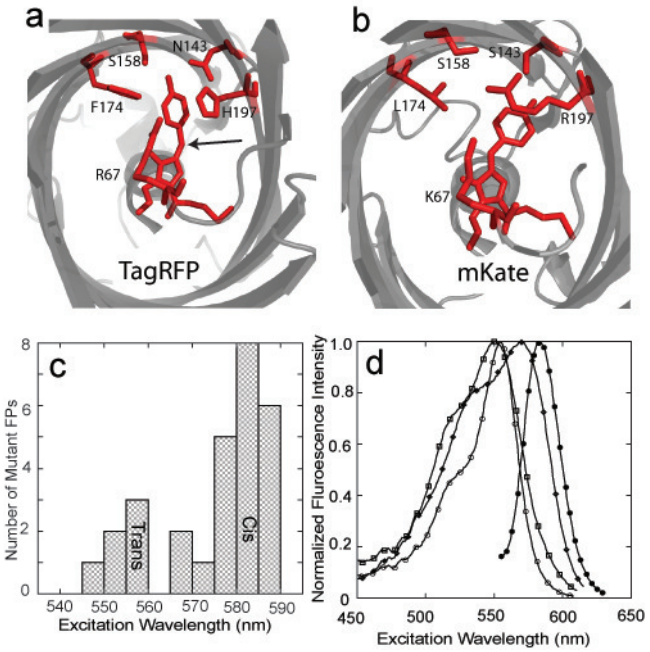

Figure 2.1: Crystal structure of chromophore pocket for TagRFP (a) and mKate (b). Crystal structures show TagRFP (PDB 3M22) and mKate (PDB 3BXB) in the trans and cis configurations, respectively, due to rotation around the bond marked by the arrow. Mutations explored in this study include R67K, N143S, S158T, S158A, F174L, and H197R. (c) A bimodal distribution of excitation wavelengths, likely indicative of a mixture of the trans and cis configurations of the chromophore throughout the transformation of TagRFP to mKate. Table 2.1 summarizes the measured extinction coefficients, quantum yields, fluorescence lifetimes, and excitation and emission wavelengths for these mutant FPs. (d) Excitation spectra of single mutants in the TagRFP-T background: TagRFP-T (open circle), TagRFP-T R67K (open square), TagRFP-T N143S (open diamond), and TagRFP-T F174L (black circle). Note the broadened excitation spectra for TagRFP-T F174L, likely indicative of two ground-state configurations, both of which absorb.

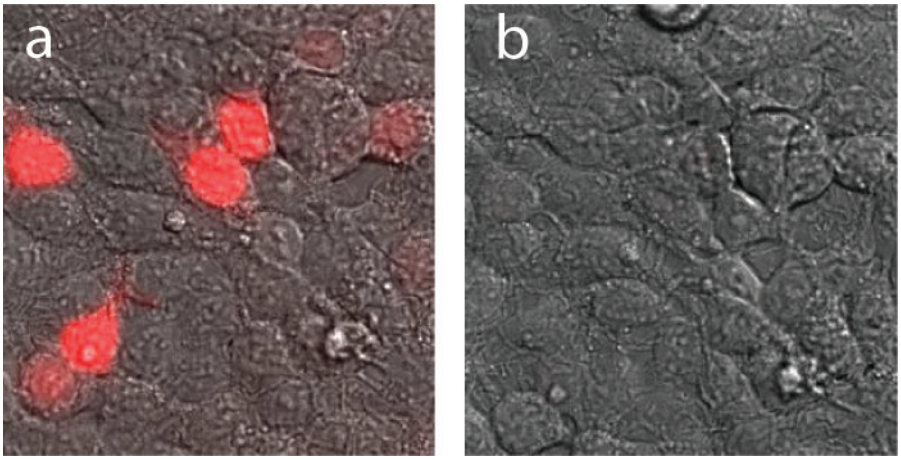

Figure 2.2: Overlay of mOrange fluorescence (red) and DIC (Differential Interference Contrast) images before (a) and after (b) photobleaching. Cells were continuously illuminated with arc-lamp illumination and the final fluorescence intensity was ≈12% of the initial fluorescence intensity. The circular shape of fluorescence image is characteristic of nuclear localization, and was observed for all FPs studied here.

variants (*i.e.*, predominantly red-absorbing) with diverse spectral properties, thereby allowing assessment of how photobleaching correlates with different photophysical attributes such as quantum yield and fluorescence lifetime.

Figure 2.3 demonstrates that the FPs exhibit a wide range of photobleaching behavior and kinetics upon exposure to either wide-field or laser (2.5 kW/cm^2 and 25 kW/cm^2) illumination. Observed responses included monoexponential decay, multi-exponential decay, photoactivation, and rapid decreases in fluorescence intensity followed by a transient increase and subsequent decay. As expected, increasing the illumination intensity led to faster photobleaching. However, there were also unexpected responses suggesting that FPs may exhibit different mechanisms of photobleaching upon wide-field vs. laser illumination or at different intensities of laser illumination. For example, TagRFP-T undergoes photoactivation with wide-field illumination (Figure 2.3a). Yet when illuminated at 25 kW/cm^2, the same protein undergoes a rapid decrease in fluorescence intensity followed by multiexponential decay with negligible photoactivation (Figure 2.3c). Figure 2.3c, inset highlights that at 25 kW/cm^2, photobleaching is characterized by a rapid decrease in fluorescence intensity during the first five milliseconds of illumination, followed by a slower decay.

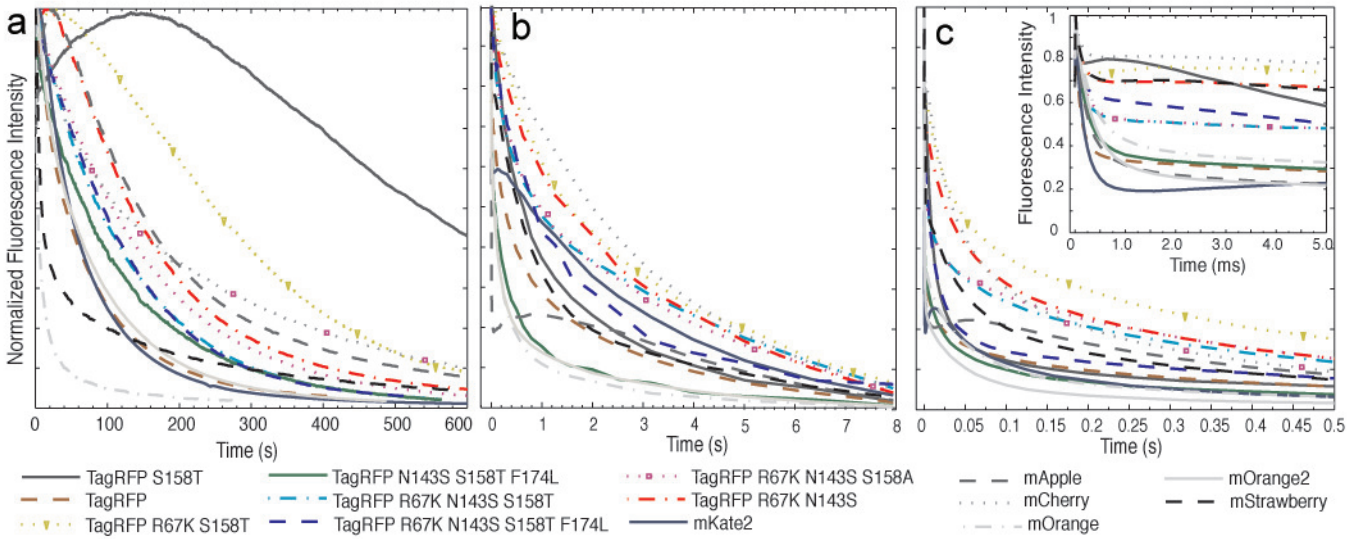

Figure 2.3: Continuous photobleaching curves were collected under (a) widefield illumination conditions (≈100 W/cm^2), (b) 2.5 kW/cm^2 and (c) 25 kW/cm^2 532 nm laser illumination. (c) Inset provides closer inspection of first 50 ms for the photobleaching decay. Each line is representative of the photobleaching observed for a single cell.

The most commonly observed behavior involved rapid decay followed by a slower decrease. Because fluorescence decay occurred over a wide range of timescales, decay curves were interpolated and converted to time points equally-spaced over six orders of magnitude in log-time. Figure 2.4a shows a typical FP fluorescence decay curve in log-time. Decay is characterized by three separate kinetic phases: an initial monoexponential decay (< 800 μs), followed by a steady-state phase (800 μs - 5 ms) where fluorescence intensity remains constant, and finally a gradual biexponential phase (>5 ms).

To gain insight into this complex behavior, photobleaching upon continuous illumination was compared to photobleaching using a train of 2 ms 25 kW/cm^2 pulses separated by 8 ms dark periods. Hereafter, we refer to this excitation scheme as pulsed. Figure 2.4b shows a characteristic photobleaching curve using pulsed excitation. The inset of Figure 2.4b demonstrates that the initial monoexponential decay phase (*i.e.*, < 800 μs) observed during continuous illumination was replicated in each excitation pulse, and was largely reversible. Accordingly, we hypothesized that this rapid decay corresponds to conversion to a transient dark state. In this context, "dark-state" means a state that is non-fluorescent, less fluorescent, less absorbing, or non-absorbing at the wavelength used (*e.g.*, the protonated chromophore, or the triplet state).

To quantify the extent of fluorescence recovery, we defined the percent recovery as (FR-FB)/(F0-FB), where F0 is the fluorescence intensity immediately after exposure to the excitation beam, FB is the final fluorescence intensity after 2 ms, and FR is the fluorescence intensity after 8 ms of recovery in the dark (Figure 2.4b, inset) [17]. The percent recovery values for each protein are listed in Table 2.2 and vary from 55 to 100%. Fluorescence recovery appeared to be complete within 8 ms, as prolonged durations in the dark (up to 10 s) did not lead to statistically significant increases in percent fluorescence recovery ($P < 0.05$, ANOVA, TagRFP, mOrange2, mCherry). However, in some cases (*e.g.*, mKate2), the percent recovery changed depending upon the number of pulse exposures, presumably due to residual dark-state accumulation.

To quantify the photobleaching of different FPs and to differentiate irreversible photobleaching from DSC, the data were fit to a sum of exponentials. The fitted rate-constants enable evalu-

Table 2.2: Percent DSC, Percent Recovery, and Irreversible Photobleaching Time-Constants Obtained under Pulsed and Continuous Illumination.

Fluorescent Protein	Percent Recovery	Percent DSC	Irreversible Photobleaching Time-Constant (ms)	DSC Time-Constant (μs)	Pulsed Photobleaching Time-Constant (ms)	Irreversible Photobleaching Time-Constant (ms)
Laser Intensity	25 kW/cm^2					2.5 kW/cm^2
TagRFP S158T	59±11 (n=3)	25±5 (n=3)	12.0±0.5 (n=3)	29±4 (n=3)	74±7 (n=3)	550±100 (n=3)
TagRFP	83±5 (n=3)	69±7 (n=3)	10.8±0.4 (n=3)	73±17 (n=3)	113±12 (n=2)	385±80 (n=3)
TagRFP R67K S158T	72±11 (n=3)	29±2 (n=3)	80.9±0.9 (n=3)	48±4 (n=3)	470±150 (n=2)	1700±110 (n=3)
TagRFP R67K N143S S158T	82±11 (n=3)	45±3 (n=3)	40.0±1.0 (n=3)	118±22 (n=3)	82±17 (n=2)	936±160 (n=2)
TagRFP N143S S158T F174L	83±4 (n=3)	68±3 (n=3)	14.8±0.9 (n=3)	173±3 (n=3)	98±9 (n=2)	225±4 (n=2)
TagRFP R67K N143S S158T F174L	77±4 (n=3)	46±3 (n=3)	16.0±2.0 (n=3)	99±3 (n=3)	81±9 (n=2)	801±27 (n=3)
TagRFP R67K N143S S158A	85±1 (n=3)	50±2 (n=3)	34.0±3.8 (n=3)	132±11 (n=3)	98±31 (n=2)	654±192 (n=X)
TagRFP R67K N143S	85±3 (n=2)	34±4 (n=2)	50±13 (n=3)	101±8 (n=3)	253±45 (n=2)	1167±150 (n=2)
TagRFP R67K N143S S158A F174L H197R (mKate2)	102±2 (n=3)	79±1 (n=3)	N.D.	187±29 (n=3)	236±72 (n=3)	N.D.
mApple	55±5 (n=3)	77±3 (n=3)	N.D.	N.D.	N.D.	N.D.
mCherry	88±5 (n=3)	18±3 (n=3)	57.0±4.6 (n=3)	73±29 (n=3)	744±35 (n=2)	3457±670 (n=3)
mOrange	90±1 (n=3)	70±10 (n=3)	1.27±2.0 (n=3)	147±89 (n=3)	183±9 (n=2)	229±170 (n=2)
mOrange2	80±5 (n=3)	74±2 (n=3)	0.96±0.2 (n=3)	180±14 (n=3)	212±13 (n=2)	262±74 (n=2)
mStrawberry	88±4 (n=3)	30±1 (n=3)	9.68±0.4 (n=3)	79±34 (n=3)	296±25 (n=3)	719±400 (n=3)

Reported error is the standard deviation, and n represents the number of measurements performed for each FP. DSC was measured at 25 kW/cm^2 and was determined by fitting the initial fluorescence decay to an exponential decay with a y-offset. Irreversible photobleaching was determined after fitting the entire decay to a triexponential fit, and is reported as the weighted average of the two slow components. Pulsed photobleaching was found by locating the peak fluorescence intensity of each excitation pulse and fitting these to an exponential decay. N.D. = Not Determined. Rapid decrease and subsequent transient increase in fluorescence intensity prohibited accurate fitting by a sum of three exponentials.

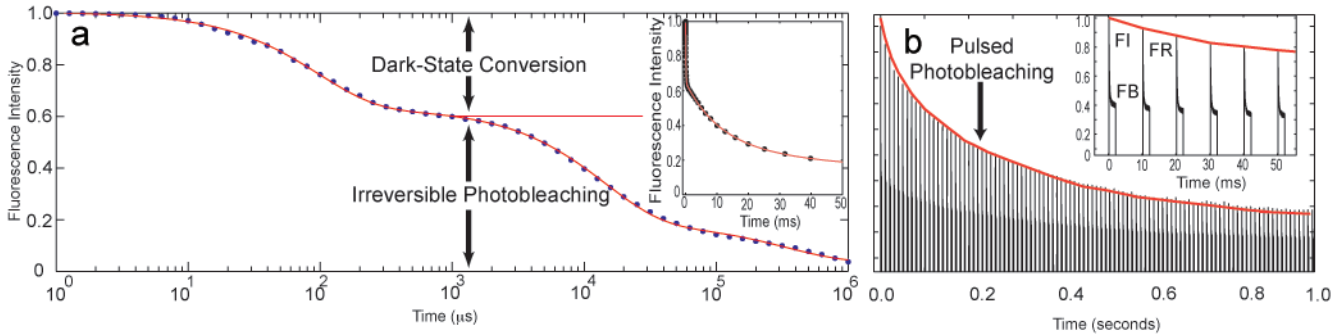

Figure 2.4: (a) Photobleaching kinetics and respective triexponential fit (red) in log-time. Initial decay representative of DSC (*i.e.*, < 1 ms), steady-state plateau (*i.e.*, $\approx$1 ms), and irreversible photobleaching phase (*i.e.*, > 5 ms) (a) inset, photobleaching kinetics plotted in linear-time. (b) Pulsed photobleaching kinetics, shown as a red line, is defined as the exponential decay of the peak fluorescence intensity of each pulse under pulsed excitation. (b) inset, percent recovery after 2 ms excitation and 8 ms in the dark. Percent fluorescence recovery is defined as (FR-FB)/(FL-FB), where FL and FR are defined as the fluorescence intensity of the initial and second pulse, respectively; and FB is the final fluorescence intensity after 2 ms of excitation.

ation of the time constants (defined as the reciprocal of the rate constant) for the different phases of fluorescence decay. At 25 kW/cm^2, continuous photobleaching data were fit to a sum of three exponential decays, allowing the kinetics of the fast and the weighted average of the slow biexponential phase to be independently determined. A representative fit is shown in Figure 2.4a. Because our pulsed excitation suggested the initial fast decay was largely reversible, this phase is referred to as DSC. To evaluate the effect of the cellular environment on the observed photophysics, we measured the kinetics and percent DSC for a representative FP (mCherry) *in vitro*. Interestingly, relative to our *in vivo* data, DSC increased 7% *in vitro*, presumably due to environmental factors. Furthermore, we compared the kinetics and percent DSC with published results from fluorescence correlation spectroscopy (FCS) on the same protein [37], and further discrepancies were attributed to difficulties in differentiating reversible and irreversible fluorescence fluctuations in FCS (For a detailed discussion, see mCherry Analysis, below). Conversely, the second slower phase appeared to be irreversible and hence is referred to as irreversible photobleaching. Table 2.2 summarizes parameters obtained from the fits of 14 different proteins including the amplitude of DSC (defined as % of the total decay attributable to DSC), as well as the time constants for DSC and irreversible photobleaching for FPs exposed to 25 kW/cm^2. Besides a small decrease in fluorescence intensity (≈1-4%) at 10 ms, no convincing evidence of triplet state dynamics was observed. At 2.5 kW/cm^2, the steady-state plateau was less pronounced, and thus the more gradual part of the photobleaching was fit to a biexponential decay (weighted time constant presented in Table 2.2). Under wide-field conditions, the three phases were not broadly identifiable and consequently, these data were not fit using this approach.

To quantitatively assess whether photobleaching occurs out of transient dark-states, photobleaching assays were also performed under pulsed excitation conditions. For each FP, the time constant of irreversible photobleaching was determined for pulsed excitation conditions by locating the maximum fluorescence intensity (*i.e.*, FR) for each excitation pulse and fitting the decrease in peak fluorescence intensity to a monoexponential decay (*i.e.*, red curve, Figure 2.4b, and inset). Hereafter, the results from this kinetic analysis are referred to as the pulsed irreversible photobleach-

ing time-constant, and the values are presented in Table 2.2. For all FPs studied, photobleaching under pulsed excitation is slower than photobleaching under continuous illumination. The extreme cases are mCherry, which exhibits a 13-fold gain in the photobleaching time-constant under pulsed illumination, and TagRFP R67K N143S S158T which only undergoes a 2-fold gain. This result suggests that for some FPs, irreversible photobleaching from dark-states is minimized by pulsed excitation, when the pulse separation is sufficient for these states to depopulate between excitation pulses.

2.5.3 mCherry Analysis

Using the rapid-photobleaching methodology discussed in the above, we measured 18% DSC for mCherry *in vivo* using 532 nm CW illumination at 25 kW/cm^2. This is in contrast to measurements performed by Hendrix et al., where they found a 46% DSC for mCherry *in vitro*, using 543 nm CW illumination at 24 kW/cm^2 [37]. Prompted by the apparent discrepancy between our mCherry data and that by Hendrix et al., we performed rapid photobleaching and DSC assays on purified mCherry *in vitro*. To facilitate comparison, we prepared fresh protein under identical buffer conditions as Hendrix et al. (Phosphate Buffered Saline, pH=7.4, 50:50 v/v glycerol), and localized freely diffusing protein within aqueous microdroplets inside of an insoluble octanol organic phase [70, 71]. To test if glycerol changed the observed DSC, samples were prepared with and without glycerol. Importantly, no statistically significant difference (two-tailed t-test, P=0.83) was observed between samples that contained glycerol (25.4% DSC, n=11) and those that did not (25.1%, n=10). Interestingly, the percent DSC did change from 18% (n=3) *in vivo* to 25% (n=21) *in vitro* (two-tailed t-test, P=0.0003), perhaps owing to changes the local environment.

Nevertheless, the 7% increase in DSC upon going from an *in vivo* to an *in vitro* environment could not entirely describe the observed percent DSC reported by Hendrix et al. Furthermore, the change in excitation intensity and excitation wavelength seems unlikely to account for the remainder of the discrepancy. Consequently, we attribute the remainder of this to artifacts arising from FCS analysis [72–74]. More specifically, FCS does not differentiate between fluorescence fluctuations

due to reversible or irreversible processes, unless they occur on largely disparate timescales.

To test this hypothesis quantitatively, we calculated the expected irreversible photobleaching that could occur during the transit time through the excitation beam in FCS. For example, Hendrix et al., report that an apparent diffusion coefficient of 56 μm^2 s^{-1}, which according to the Einstein-Stokes relation (Equation 2.10), predicts a hydrodynamic radius of 3.89 nm for mCherry. Here K_b is the Boltzmann constant, T is the temperature, η is the solvent viscosity (1.002 mPa s for water at 20° C, and 8.4 mPa s for 50:50 v/v water glycerol mixture at 20° C), D is the diffusion coefficient, and r is the hydrodynamic radius.

$$r = \frac{K_b T}{6\pi\eta D} \tag{2.1}$$

Assuming diffraction limited excitation and collection volume for FCS, the lateral (Equation 2.11) and axial dimensions (Equation 2.12) of the excitation volume at full width and half maximum (FWHM) are approximately 200 and 500 nm, respectively [11]. Here, λ is the wavelength of light, n is the refractive index of the immersion liquid (water = 1.33), and α is the angle for which the objective can collect light (66° for a 1.2 numerical aperture objective)

$$d_{lateral} = \frac{\lambda}{2n\sin(\alpha)} \tag{2.2}$$

$$d_{axial} = \frac{\lambda}{n\sin^2(\alpha)} \tag{2.3}$$

Under these conditions, the transit time for a single FP through the excitation volume can be estimated using Brownian diffusion (Equation 2.13).

$$t = \frac{x^2}{2D} \tag{2.4}$$

Using the aforementioned hydrodynamic radius of mCherry (3.89 nm), and the viscosity of a 50:50 v/v glycerol water solution (8.4 mPa s), this equation dictates that it takes, on average, 3.7 and 19.2 ms to travel through the excitation volume in the lateral and axial directions, respectively.

Using our measured irreversible photobleaching time-constant for mCherry of 57 ms, we predict that 6.3% of the molecules traversing the beam in the lateral direction will undergo irreversible photobleaching, and 28.6% for those traversing the axial direction. This observed photobleaching is even more problematic for FPs with accelerated photobleaching, including mStrawberry (9.77% and 41.34%), and mOrange (97.5% and 100%).

Indeed, this is consistent with our observation that mCherry undergoes irreversible photobleaching within the first 2 ms of pulsed excitation (See Table 2.2, and Figure 2.4b). Combining these values with the observed increase in DSC upon going from *in vivo* to *in vitro* conditions (18 to 25%), in addition to subtle excitation wavelength effects, we infer that the remaining 20% of DSC observed by Hendrix *et al.* results from irreversible photobleaching. Lastly, this is also consistent with the observation that Hendrix *et al.* observed relaxation longer time-constants (98.6 ms) than ours (73 ms) as this likely represents a weighted average of the time-constants for irreversible photobleaching dark-state relaxation.

2.5.4 Comparison of Irreversible Photobleaching in FP Variants

Measurement of photobleaching in a panel of FPs under different illumination conditions allowed us to identify general trends and hence common themes in fluorescence decay. Figure 2.5a compares the irreversible photobleaching time-constant under continuous illumination at 2.5 and 25 kW/cm^2. Overall, time constants at 2.5 kW/cm^2 were significantly greater than at 25 kW/cm^2, indicating a slower rate of fluorescence decay at lower intensity illumination. In general, the time constants were correlated so that FPs that were more susceptible to photobleaching at 2.5 kW/cm^2 were also more susceptible at 25 kW/cm2 (see mOrange and mOrange2). However, some FPs showed heightened sensitivity to increases in excitation intensity. For example, mCherry was 30 percent less photostable than TagRFP R67K S158T at 25 kW/cm^2 but 2-fold more photostable at 2.5 kW/cm^2. This observation points to a need for understanding photostability in terms of photexcitation rates relative to timescales of excited-state population transfer. Figure 2.5b compares the photobleaching time constant for pulsed *vs.* continuous illumination at 25 kW/cm^2.

Here, the two parameters are poorly correlated amongst the proteins tested, suggesting that some proteins undergo gains in photostability when subjected to pulsed excitation whereas others do not. For example, although mCherry is less photostable than TagRFP R67K S158T under continuous illumination at 25 kW/cm^2, it becomes more photostable when subjected to pulsed excitation at the same intensity.

2.5.5 Comparison of Dark-State Conversion in FP variants

Figure 2.6a presents a comparison of the percent DSC (*i.e.*, the fast reversible phase of photobleaching under continuous illumination) vs. irreversible photobleaching time constant (*i.e.*, the slow and irreversible phase under continuous illumination) at 25 kW/cm^2. For these FPs, as the percent DSC increases the photobleaching time constant decreases (correlation provided with dashed line), suggesting that as DSC increases, the propensity to photobleach also tends to increase (as observed for mOrange, mOrange2, TagRFP, etc.). However there are significant exceptions. For example, a single mutation in TagRFP, S158T, solely affects DSC (Figure 2.6a, Arrow 1), whereas incorporation of R67K into TagRFP S158T, exclusively modulates irreversible photobleaching (Figure 2.6a, Arrow 2). Conversely, some mutations simultaneously modulate both DSC and irreversible photobleaching rates (Figure 2.6a, Arrow 3).

To examine the effect of excited state lifetime on DSC, the fluorescence lifetimes of purified proteins (Table 2.1) were compared to the observed DSC kinetics for FPs in cells. Figure 2.6b reveals a correlation between increasing fluorescence lifetime and increased percent DSC. At 25 kW/cm^2, depending upon the absorption cross-section, on average one photon is absorbed every 40-80 ns (see Materials and Methods), suggesting that transient absorption out of the first excited singlet state is unlikely. Furthermore, the radiative rate, as estimated from the fluorescence quantum yield and lifetime ($\phi_{fl} = \mathrm{k}_{rad} \times \tau_{fl}$), was found to be independent of the mutational context. These results suggest that DSC is competitive with radiative decay from the first excited singlet state. Consequently, FPs exhibiting the longest fluorescence lifetimes, and hence those with the greatest percent DSC and propensity to undergo irreversible photobleaching, also tended to have the largest

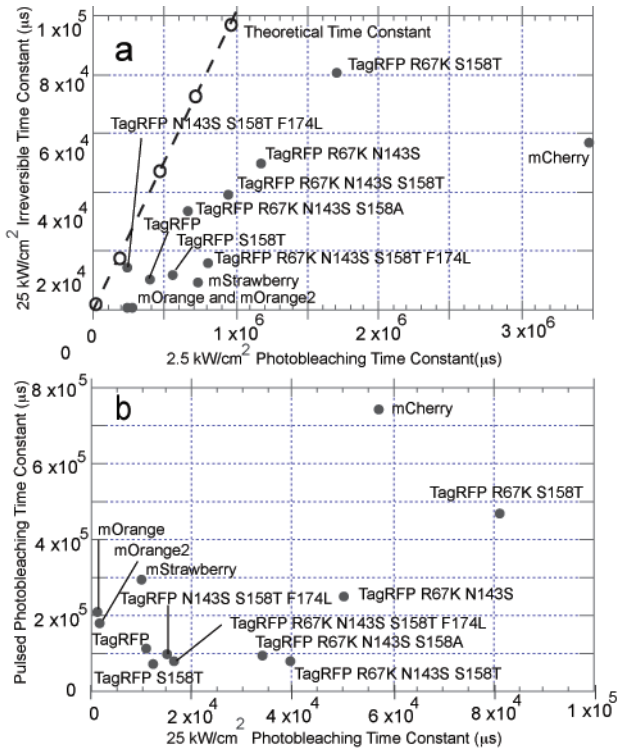

Figure 2.5: (a) Correlation between irreversible photobleaching time constants at 2.5 kW/cm^2 and 25 kW/cm^2 laser illumination shows that different proteins have different sensitivities to heightened excitation rates, and the rank-order of photostability changes with intensity. Dashed-line shows anticipated correlation for a simple 3-state system (*e.g.*, ground, excited, and bleached) where 10-fold increases in excitation intensity result in 10-fold decrease in the photobleaching time-constant. (b) Comparison of the irreversible photobleaching time constant obtained for continuous vs pulsed illumination. Under pulsed illumination, FPs with photoreactive dark-states become more photostable, whereas FPs with photoprotective dark-states do not.

quantum yields (see Relationship between quantum yield and DSC in Materials and Methods for detailed discussion).

As mentioned previously, both the amplitude and kinetics of DSC varied substantially for different FP variants. Figure 2.6c compares the time constant versus percent DSC for different FPs. Interestingly, this comparison revealed that RFPs with a slower rate of DSC, hence those that reach the steady-state phase of photobleaching more slowly, had a greater percent DSC. This observation will be explained by the kinetic modeling (below).

2.5.6 Kinetic Modeling

Careful examination of the RFP photobleaching behavior at 25 kW/cm^2 revealed clear trends between the percent DSC, the measured rate of DSC, the fluorescence lifetime, and the measured rate of irreversible photobleaching. Given these observations, we sought to expand upon existing models for DSC, to see if we could quantitatively replicate the trends observed, and if so, gain additional insight into the mechanisms of DSC and irreversible photobleaching. Previously, Dickson et al. proposed a four-state model consisting of two anionic and two neutral chromophore states to describe the blinking of yellow-emitting GFP variants at the single-molecule level [31]. Here, we perform numerical simulations on an analogous 4-state system consisting of two bright-states (S_0 and S_1) and two dark (or less-fluorescent) states (D_0 and D_1). In the context of RFPs, dark-states likely represent a mixture of neutral (non-absorbing at 532 nm) and/or isomerized (absorbing at 532 nm) chromophore states. A schematic of this model is presented in Figure 2.7a. The rates input into the kinetic simulations are referred to as microscopic, the rates measured by fitting the results from the numerical simulations are referred to as the simulated time-constant. In contrast, kinetic analysis from experimental data is referred to as measured.

All simulations discussed here were performed with a commercially available kinetic analysis software package. Simulations involving continuous laser illumination were modeled using Runge-Kutta analysis [63]. All numerical simulations were treated with mass-action kinetics, and can be summarized with the following coupled differential equations:

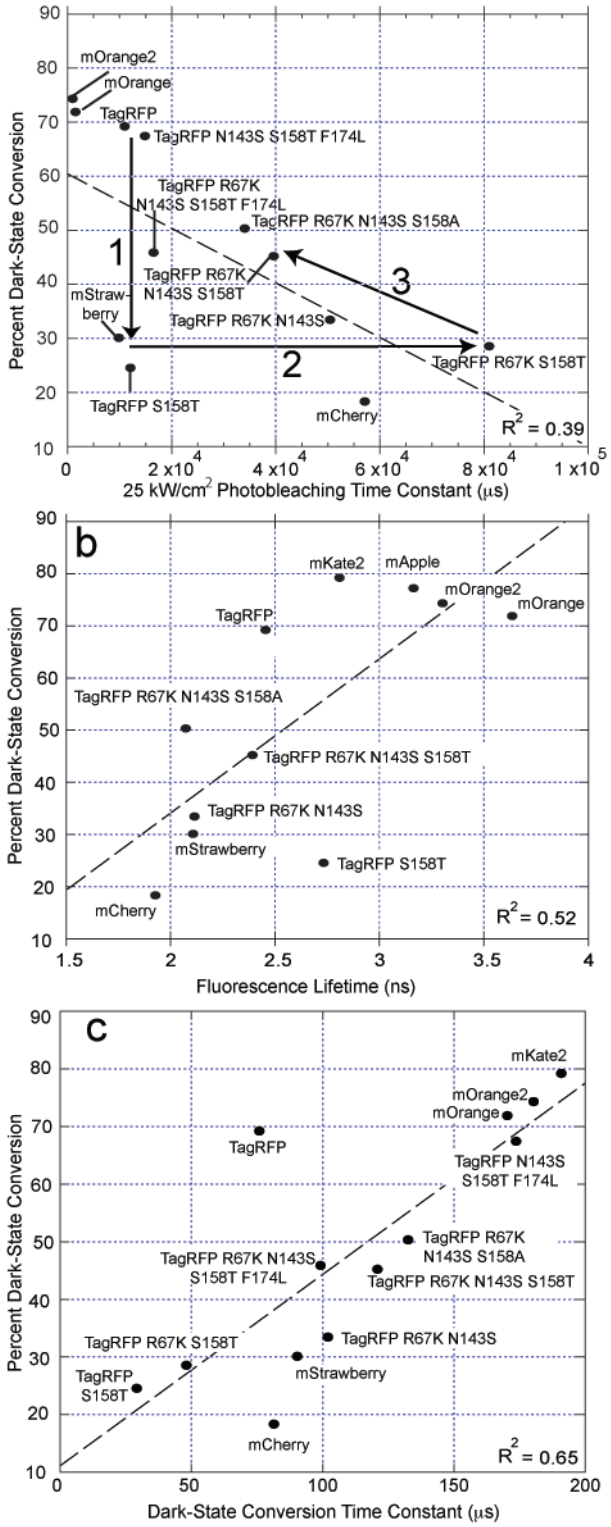

Figure 2.6: (a) Single mutations perturb the percent DSC (arrow 1), irreversible photobleaching time-constant (arrow 2), or both parameters simultaneously (arrow 3). A weak correlation (dashed line) suggests that increases in the percent DSC are accompanied by decreased photostability. (b) Comparison of the percent DSC versus fluorescence lifetime suggests that DSC is competitive with emission from the first excited singlet state. (c) Percent DSC versus the time-constant of DSC. Linear correlation reveals that the percent DSC increases in proteins with slower rates, or larger time-constants, of DSC.

$$\frac{d[S_0]}{dt} = -kS_{0ex}[S_0] + k_{em}[S_1] + k_{dsr}[D_0] \tag{2.5}$$

$$\frac{d[S_1]}{dt} = kS_{0ex}[S_0] - kS_{1B}[S_1] - k_{em}[S_1] - kS_1D_1[S_1] + kD_1S_1[D_1] \tag{2.6}$$

$$\frac{d[D_1]}{dt} = kS_1D_1[S_1] - kD_1S_1[D_1] - kD_{1B}[D_1] - k_{ic}[D_1] + kD_{0ex}[D_0] \tag{2.7}$$

$$\frac{d[D_1]}{dt} = -k_{dsr}[D_0] + k_{ic}[D1] - kD_{0ex} \tag{2.8}$$

All calculations for the excitation rate (k_{ex}) were obtained from the Beer-Lambert law. Here, light intensity, I, decreases in magnitude with respect to distance x as it passes through a solution containing n molecules per cm^3 with an absorption cross-section in cm^2 [51].

$$\frac{dI}{dx} = -I\sigma n \tag{2.9}$$

Using the conditions $I=I_0$, and x=0 cm, integration results in Equation 2.6, the Beer-Lambert law, where D is the path length for light absorption in centimeters:

$$\ln\left(\frac{I_0}{I}\right) = \sigma n D \tag{2.10}$$

Equation 2.7 is another form of the Beer-Lambert law where ϵ is the decadic molar extinction coefficient (M^{-1} cm^{-1}), C is the molar (mol/L) concentration, and D is the path length for light absorption.

$$\log\left(\frac{I_0}{I}\right) = \epsilon C D \tag{2.11}$$

Combining Equation 2.6 with Equation 2.7 allows one to relate the experimentally measured decadic molar extinction coefficient to the absorption cross-section for a single-molecule in terms of cm^2, where the factor of 2.303 results from the log/natural log conversion, and the factor of 1,000 accounts for the conversion between milliliters (cm^3) and liters.

$$\sigma = 2.303 \times 1000\left(\frac{\epsilon}{N}\right) \tag{2.12}$$

Multiplication of the absorption cross-section in cm^2 with the laser intensity in W/cm^2 gives the total joules per second absorbed, which is converted into photons absorbed per second (k_{ex}) using the relationship between Plancks constant ($h = 6.626068 \times 10^{-34} Js$) and the speed (c) and wavelength (λ) of light.

$$k_{ex} = \frac{\sigma I \lambda}{hc} = 2.303 \times 1000 \left(\frac{\epsilon I \lambda}{Nhc} \right) \tag{2.13}$$

For the FPs studied here ($\epsilon \approx$ 100,000 M^{-1} cm^{-1}), this gives a maximum excitation rate of 2.5 $\times$ 10^7 s^{-1}, or on average 1 photon every 40 nanoseconds. Due to off-peak excitation, the actual excitation rates are likely to be $\approx$ 4-fold slower. Rates for emission (k_{em}), conversion from S_1 to D_1 (kS$_1$D$_1$), conversion from D_1 to S_1 (kD$_1$S$_1$), D_1 internal conversion (k_{ic}), and ground-state recovery (k_{dsr}) were, 2.5$\times 10^8$ - 1$\times 10^{10}$ s^{-1}, 5$\times 10^5$ s^{-1}, 0 - 5$\times 10^5$ s^{-1}, 1$\times 10^9$ - 1$\times 10^{12}$ s^{-1}, and 1$\times$10 - 1$\times 10^6$ s^{-1}, respectively. Photobleaching out of S_1 (kS$_{1B}$), and D_1 (kD$_{1B}$), were varied between 10 and 10^8 s^{-1}. Pulsed illumination was analyzed using a suite of nonlinear and differential and algebraic solvers (SUNDIALS) [64]. Here, the rate of excitation was provided with a Fourier series, $(3 \times 10^7 + 2.5 \times 10^7 \times (4/\pi) \times \Sigma(1/n) \times \sin([n \times \pi \times t]/L)$, where t is time, L is the duration of the pulse in seconds and n is number of odd integer harmonics. To compare the effects of pulsed versus continuous illumination, numeric modeling was performed in the presence (two-way) or absence (one-way) of dark-state excitation. For two-way simulations, kD$_{0ex}$ was arbitrarily set to equal kS$_{0ex}$, as was kS$_1$D$_1$ and kD$_1$S$_1$. For one-way simulations, kD$_{0ex}$ and kD$_1$S$_1$ were set equal to zero.

In this four-state model, absorption of a photon (*i.e.* electronic transition from S_0 to S_1) is followed by depopulation through emission of a photon (k_{em}), non-radiative internal conversion, or a low quantum-efficiency (ϕ_{dsc}=1$\times 10^{-3}$, kS$_1$D$_1$ $\approx$ 5$\times 10^5$ s^{-1}) [42] conversion to the weakly or non-radiative D_1 state. D_1 can decay to D_0 (k_{ic}), which can subsequently be converted back to S_0 (k_{dsr}). In accordance with Dickson et al., recovery from D_0 to S_0 was assumed to be rate limiting (26). As shown in Figure 2.7b, variation of the microscopic time constant for dark state recovery, τ_{dsr} from 1-500 μs altered the populations of the S_0 ground state and D_0 dark state (*i.e.* the percent

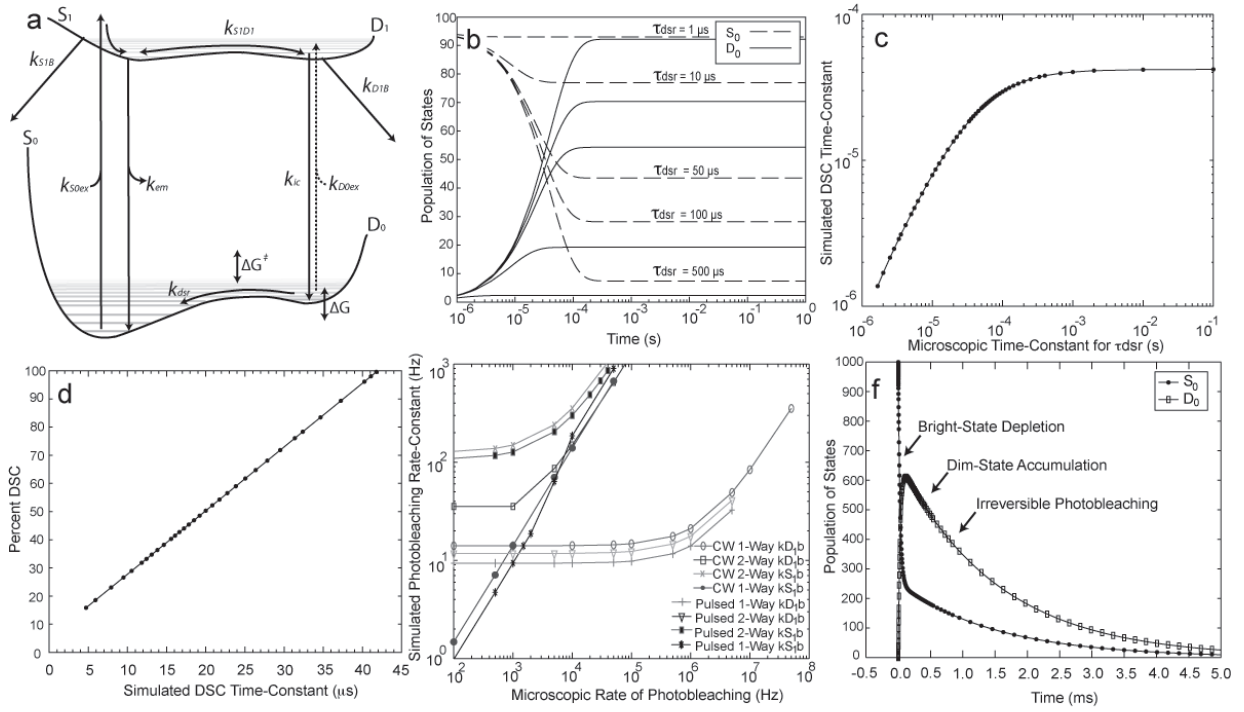

Figure 2.7: (a) Four state model includes the rate of excitation (kS_{0ex}), fluorescence emission (k_{em}), conversion from S_1 to D_1 (kS_1D_1), internal conversion from D_1 to D_0 (k_{ic}), and dark-state recovery (k_{dsr}). Photobleaching was incorporated out of both S_1 (kS_{1B}) and D_1(kD_{1B}). In some FPs, dark-state excitation (kD_{0ex}) is included, and D_1 may be weakly fluorescent. (b) The influence of dark-state recovery kinetics on S_0 depletion at 25 kW/cm^2. As the microscopic time-constant for dark-state recovery (τ_{dsr}) increases, the S_0 state is depleted and a significant increase in the D_0 population is observed. (c) Microscopic time-constant of dark-state recovery vs the time-constant obtained by fitting the simulated DSC. At fast time-scales, the measured time-constant of DSC accurately reflects the time-constant of ground-state recovery, with increasing deviations observed for FPs with particularly slow DSC kinetics (long time-constants). (d) Percent DSC vs time-constant of DSC. Kinetics of DSC were determined by fitting the results from the numerical simulation. The model predicts that the percent DSC linearly increases with the time-constant of DSC. (e) Numerical modeling of photobleaching out of S_1 and D_1. Kinetic modeling was performed in the presence (Two-Way) and absence (One-Way) of dark-state excitation for both continuous (CW) and pulsed illumination. The x-axis represents the microscopic photobleaching rate for S_1 or D_1, and the y-axis represents the photobleaching kinetics obtained by fitting the numerical simulations. For example, CW 1-Way D_1 Bleach represents a continuously illuminated numerical simulation where the dark-state does not absorb (*i.e.*, 1-way), and the D_1 bleaching rate is iteratively adjusted while the S_1 bleaching rate is held constant. Modeling demonstrates that when D0 does not absorb, the observed photobleaching rate is independent of bleaching out of D_1 and linearly correlated with bleaching out of S_1. Under two-way conditions, D_1 bleaching becomes significant for continuous illumination, but is minimized upon stroboscopic illumination. (f) Four-state model explains complex photophysical behavior observed for mKate2 and mApple under continuous photobleaching at 25 kW/cm^2. In cases where D_1 may be weakly fluorescent, due to changes in the fluorescence quantum yield of excitation rate, the rapid decrease and subsequent transient increase in fluorescence intensity represents population transfer from a bright-state to a dim-state prior to the onset of irreversible photobleaching.

DSC). This result suggested that the measured variation in the percent DSC (from 18 to 87%, Table 2.2) reflects changes in the kinetics of recovery from the dark state (τ_{dsr}). To test whether the DSC time constant obtained by fitting the fast phase of fluorescence decay reflects the rate of ground state recovery (*i.e.* transition from D_0 to S_0), we varied the microscopic time constant for dark state recovery (τ_{dsr}) and determined the corresponding time constant for DSC from the numerical simulations. At fast time scales (*i.e.*, < 100 μs), the time constant of DSC is correlated with the microscopic dark-state recovery kinetics (Figure 2.7c); while at longer time-scales (*i.e.*, $>$ 100 μs) the parameters are uncorrelated. For some of the FPs (7 out of 13), the measured DSC time constant is within the linear range of the simulated parameters, suggesting that for these FPs, the observed fluorescence decay directly reflects the kinetics of ground state recovery.

The four-state model also explains the correlation between the fastest timescale of fluorescence decay and the magnitude of DSC. Here, FPs with slower rates of ground state recovery will have an increased population build-up in D_0. In agreement with our experimental results, simulations predict that the percent DSC is linearly proportional to the DSC time constant (Figure 2.7d). Additionally, in agreement with our experimental data (Figure 2.5b), modeling confirmed that DSC increases linearly with the lifetime of S_1 (τ_{fl} = 0.5 - 4.0 ns) with small changes ($\approx$ 2-fold) in the simulated kinetics of DSC (results not shown).

Kinetic pathways for photodegradation out of both S_1 and D_1 (Figure 2.7a, kS_{1B} and kD_{1B}, respectively) were incorporated into the four-state model. Simulations of both continuous and pulsed illumination experiments were performed, as a function of both microscopic photobleaching rates (Figure 2.7e). In cases where excitation from D_0 to D_1 does not occur (One-Way in Figure 2.7e), the microscopic rate kS_{1B} was found to correlate linearly with the observed photobleaching rate for both pulsed and continuous illumination. In this case, photobleaching from the dark-state was negligible, and required kD_{1B} rates at 1000-fold greater than kS_{1B} to significantly alter the observed photobleaching kinetics. This result indicates that non-absorbing or weakly absorbing dark-states are photoprotective. Interestingly, in the case where the excitation from D_0 to D_1 does occur, (*i.e.*, Two-Way in Figure 2.7e) large differences were observed in the photobleaching

rate between continuous and pulsed illumination. For continuous illumination, the photobleaching rate was no longer linearly correlated with changes in kS_{1B}, and changes in the observed photostability became significant for kD_{1B} at rates comparable to kS_{1B} (*i.e.*, $> 10^3$ s^{-1}). Pulsed illumination however, minimizes the contribution of kD_{1B} to the observed photobleaching kinetics. These simulations suggest that comparison of photobleaching under pulsed and continuous illumination provides insight into whether the dark-state is photoprotective (bleaching does not occur from D_1) or photoreactive (bleaching does occur from D_1). For example, FPs with photoprotective dark-states, *i.e.*, TagRFP R67K S158T, likely do not absorb at the given excitation wavelength (*i.e.* transition from D_0 to D_1 is insignificant).

2.6 Discussion

Rapid irreversible photobleaching and DSC remain major obstacles in the utilization of FPs for single molecule applications, low-copy gene expression, and particle tracking *in vivo*. A better understanding of DSC, and new methods for measuring it, permit a detailed characterization of different FPs and may provide insight into which FP is most suited for a particular application. For example, our results (Figure 2.3a), as well as those of Shaner et al. [17], suggest that TagRFP-T may be the most photostable FP for low excitation intensity imaging (*e.g.*, wide-field arc-lamp, total-internal reflection fluorescence (TIRF), and live-cell laser scanning confocal microscopy). However, in single-molecule applications (single particle tracking, FCS, etc.), where excitation intensities exceed 1 kW/cm^2, mCherry and TagRFP R67K S158T appear substantially better than TagRFP-T (Figure 2.3b and 2.3c). These observations, and those on wavelength dependence (see reference [17] and Materials and Methods), illustrate that extensive data on excitation intensity and wavelength dependence data on each FP are necessary to select the optimal FP for a particular imaging application.

Numerical simulations demonstrate that a simple four-state model can explain how the magnitude of DSC varies with the kinetics of DSC and fluorescence lifetime, and how DSC contributes to irreversible photobleaching. The modeling also suggests that the measured kinetics of the initial

decrease in fluorescence (*i.e.*, kinetics of DSC) reflects the rate of dark-state recovery (τ_{dsr}), that the percent DSC is sensitive to changes in τ_{dsr}, and that comparison of CW and pulsed excitation measurements provides insight into coupling of the dark-state to photodegradation. In addition to replicating general trends, the four-state model can also explain complex behavior of select FPs such as mKate2 and mApple. These FPs undergo a rapid decrease in fluorescence intensity followed by a transient rise in fluorescence intensity prior to irreversible photobleaching (Figure 2.3b and 2.3c). This behavior can be explained by considering population transfer from the initially excited bright state to a less fluorescent state (*i.e.*, decreased quantum yield ϕD_{1Fl} and/or absorption rate kD_{0ex},) rather than a strictly dark state. Consequently, a transient rise in fluorescence intensity represents population build-up in the less-fluorescent state prior to the onset of irreversible photobleaching (Figure 2.7f).

Kinetic analysis of photobleaching 25.0 kW/cm^2 revealed a clear trend in mutations that act synergistically or antagonistically to impact irreversible photobleaching. For example, introduction of R67K into TagRFP S158T resulted in a 6.4-fold increase in the irreversible photobleaching time-constant without significantly altering the percent DSC (Table 2.2). Likewise, single mutations in the context of TagRFP R67K S158T, including N143S, T158S, or T158A, all exhibited excellent photostability, although to a lesser extent than TagRFP R67K S158T alone. Interestingly, in all tested cases, the presence of F174L decreased the photostability (Table 2.2), rendering the FP similar or worse in performance to the parent TagRFP S158T. These results suggest that mutations act in concert with regard to irreversible photostability, and that significant gains in photostability may be possible within the correct mutational context.

The kinetic simulations suggest that the rate of D_0 excitation dictates the extent to which D_1 is populated and hence whether D_1 is a significant precursor along a photodegradative pathway. For example, at 25 kW/cm^2 mCherry is markedly more photostable under pulsed vs. continuous illumination, suggesting that mCherrys dark-state is photoreactive. Alternatively, TagRFP R67K S158T does not undergo as large of a gain in photostability under pulsed conditions, suggesting that its dark-state is more photoprotective than photoreactive. For TagRFP R67K S158T, our numerical

modeling simulations suggest that this behavior could potentially result from a decreased dark-state excitation rate (*e.g.*, temporary alterations in the chemical structure of the chromophore, or protonation of the p-hydroxybenzylidene moiety upon a change in the local chemical environment).

The variability of photobleaching out of dark-states also provides some explanation of the contrasting behavior of mCherry and TagRFP R67K S158T at 25 kW/cm^2 compared to 2.5 kW/cm^2. At moderate intensities (tens of kW/cm^2), DSC rates scale linearly with excitation intensity [32] and consequently, FPs with more photoreactive dark-states will show heightened sensitivity to increases in excitation intensity relative to those with less reactive dark-states. Our experimental results and kinetic simulations also provide some context for published results that demonstrate the excitation wavelength dependence of FP DSC and photostability [17, 42, 43]. This wavelength dependence may be explained by changes in the excitation rate of D_0 relative to S_0, which varies in accordance with their corresponding excited-state absorption spectra. In cases where dark to bright-state conversion occurs, the final steady-state distribution of dark-state will depend on the rate of kD_{0ex}. For irreversible photobleaching, the relative rates of kD_{0ex} and kS_{0ex} dictate whether D_1 or S_1 is the dominant pathway for photobleaching.

The key reason for the value of our pulsed excitation method on FPs is that DSC and photobleaching occur on widely varying timescales, which are probed by the microsecond time-resolved fluorescence transients repetitively observed during the millisecond excitation/dark intervals. The method therefore resolves kinetics over six orders of magnitude in time, in particular extending measurements beyond the ms timescale. Experiments with a narrower experimental time-window, such as FCS, do not directly resolve both timescales, and therefore require a rigorous, separate analysis of irreversible photobleaching for the DSC time constants to be accurately determined [75–78]. Another key advantage in the broad time-window of our method is that it can be employed over the three orders of magnitude in excitation intensities encompassed by many commonly-used imaging techniques, thus potentially providing one set of measurements for quantitative comparisons of signal intensities.

In conclusion, examination of several closely-related RFPs with pulsed excitation provides

evidence for dark-states of varying reactivity and highlights the role of these states in irreversible photobleaching. This chapter introduces a spectroscopic method for independently measuring DSC and irreversible photobleaching at the ensemble level. In comparison with DSC kinetics measured on single-molecules [32,34,37,41,42], our methodology provides additional insight into slow events such as irreversible photobleaching, without requiring surface immobilization, and permits measurements inside living mammalian cells.

Chapter 3

Microfluidic Flow Cytometer for Quantifying Photobleaching of Fluorescent Proteins in Cells

3.1 Abstract

Traditional flow cytometers are capable of rapid cellular assays on the basis of fluorescence intensity and light scatter. Microfluidic flow cytometers have largely followed the same path of technological development as their traditional counterparts; however, the significantly smaller transport distance and resulting lower cell speeds in microchannels provides for the opportunity to detect novel spectroscopic signatures based on multiple, nontemporally coincident excitation beams. Here, we characterize the design and operation of a cytometer with a three-beam, probe/bleach/probe geometry, employing HeLa suspension cells expressing FPs. The data collection rate exceeds 20 cells/s under a range of beam intensities (5 kW to 179 kW/cm^2). The measured percent photobleaching (ratio of fluorescence intensities excited by the first and third beams: S_{beam3}/S_{beam1}) partially resolves a mixture of four RFPs in mixed samples. Photokinetic simulations are presented and demonstrate that the percent photobleaching reflects a combination of the reversible and irreversible photobleaching kinetics. By introducing a photobleaching optical signature, which complements traditional fluorescence intensity-based detection, this method adds another dimension to multichannel fluorescence cytometry and provides a means for flow-cytometry-based screening of directed libraries of FP photobleaching.

3.2 Publication Status and Author Contributions

Lubbeck, J.L., Dean, K.M., Ma, H., Palmer, A.E., Jimenez, R. Microfluidic Flow Cytometer for Quantifying Photobleaching of Fluorescent Proteins in Cells. Anal. Chem. 2012. May 7;9(5):1425-34.

J.L.L., K.M.D., A.E.P, and R.J. designed the research. J.L.L. and K.M.D. performed research. H.M. performed optical calculations. J.L.L. performed data analysis and photobleaching numerical simulations. J.L.L., A.E.P., and R.J wrote the paper.

3.3 Introduction

Traditional flow cytometers employ light-scattering and fluorescence-based detection to assess spectral diversity [79–81], cell size [82], fluorescence brightness [83–85], fluorescence lifetime [86,87], and analyte concentration [88] on individual cells flowing through one or more tightly focused excitation beams at speeds of ≈1-10 m/s. In this operating regime, the time window for optical excitation and detection is approximately a few microseconds per beam and hundreds of microseconds between beams. In contrast, the short transport dimensions and confining properties of microfluidic channels enable highly stable flows at cell speeds of 10^{-6} to 10^{-3} m/s. We exploited these properties to develop the ability to screen with optical or photophysical properties that are manifested at longer timescales (tens of milliseconds or slower) by implementing multipoint fluorescence excitation measurements in a microfluidic flow cell. We specifically investigate the probing of photobleaching in flow. Although it is likely to be ubiquitous in flow cytometry, few studies have investigated photobleaching in detail, and there are no reports of fluorophore screening or sorting based on photobleaching. Previous reports by van den Engh et al. and Doornbos et al. focused on understanding photobleaching and photon saturation in DNA stains, fluorescein conjugates, phycoerythrin, and allophycocyanin, via pulse shape and power-dependence measurements, primarily with the goal of optimizing the magnitude of fluorescence signals [89,90]. The excitation conditions in those studies accessed time windows of 2 μs to 2 ms, at excitation intensities of 5-3200 kW/cm^2.

Here, we report the design of a cytometer for assessing photobleaching of genetically encodable FPs, at excitation intensities comparable to those used for confocal imaging and single molecule spectroscopy (10-100 kW/cm^2).

FPs exhibit complex excited-state dynamics, including processes such as DSC and photobleaching which limit their photon output. The magnitudes and time-constants of both DSC and irreversible photobleaching depend on the fluorophore, excitation intensity, and excitation wavelength [17, 33, 49, 50]. Although these factors make the composite photobleaching process tricky to quantify, there is a clear potential for using it in flow-cytometric screening for the development of new FPs. This approach would be significantly faster than microplate or colony-based screening. Due to the longer time scale photophysics in FPs compared to small molecule fluorophores, a cytometry-based screening system will require that a correspondingly longer time-window be accessible to the measurement.

In Chapter 2, the use of millisecond pulse sequences to dissect the photobleaching process of FPs in individual HeLa cells was reported [49]. Here, to measure photobleaching of cells in flow, we implemented a design that quantifies photobleaching on the millisecond time scale, independent of fluorophore concentration, fluorescence quantum yield or extinction coefficient. We employ three spatially separated beams: a low-intensity probe beam (5 kW/cm^2) to measure initial fluorescence, followed by a high-intensity bleach beam (5-179 kW/cm^2) to initiate photodestruction of the fluorophores, followed by a second low-intensity probe beam, of equal intensity to the first, to assess the extent of photobleaching. This approach simplifies data acquisition compared to direct measurement of a time-resolved fluorescence decay because ratios of peak signal intensities are easier to fit and define than the multiexponential decays which characterize the photobleaching process.

Here, we combine microfluidics and spectroscopy techniques in a flow cytometer for measuring the combined effect of reversible and irreversible photobleaching at a rate of >20 cells/s. To our knowledge, this capability has not previously been reported. We present calculations guiding the optical design of a multibeam cytometer describing how to optimize measurement precision and alignment tolerance in a simple 2D hydrofocusing geometry. The technique is demonstrated on

four different RFPs, under a variety of excitation conditions, which uncovered a diverse range of reversible and irreversible photobleaching on the millisecond time scale. Lastly, we present kinetic simulations to examine the effects of reversible and irreversible photobleaching rates on the capability of our method to discriminate populations.

3.4 Experimental

The cytometer consists of four general components: (1) a microfluidic hydrofocusing chip and manifold which holds the sample and drives fluid flow, (2) an inverted microscope which serves as an optical platform for the cytometer, (3) optics to shape and align the three beams into the microscope, (4) the data acquisition and processing electronics.

3.4.1 Design Considerations

One of the design goals was to ensure that the distribution of measured fluorescence intensities for a population accurately reflects cellular RFP expression heterogeneity rather than instrument resolution. Even for a single-beam fluorescence measurement of each cell in flow, the excitation intensity and therefore the observed emission signal is strongly dependent on the trajectory of each cell as it traverses through the 3-D laser focus in the microchannel. Although, in principle, 3-D hydrofocusing geometries would more precisely define these cellular trajectories, we show that simpler-to-fabricate 2D hydrofocusing devices can provide sufficient precision for properly designed multibeam excitation/ detection geometries. In 2-D hydrofocusing, cells flowing past a cross-junction with two channels of sheath flow at higher pressures are laterally confined by the flow to dimensions significantly narrower than the channel width (Figure 3.1a) [91]. Nevertheless, there will always be lateral and axial variation (relative to the optical axis of the microscope objective: see Figure 3.1) in trajectories from cell to cell. We quantify the effects of this variation on the fluorescence signal, along with the effects of slight misalignment of the two probe beams relative to the flow axis of the microfluidic. We minimized the alignment sensitivity by introducing a cylindrical lens (f = 150 mm) positioned ≈190 mm before the objective lens, to shape the Gaussian

beam into an elliptical profile in the microchannel, in which the focused beam size perpendicular to the flow direction (y-axis) is much larger than along the flow direction (x-axis).

To quantify the impact of cell transit variation on the fluorescence signal, we first calculated the astigmatic transformation of a Gaussian beam through a cylindrical lens and objective optical system with a number of experimental constraints. We assumed that each cell was 14 μm in diameter (the mean cell size observed for HeLa-S cells on a wide-field microscope), had a uniform RFP concentration (*i.e.*, an RFP containing sphere) and traveled between two 4 μm diameter (FWHM) laser beams (Figure 3.1a and b). This beam size matched our measurements of the focused probe beam sizes produced with a 20x, 0.45 N.A. air-objective. The observed fluorescence signal, S (Equation 3.1), is the convolution of the RFP density, $s(x, y, z)$, and the three-dimensional Gaussian intensity profile at the laser focus, $B(x, y, z)$:

$$S(x_\circ, y_\circ, z_\circ) = \int\int\int_{x,y,z} s(x - x_\circ, y - y_\circ, z - z_\circ) \times B(x, y, z) dx dy dz \tag{3.1}$$

The intensity function of a radially symmetrical Gaussian beam may be written as:

$$B[x, y, z] = \left(\frac{2P}{\pi w^2[z]}\right) exp\left(\frac{-2(x^2 + y^2)}{w^2[z]}\right) \tag{3.2}$$

Where P is the total power of the beam and $w[z]$ is the beam radius where the intensity drops to $1/e^2$ of its peak value. The evolution of the Gaussian beam along the propagation direction, defined as the z axis here, is written as follows:

$$w_i[z] = w_\circ \sqrt{1 + \frac{z^2}{z_{Ri}^2}} \tag{3.3}$$

Where $z_R = \pi w_\circ^2/\lambda$ is known as the Rayleigh range, at $z = z_R$ the radius of beam is $\sqrt{2}$ times larger than its waist value w_{co}, or the beam area doubles. For a Gaussian beam propagating through a cascade of optical elements in space, its wave function is modified by the optical elements (*e.g.* lenses) it passes through. Due to the unique transform characteristics of the Gaussian beam, its propagation can be treated analogous to geometric optics following a general ABCD matrix

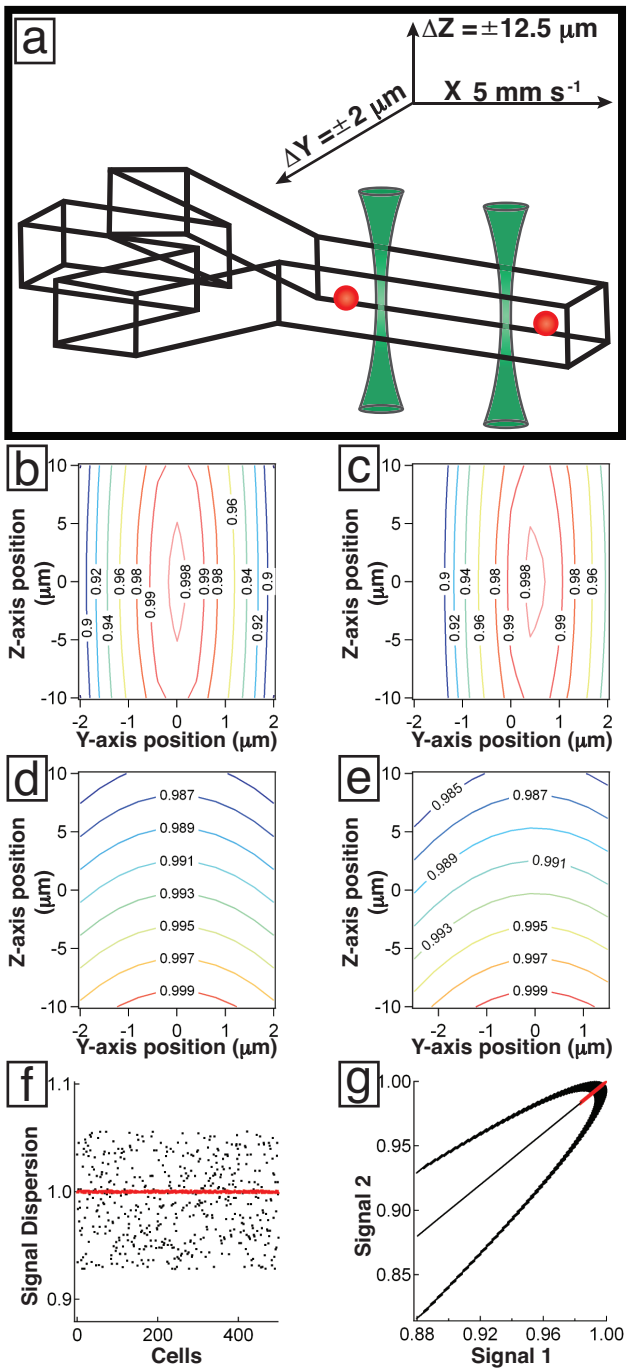

Figure 3.1: (a) Schematic of hydrodynamically-focused cells traveling through two circularly shaped Gaussian laser beams where ΔZ and ΔY refer to the cell axial and lateral displacement from the center of the channel. (b-e) Contour plots showing peak fluorescence signal as a function of the cell displacement (ΔZ and ΔY) as it flows through circularly (b-c) and elliptically (d-e) shaped Gaussian beams. (b and d) Represent the fluorescence signal if the two beams are perfectly centered in the channel, whereas (c and e) represent the fluorescence signal if the second beam is displaced 0.5 μm along the y-axis relative to the center of the channel. (f) For the misaligned beams, a scatter plot of the ratio of peak fluorescence signals (I_1/I_2) from 500 cells randomly displaced from the center of the channel (within ΔY = ±2 mm and ΔZ= ±5.5 mm) in signal from elliptically shaped beams (red) is 35-fold smaller than that of circularly shaped beams (black).

method [92], by defining a complex radius of curvature,

$$\tilde{q}^{-1} = R^{-1} - i\left(\frac{\lambda}{\pi w^2[z]}\right) \tag{3.4}$$

where R_z is the radius of curvature of the wave at position z.

In a case of astigmatic transformation, for example, the propagation of a Gaussian beam through a cylindrical lens, the evolution of the beam in the x and y directions differ and the evolution in each orthogonal direction can be treated independently.

In our experiment, a Gaussian beam from the laser first passes through a cylindrical lens (f_y=150 mm), then is focused by an objective lens (20x, NA=0.45) onto the sample. The sample is placed at the x-axis focal point of the objective lens, where the beam has passed the y-axis focal point and is therefore expanded across the microfluidics channel. We first deduced the analytical propagation equation of the Gaussian beam in this astigmatic optical system, then calculated the emission signal intensity of the fluorescent cells as they traverse through the beams. Here for simplicity we treated the objective lens as a simple lens with a specified focal length of 9 mm, as it is neither practical nor necessary to trace the beam propagation through each one of the dozens or more individual optical elements in a modern objective lens. In the x direction in which the cylindrical lens does not focus, the beam transfer matrix may be written as:

$$M_x = \begin{bmatrix} 1 - \frac{z_\circ}{f_{obj}} & z_\circ \\ -\frac{1}{f_{obj}} & 1 \end{bmatrix} \tag{3.5}$$

where z_0 is the distance between the objective lens and the sample, which is placed at the x-axis waist position, and f_{obj} is the focal length of the objective lens. The transfer matrix in the y direction can be calculated in a similar way, except that the cylindrical lens needs to be included in the transfer matrix.

The deduced analytical form of the Gaussian beam after the objective can be written as:

$$B(x, y, z) = \frac{2P}{\pi w_x[z] w_y[z]} \times exp\left[-\left(\frac{2x^2}{w_x^2[z]} + \frac{2y^2}{w_y^2[z]}\right)\right] \tag{3.6}$$

where P is the total power of the beam, $w_x[z]$ and $w_y[z]$ are respectively the x-axis and y-axis beam radius where the intensity drops to $1/e^2$ of its peak value. The evolution of the Gaussian beam along the propagation direction, defined as the z-axis here, is:

$$w_i[z] = w_\circ \left(1 + \frac{z^2}{z_{Ri}^2}\right) \tag{3.7}$$

where i denotes x or y-direction, and $z_{Ri} = 2\pi w_{\circ i}^2/\lambda$ is known as the Rayleigh range. At $z = z_{Ri}$ the beam radius is $\sqrt{2}$ times larger than its waist value $w_\circ$, and the beam area doubles.

The calculated beam radius at the sample, which is positioned at the x-axis waist position, is $w_x[z]|_{z=z\circ} = 2$ μm and $w_y[z]|_{z=z\circ} = 56$ μm, which is consistent with the measured beam radius of $w_x = 3$ μm and $w_y = 67$ μm. The distribution of peak signal intensities from a cell traversing a spherically and cylindrically focused beam centered on the hydrodynamic flow are shown in Figure 3.1b and d, respectively. These contour plots reveal how the observed fluorescence signal varies as a function of the cell axial and lateral position with respect to the center of the channel (ΔZ = ΔY=0). Figures 1c and 1e are similar, but correspond to the case in which the beam is displaced laterally (ΔY=0.5 μm) with respect to the center of the channel. This displacement represents the precision of experimental alignment. Due to the relatively low NA of the optical system, the signal intensity is insensitive to cell axial positioning ($\pm$5.5 μm is the maximum range for a 14 μm diameter cell in a channel of 25 μm height) for both spherical and cylindrical focusing. However, in the lateral direction, a comparison of spherical vs. cylindrical beam shaping reveals very different sensitivity to cell position and beam alignment. In particular, if the beams are misaligned or the cell drifts by ΔY=0.5 μm, the difference in the peak fluorescence intensity of the second beam relative to the first beam is significantly smaller with the cylindrical focus (Figure 3.1d-e). Consequently, we consider cells transiting only along the X-axis between the two probe beams at randomly chosen axial and lateral positions in the range ΔY = $\pm$2 μm and ΔZ= $\pm$5.5 μm. If the two beams are perfectly aligned, then for both cases, the ratio of fluorescence intensities (beam 1 / beam 2) = 1. However, for the misaligned geometry, this signal ratio depends on the cell position in the

channel. Figure 3.1g shows that for cylindrically focused beams, it shows a 35-fold lower dispersion in the signal intensities compared to the spherically focused beams. This result indicates that pairs of cylindrically focused beams will lead to substantially smaller variability in fluorescence measurements.

3.4.2 Microfluidics and Optical Layout

Microfluidic devices were built by anodically bonding a 25 μm thick 2 in. diameter silicon wafer to a 1.7 mm thick glass-slide. Silicon was etched down to the glass in the pattern of the channels using standard photolithography and plasma etching techniques [93]. This method results in optically transparent channels of 25 μm height $\times$ 150 μm width $\times$ 1 mm length for the central interrogation channel. Sample ports of 1 mm diameter were drilled in a second, identical glass slide before bonding to the silicon.

The microfluidic was compression-fit with O rings against a manifold constructed from polytetrafluoroethylene (PTFE; to minimize nonspecific adsorption of cells) with 200 μL sample reservoirs (Figure 3.2. The microfluidic device and combined manifold assembly were mounted onto the stage of a commercial inverted microscope. Flow was driven using three closed-loop air-pressure controllers connected by PTFE tubing to the sample ports. By independently varying the pressures on all three inlets, the hydrodynamic focal width was kept constant at 15 μm as measured by imaging the fluorescence from a dye flowing in only the center cell channel [91]. The cell speed in the interrogation region was varied from 1 to 15 mm/s to control exposure time to the bleach beam. The speed was calculated from measurements of cell transit times between probe beams 1 and 2 using fluorescence signals, and measurements of spatial separation of the beams (Figure 3.3; typically 240 $\pm$ 3 μm). The cell speed distribution typically had a standard deviation of 1%. The flow was visualized with a CMOS camera, and wide-field transillumination was provided by a home-built condenser.

The three-beam geometry consisted of two equal intensity probe beams measuring the peak fluorescence from a cell before and after a higher-intensity photobleaching beam. To implement this

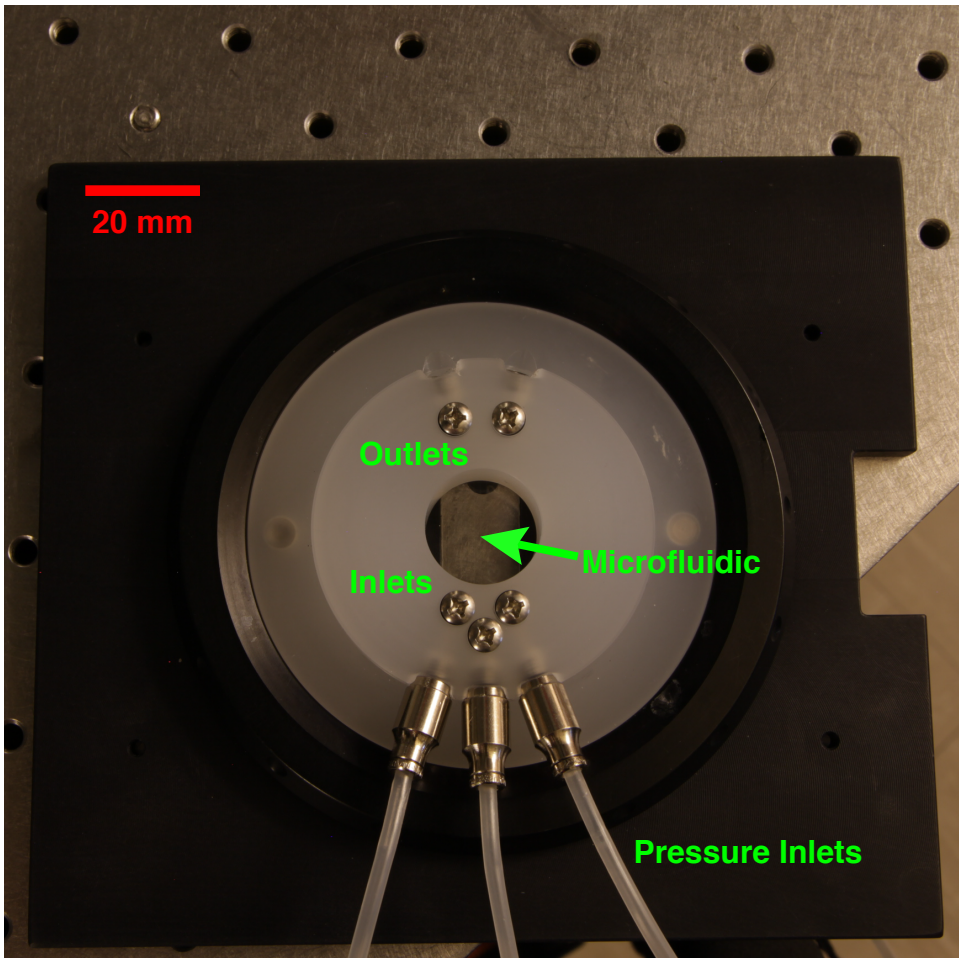

Figure 3.2: Microfluidic and manifold assembly.

experimental geometry, a 2 W 532 nm continuous wave laser was split into three beams by a series of beam splitters (30:70 and 50:50) and waveplate-polarizer pairs, thereby allowing independent control of each beams excitation intensity. After splitting, all beams were shaped by a cylindrical lens (150 mm focal length), directed into the microscope, reflected from a 532 nm dichroic mirror, and focused inside of the microfluidic channels by a 20×, 0.45 NA air-objective (Figure 3.3a). Shaping the beams with the cylindrical lens results in elliptical beams (75 μm length and 3.5 μm width, FWHM, as measured by imaging light scattered from the sample focal plane onto a CMOS camera) that stretch the entire width of the hydrofocus. The beams were distributed over a 240 μm distance with the bleach beam located midway between the two probe beams (Figure 3.3b). The probe beam intensity was 5 kW/cm^2 and the bleach beam was 170 kW/cm^2 (calculated from the FWHM of the beam dimensions and laser power measured at the sample plane (±5%)). The probe beams were matched in intensity before each experiment. Fluorescence was collected through the same objective and separated from excitation light by the 532 nm dichroic mirror and a 545 nm long-pass filter. The emission was detected by a red-sensitive photomultiplier tube (PMT, Hamamatsu, R9880U- 20) on the primary imaging port of the microscope. At this port, the fluorescence signals from the three beams are spatially resolved, which allowed for placement of a mask at the focal plane which blocks the photobleaching beam. A lens is used to refocus fluorescence from the two probe beams onto the PMT.

3.4.3 Data Acquisition and Processing

The PMT photocurrent was processed by a custom-built AC-coupled transimpedance operational amplifier, which improves the signal-to-noise ratio by removing high and low frequency noise components outside the band-pass of 0.16 - 106 kHz. The resulting voltage levels were digitized at 250 kHz with a PC-based data acquisition board (16 bit ADC) and custom software (LabView, National Instruments). After fitting each peak to a Gaussian, the peak fluorescence signals for the first and second probe beams (S_{beam1} and S_{beam3}) were recorded. Typical fluorophore transit times through each beam varied from 0.2 to 3.5 ms depending on the cell velocity (1-15 mm/s) and

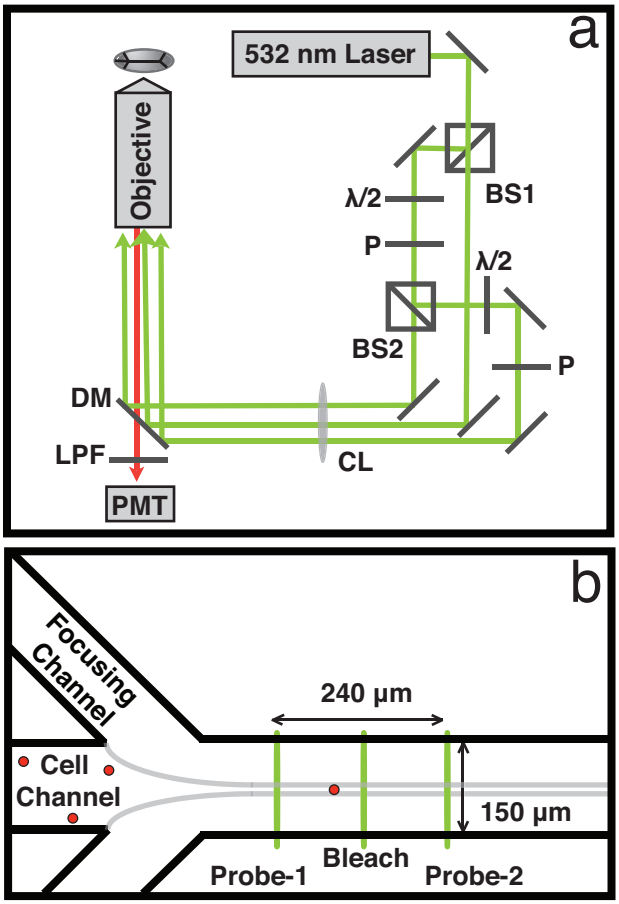

Figure 3.3: (a) Schematic of the optical setup. Relevant components include: 20× 0.45 N.A. air immersion objective (Obj.); 532 nm dichroic mirror (DM); 545 nm long-pass filter (LPF); red-enhanced photomultiplier tube (PMT); 150 mm focal length, cylindrical lens (CL, placed 19 cm from back aperture of objective); half-wave plate ($\lambda/2$); Glan-Thompson polarizer (P); 70:30 beam splitter (BS1); 50:50 beam splitter (BS2). (b) Schematic of the microfluidic channel geometry at the interrogation region. Cells were hydrodynamically focused to a width of 15 μm before encountering the elliptical bleach and probe beams (FWHM 3 $\times$ 75 μm).

neglecting fluorophore diffusion within the cell.

3.4.4 Sample Preparation

HeLa suspension (HeLa-S, mean diameter = 14.4 μm, coefficient of variation (CV) = 21.8%, as measured from images taken on a widefield microscope) cells were maintained in spinner flasks at 37° C in a 5% CO_2 atmosphere using spinner-modified Dulbeccos Modified Eagles Medium, 10% FBS, and 1% penicillin-streptomycin. HeLa-S cells were virally transduced according to manufacturers protocols with an FP either under a constitutive cytomegalovirus promoter (TagRFP, and TagRFP-T in pCLNCX) or an inducible tet-responsive promoter (mCherry, mOrange2, pCL-TRE). Briefly, virus was generated by transfecting the appropriate combination of DNA (pCLNCX-FP, pCLTRE-FP, pCL-Ampho, pCL-TetOn, pVSV-G) into HEK293FT cells. After two days, the viral containing supernatant was collected, passed through a 0.45 μm cellulose acetate filter, and added to HeLa suspension cells with 12 μg/ml polybrene, and if appropriate, expression was induced with 1 μg/ml doxycycline. Two days after the retroviral transduction of HeLa suspension cells, fluorescence-activated cell sorting (FACS) with a Dako Cytomation Mo-Flo cell sorter was used to enrich the population of successfully infected cells (RFP fluorescence positive). Fluorescent cells were enriched using a commercial flow-cytometer at a concentration of approximately 1 million cells per mL in Ca^{2+} and Mg^{2+} free HHBSS, pH=7.4. Excitation was performed with a 568 nm krypton laser, forward scatter was used to trigger acquisition, and the fluorescence emission was separated from the excitation scatter by use of a 630/30 band-pass filter. The PMT was set at 450 volts, and forward scatter, side-scatter, and fluorescence were all operated in logarithmic modes. The flow-cytometer was maintained at around 2,000 events per second. Sufficient optical alignment was confirmed by a narrow (1.3%) coefficient of variation using Beckman Coulter Flow-Check Fluorospheres (part number: 6605359, diameter = 10 μm). Uninfected, and thus non-fluorescent, HeLa suspension cells were used to set the threshold (or gate) and so the sort attempted to select all cells with fluorescence greater than cellular autofluorescence. To avoid biasing the fluorescent populations evaluated in our experiments, FACS was only performed initially for each individual cell-line, and

Table 3.1: Fluoresence Coefficient of Variation and Expression Vector for Each Cell Line

Protein Expressed in Cells	Vector	Fluorescence CV
TagRFP-T	pCLNCX	131.52%
TagRFP	pCLNCX	158.26%
mCherry	pCL-Tet-On	250.16%
mOrange2	pCL-Tet-On	145.77%

G418 (working concentration of 100 mg/mL) was applied to select against potential loss of retroviral gene insertion. The fluorescence observed for virally transduced cells varied from cell-line to cell line according to Table 3.1.

Aliquots of cells were concentrated *via* swinging-bucket centrifugation at 1000 rpm for 5 min. To prevent clumping and settling within the microfluidic reservoirs, cell pellets were resuspended in a density-matched medium using a commercially available density matching solution and HEPES-buffered Hanks balanced salt solution (HHBSS), pH 7.4 solution supplemented with 1% bovine serum albumin. Experiments involving beads utilized 6 μm diameter fluorescently labeled beads from a Invitrogen LinearFlow Deep Red Flow Cytometry Intensity Calibration Kit, suspended in a density matched 20% (v/v) glycerol in water solution. The microfluidic channels were passivated with a 1% solution of bovine serum albumin prior to each run. Cell suspensions were loaded into the center reservoir in 150 μL aliquots at a concentration of $\approx 5\times10^5$ cells/mL. The side channels were filled with 150 mL aliquots of HHBSS, pH = 7.4 for the sheath flow.

3.5 Results and Discussion

The measured quantity in all experiments described below is the %bleach, which is defined in terms of the measured peak fluorescence signal for the first and third beams (S_{beam1} and S_{beam3}, respectively), as:

$$\%bleach = \left[1 - \left(\frac{S_{beam3}}{S_{beam1}}\right)_{With\ Bleach\ Beam} \times \left(\frac{S_{beam3}}{S_{beam1}}\right)_{No\ Bleach\ Beam}\right] \tag{3.8}$$

To correct for small differences in beam intensity, and lateral misalignments of probe beams,

the %bleach is defined as the function of reference measurements taken in the absence of the bleach beam. Note that %bleach may be composed of a combination of reversible and irreversible photobleaching, as dictated by the excited-state dynamics of the fluorophores. To shed light on the molecular origins of the measured %bleach in terms of the rate constants for reversible and irreversible photobleaching, we present and discuss numerical simulations of the signals in terms of a four-state model of RFP photophysics.

3.5.1 Instrument Validation and Theoretical Considerations

We first performed multibeam fluorescence measurements on fluorescently labeled beads to verify the precision of the measurements matched predictions from the design considerations discussed above. Data from one probe beam yields a fluorescence intensity CV ranging from 6 to 16%, depending on the fluorescence intensity of the bead type (higher intensity beads yielded lower CV, Figure 3.4b). The CV value averaged over all three populations of beads, was within 10% of the average value obtained on a Dako Cytomation Mo-Flo FACS (Figure 3.4). This variability is lower than many other 2D-focusing microfluidic cytometers (CV of 25-30%) [94, 95] and comparable to 3D-focusing microfluidic cytometers (CV of 1-9%) [96, 97] but remains larger than state-of-the-art flow cytometers (CV $<$ 3%, BD Biosciences). For a two probe beam measurement with a mixture of beads, a plot of S_{beam3} vs. S_{beam1} was linear, with a coefficient of determination, R^2=0.99 with a 7% standard deviation in the ratio of S_{beam1} vs. S_{beam3} for greater than 3,000 events (Figure 3.4a). Additionally, our microfluidic platform detected all but the most weakly fluorescent beads, those which have intensities comparable to cellular autofluorescence on a standard flow cytometer. Furthermore, the flexibility of our microfluidic platform permitted accurate measurement of fluorescence intensities spanning three orders of magnitude (0.1-10.0 V). Our signal to noise was limited by the noise-floor of our transimpedance amplifier and saturation of our PMT or analog-to-digital conversion hardware, enabling the user to tune the cytometer for maximum utility within a specific range of fluorescence intensities.

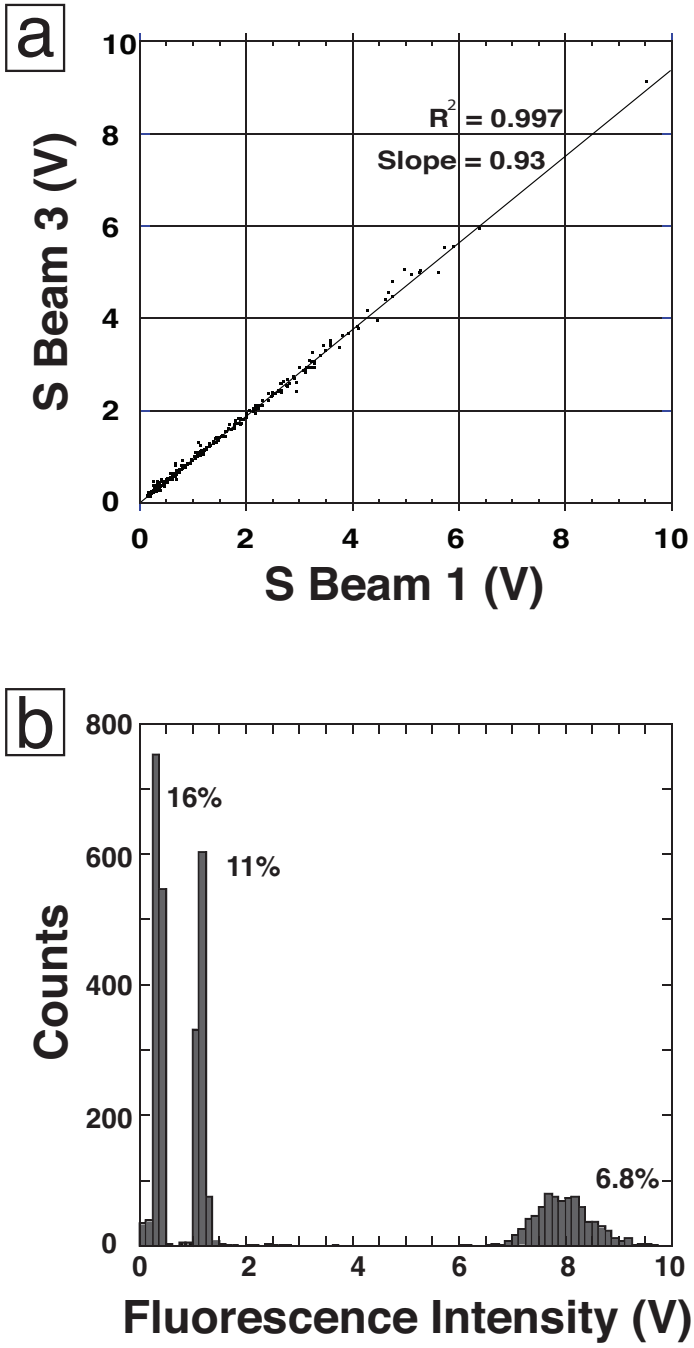

Figure 3.4: Commercially available intensity calibration beads (Invitrogen LinearFlow Deep Red Flow Cytometry Intensity Calibration Kit), suspended in a density matched 20% (v/v) glycerol in water solution) were used to characterize the microfluidic cytometer. (a) Using a mixture of beads with different fluorescence intensities, the correlation between the two probe beams was determined to be linear. The data collected in this run resulted in a slope of 0.93 with a CV of 7%. (b) With a single excitation beam (10 kW/cm^2), mixtures of polystyrene beads with three different fluorophore densities were resolved and yielded fluorescence intensity coefficients of variation (CV, listed as % in the above figure) similar (less than 10% different on average) to those measured individually on a FACS in a linear fluorescence mode (from left to right: 12.1%, 11.3%, and 7.8%).

3.5.2 Single-RFP Population Photobleaching

Two-beam measurements (without a bleach beam) on HeLa-S cells expressing TagRFP-T were fit to a line with a coefficient of determination of 0.99 and an 11% CV in the ratio of S_{beam3} vs S_{beam1} (Figure 3.5). In principle, for two probe beams of identical intensity, and in the absence of photobleaching, we observed slopes of slightly less than 1 for both the beads(0.93, CV=7%, 3.4) and TagRFP-T-expressing cells (0.94, CV=11%) which were statistically the same by an unpaired t test (T=1.42). Under these probe beam conditions, we expect photobleaching of the beads, and even the less photostable RFPs, to be negligible. For example, using photobleaching kinetics parameters measured for TagRFP-T at 532 nm in immobilized HeLa cells at similar intensities [49], we estimate 0.4% photobleaching occurs. It seems likely that the nonunity slope occurs primarily due to a slight mismatch in the probe beam power transmitted through the objective, which we observe to be highly sensitive to alignment into the microscope. In our definition of %bleach, we account for this mismatch in probe beam intensities, to provide for a corrected measure of the bleaching magnitude. For TagRFP-T cells, with a bleach beam intensity of 170 kW/cm^2 and flow speed of 27.9 mm/s (exposure time of 125 μs), the slope decreases to 0.52 (Figure 3.5), which indicates a significant amount of bleaching (%bleach = 51%, from Equation 3.8). The same performance for all measurements were reproduced with the beams intersecting the hydrofocused stream anywhere along the 1 mm length from immediately after the hydrofocus to the end of the interrogation channel.

3.5.3 Resolving Fluorescent Protein Populations

To evaluate the ability to resolve subpopulations on the basis of photobleaching, three-beam measurements were performed on a mixture of HeLa-S cells expressing TagRFP [16], TagRFP-T [17], mOrange-2 [17], and mCherry [15]. Photophysical properties of these FPs are summarized in Table 3.2. With a bleach beam intensity of 170 kW/cm^2 and flow speed of 12.9 mm/s (exposure time of 270 μs), the beam spacing resulted in an 8 ms average cell transit time between beams.

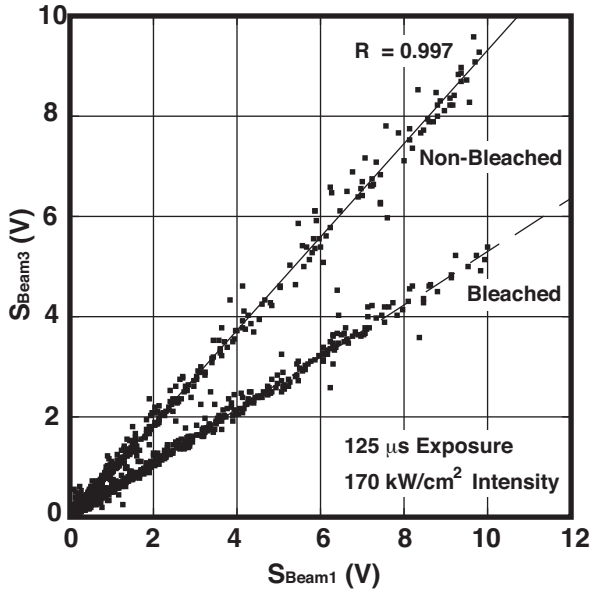

Figure 3.5: HeLa-S cells virally transduced with TagRFP-T interrogated with the two probe beams indicate that the cytometers response is linear with respect to fluorescence intensity and the signals from each probe beam are highly correlated (CV =11%, R^2=0.997, Non-Bleached Slope = 0.94, Bleached Slope = 0.52). Upon addition of the bleach beam, the slope decreases, indicating photobleaching. Here, each point represents a measurement performed on a single cell.

This time scale permits complete recovery from higher-ordered excited states and dark states [49] (Table 3.3). Under these conditions, four populations of cells were apparent in the plots of S_{beam3} vs S_{beam1} (Figure 3.6a). Each RFP-expressing cell population was identified by measurements on the individual cell types under identical flow and intensity conditions. A histogram of %bleach for the ≈1891 cells in this sample also reveals four subpopulations, corresponding to the four RFPs (Figure 3.6b). The rank order of average fluorescence intensities for the cell lines measured in the microfluidic cytometer agreed with those measured by FACS (TagRFP-T = TagRFP > mOrange2 > mCherry). The differences in fluorescence brightness for different RFP-expressing cell lines may result from differences in the relative absorption cross section at 532 nm (Table 3.1) or from differences in cellular RFP concentrations, which in turn may result from incomplete chromophore maturation and differences in the transcription promoter strength. As stated previously, the cells assayed in the cytometer were not prescreened or enriched for brightness; therefore, a large range (CV > 130%) of intensities were screened. Tuning the PMT gain to optimize detection of weakly fluorescent cells would permit improved resolution of the photobleaching response in these cells [51]. In Figure 3.6c, we plot the measured %bleach vs prebleach fluorescence intensity for the cell mixture. These data show a resolution of the mixture into four populations and demonstrate that the measured %bleach depends on the RFP but is largely independent of the fluorophore concentration (as given by the prebleach emission level). The ability of %bleach to resolve the mixture of four RFPs may be quantified by fitting the histogram (Figure 3.6b) to a sum of four Gaussians. The fit parameters (Figure 3.5 caption) reveal that the mean %bleach values for mOrange2, mCherry, and TagRFP were separated by at least 1σ, whereas the TagRFP-T population was separated from the others by at least 2σ. The percentages of cells that could be uniquely assigned to one population with at least 99.9% confidence were obtained by determining the confidence interval of the Gaussian fit for a given cell population which has less than 0.1% overlap from the Gaussian fits for the other cell populations. This confidence interval defines the percentage of cells in a population that can be assigned to a given Gaussian fit with 99.9% confidence. The percentages resolved by this criterion are as follows: 1% of the mOrange 2 cells were resolved from the mCherry cells, 43%

Table 3.2: Reported photostabilities are from Shaner et al. [17]. Experimental details for the measurement of these photophysical properties can be found in [49].

RFP	Ex/Em Max (nm)	Abs. Cross-Section @ 532 nm (cm^2)	Quantum Yield	Chromophore	Reported Photostability [17] $t_{1/2}$ (s)
mOrange2	550/563	1.36×10^{-16}	0.55 ± 0.04	Tricylic [98]	2,900
mCherry	586/609	1.45×10^{-16}	0.16 ± 0.02	Cis [98]	1,800
TagRFP	554/579	2.55×10^{-16}	0.48 ± 0.04	Trans	550
TagRFP-T	555/580	2.93×10^{-16}	0.47 ± 0.08	Trans	6,900

of the mCherry cells from the mOrange2 and TagRFP cells, 10% of the TagRFP cells from the mCherry and TagRFP-T cells, and 100% of the TagRFP-T cells from the others.

3.5.4 Photokinetic Simulations

To understand the connection between microfluidic photobleaching measurements and fluorophore photophysics, we performed numerical simulations based on a four state system consisting of the ground state (S_0), the first excited state or bright state (S_1), and two dark or weakly fluorescent states (D_0 and D_1) (Figure 3.7a). Table 3.4 contains a summary of the reactions and kinetic parameters. Photobleaching was permitted out of S_1 and D_1. Recently we used this four-state model to describe the excited-state dynamics of RFPs in immobilized single cells exposed to a series of millisecond timescale excitation pulses, and demonstrated that this model faithfully captured trends for reversible and irreversible photobleaching for a panel of 13 FPs [49]. A similar model has been used to examine reversible photobleaching (*i.e.* blinking) of GFP [31]. We modified our previous simulations by approximating the excitation profile as a sum of Gaussian pulses that replicate the durations and excitation rates experienced by the fluorophores as they flow through the three beams in the cytometer.

Previous investigations of photodynamics in flow cytometry primarily focused on photobleaching and photon saturation [89, 90], which are the dominant processes operative at the $\approx10^3$

Table 3.3: Percent recoveries ± the standard deviation for the four RFPs after a 2 ms, 100 kW/cm^2 pulse of illumination from a 532 nm CW laser followed by either 8 ms, 1 s, and 10 s in the dark prior to the next 2 ms pulse. Experimental details are reported in [49].

RFP	Percent Recovery 8 ms	Percent Recovery 1s	Percent Recovery 10s	ANOVA P-Value
mOrange2	70 ± 3 (n=3)	75 ± 2 (n=3)	72 ± 2 (n=2)	0.12
mCherry	73 ± 6 (n=2)	74 ± 7 (n=3)	81 ± 6 (n=2)	0.49
TagRFP	54 ± 1 (n=3)	62 ± 7 (n=3)	63 ± 7 (n=2)	0.14
TagRFP-T	20 ± 4 (n=3)	32 ± 5 (n=3)	26 ± 5 (n=2)	0.059

Table 3.4: Summary of Reactions and Equations Used in Photokinetic Model

Process	Reaction	Reaction Rate	Rate Constant Value (s^{-1})
Emission and Non-Radiative Decay	$S_1 \rightarrow S_0$	$[S_1]\ k_{Em}$	$k_{Em} = 1\times10^9$
Reversible Photobleaching	$S_1 \rightarrow D_1$	$[S_1]\ k_{Rev}$	k_{Rev} = Varied = 0 - 1×10^6
Dark-State Decay	$D_1 \rightarrow D_0$	$[D_1]\ k_{DSD}$	$k_{DSD} = 1\times10^9$
Ground-State Recovery	$D_0 \rightarrow S_0$	$[D_0]\ k_{GSR}$	$k_{GSR} = 1\times10^4$
S_1 Bleach	$S_1 \rightarrow$Null	$[S_1]k_{S1Bleach}$	$k_{S1Bleach}$ = Varied = 0 - 5×10^6
D_1 Bleach	$D_1 \rightarrow$Null	$[D_1]\ k_{D1Bleach}$	$k_{D1Bleach}$ = Varied = 0 - 5×10^{10}
Excitation	$S_0 \rightarrow S_1$	$[S_0]\ k_{Ex}$	k_{Ex} = Gaussian

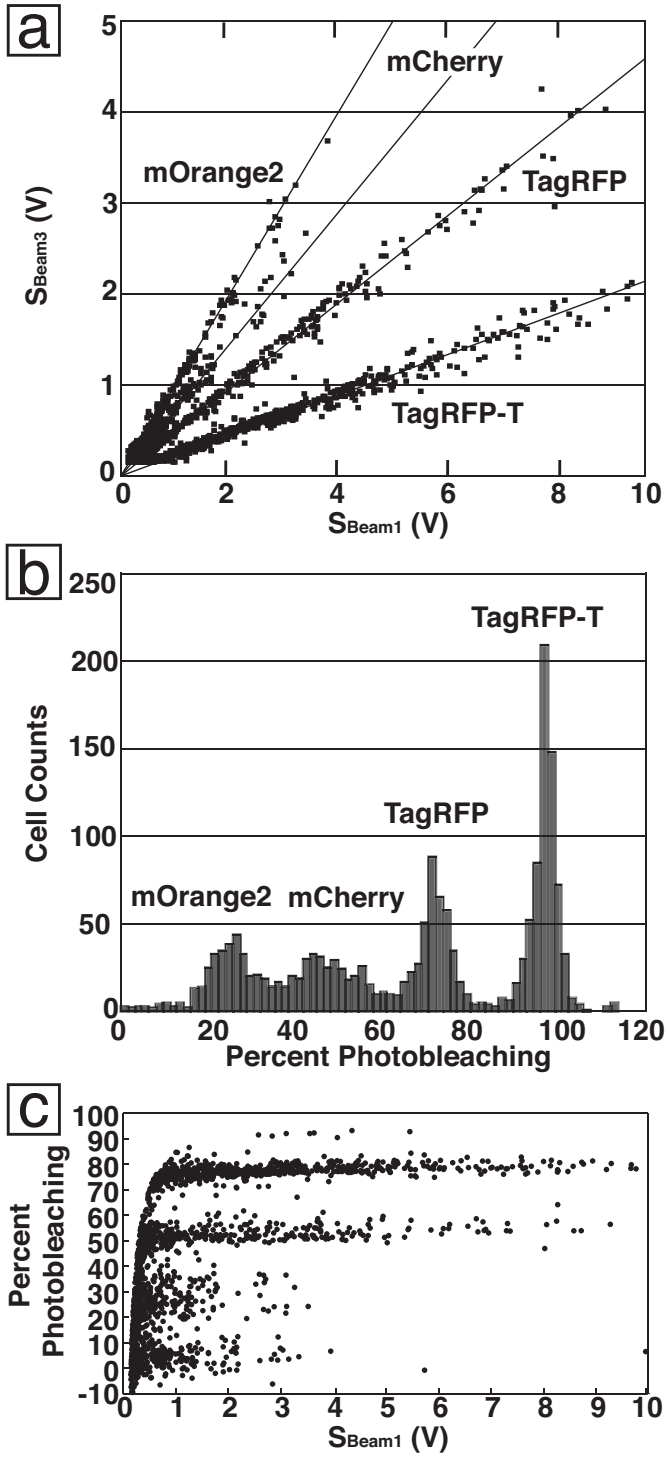

Figure 3.6: (a) A mixture of cells expressing one of four RFPs was resolved on the basis of photobleaching. Each point represents an individually assayed cell and the slope of the S_{beam1} versus S_{beam3} plot yields the %bleach for each RFP. (b) The mean %bleach for each RFP-expressing cell line (upon measurement of 200-300 cells) was 4.4 (CV = 145%) %bleach for mOrange2, 26.8 (CV = 49%) %bleach for mCherry, 52.0 (CV = 9%) %bleach for TagRFP, and 77.3 (CV = 4%) %bleach for TagRFP-T as determined using a fitting program which fit a sum of four Gaussian functions to the histogramed data. (c) Plot of %bleach vs. pre-bleach intensity, showing the resolving power provided by bleaching measurements.

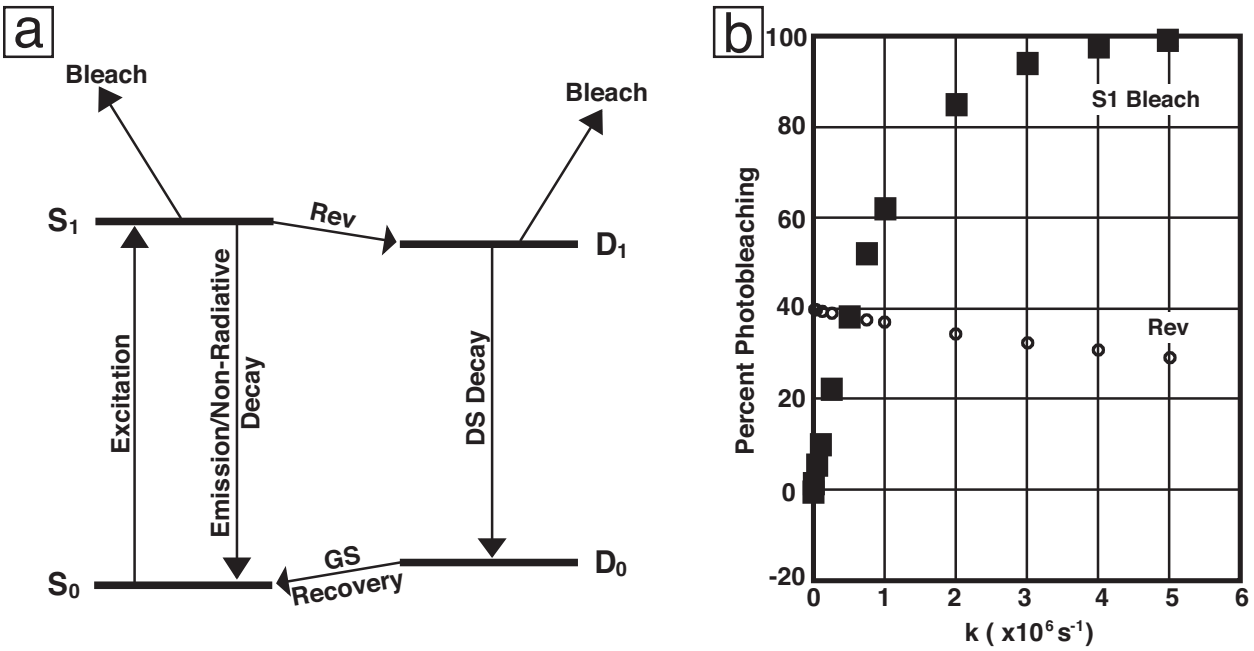

Figure 3.7: (a) Jablonski diagram depicting four-state model used for photokinetic modeling results. (b) Simulated percent photobleaching as a function of $kS_{1Bleach}$ or k_{Rev}. $kS_{1Bleach}$ was held constant while k_{Rev} was varied and the percent photobleaching was calculated (○). k_{Rev} was held constant while $kS_{1Bleach}$ was varied and the percent photobleaching was calculated (■). Increasing rates of irreversible photobleaching out of the first excited singlet state and reversible photobleaching have opposite effects on observed photobleaching.

kW/cm^2 intensities and microsecond timescales considered in those investigations. Photon saturation occurs when the average time between excitation-photon absorption approaches the time the fluorescent molecule spends in the excited state. We estimate that the average arrival time between excitation photon for our highest intensity beam (170 kW/cm^2) beam was 1.7 photons/msec. Since the excited-state lifetime of the RFPs are in the range of 2-3 ns [49], photon saturation is negligible under the conditions employed here. We therefore focused on photobleaching and DSC processes.

The excitation rate was calculated using the measured, average-excitation intensity to find the peak-excitation intensity, which was then used to calculate the maximum rate of excitation for a representative RFP (TagRFP-T, which was chosen because its photophysical properties represent the median of the four proteins assayed) using its extinction coefficient at 532 nm (52000 M^{-1} cm^{-1}) and the Beer-Lambert law:

$$k_{ex} = \frac{\sigma I \lambda}{hc} = 2.303 \times 1000 \left(\frac{\epsilon I \lambda}{N h c} \right) \tag{3.9}$$

where σ is the absorption cross-section, I is the light intensity, λ is the wavelength, h is Plancks constant, c is the speed of light, ϵ is the decadic molar extinction coefficient, and N is the number of molecules.

The fluorophores first experience an excitation rate corresponding to the first probe beam. The rate of excitation increases and then decreases in a Gaussian profile in time from zero up to the peak rate of excitation (8×10^4 s^{-1}) and then back to zero over the course of 0.54 ms. The excitation rate remains at zero for 20 ms (as mentioned previously, ground state recovery is complete after 8 ms) before experiencing the excitation of the bleach beam (maximum rate of 1.6×10^6 s^{-1}) and, lastly, the third probe beam. In accord with the calculations and measurements on the cylindrical beam shaping, the excitation profile was assumed to be constant in the direction perpendicular to the cells travel. The FWHM of the laser spatial profile was transformed into time coordinates assuming an average cell velocity of 6 mm/s which is approximately the mid-point of the range of speeds used in these experiments. The peak of the time-dependent fluorescence profiles from the

first and third excitation beams was then used to calculate the %bleach.

The values of the rate constants for each step in the four-state model were taken from Chapter 2 (Table 3.4) [49]. In particular, three parameters were varied individually and the magnitude of photobleaching was calculated for each simulation. First, the rate of bleaching out of the higher-energy dark-state ($k_{D1Bleach}$) was varied while k_{Rev} and $k_{S1Bleach}$ were held at 5×10^5 s^{-1}. A negligible increase in %bleach was observed for all but extremely large rate constants (1×10^{10} s^{-1}) indicating that, in this model, the dark state acts photoprotectively, *i.e.* the fluorophore does not bleach out of the dark state. Next, the rate of bleaching out of the first excited state ($k_{S1Bleach}$) was increased from 0 - 5×10^6 s^{-1} while k_{Rev} was held at 5×10^5 s^{-1} and $k_{D1Bleach}$ was held at 0. This perturbation resulted in an expected increase in %bleach since the increased rate of bleaching allowed the bleaching process to compete more successfully with the other S_1 depopulation pathways. Lastly, the rate of reversible photobleaching (k_{Rev}) was increased over the same range while $k_{S1Bleach}$ was held at 5×10^5 s^{-1} and $k_{D1Bleach}$ was held at 0, leading to a decrease in %bleach. This trend shows that reversible and irreversible photobleaching are competing processes since increases in the rate of either process leads to opposite impacts on the observed %bleach. These trends are plotted together in Figure 3.7b. Although the results of our model indicate that the $k_{S1Bleach}$ has a greater effect than k_{Rev} on the observed values of %bleach, note that in general, the rates of both processes are known to change with excitation intensity, pulsed vs. continuous wave illumination, and excitation wavelength [17, 33, 49].

For the four RFPs investigated here, the rates of reversible and irreversible photobleaching vary over 1-2 orders of magnitude across the range of excitation intensities characteristic of widefield and confocal microscopies (10 W/cm^2 - 1 kW/cm^2) (Table 3.2) [17]. Therefore, for completeness, these calculations were performed using a range of rate values (Table 3.4), covering both experimental and modeling estimates [31, 33, 37, 43, 49, 90]. Our kinetic simulations indicate it is likely that the rates of both reversible and irreversible photobleaching are in the range from 1×10^5 to 1×10^6 s^{-1} since experimental and modeling results for the observed %bleach are in agreement in this range. Furthermore, these simulations predict that, for the current set of measurements,

the magnitudes of reversible and irreversible photobleaching are anti-correlated (Figure 3.7b). The RFPs examined have rate constants that vary by an order of magnitude or less and our modeling results indicate that, over this small range, the effects of reversible photobleaching significantly influence the observed extent of irreversible photobleaching.

The four proteins examined in this study represent closely related fluorophores. In particular, TagRFP and TagRFP-T differ by only one point mutation and have similar fluorescence spectra and quantum yields (Table 3.2). However, as emphasized by the resolution of the populations in Figure 3.6, the FPs differ greatly in their photostabilities and propensities for reversible photobleaching. Our photokinetic simulations show that although the four cell populations are differentiated with our 3-beam geometry, they are not resolved solely on the basis of reversible or irreversible photobleaching but rather, by a combination of both processes. For this reason, additional resolving power will be necessary if the two processes are to be separated. For example, according to pulsed photobleaching experiments performed on stationary, individual cells (Figure 3.8 and Tables 3.2 and 3.3), mCherry is less prone to both irreversible and reversible photobleaching than mOrange2. However, the significant contribution of reversible photobleaching for mOrange2 causes it to appear very similar to mCherry, if only %bleach is considered. Building on the multi-beam geometry described here, other excitation schemes may be devised to separately measure the rates of both processes.

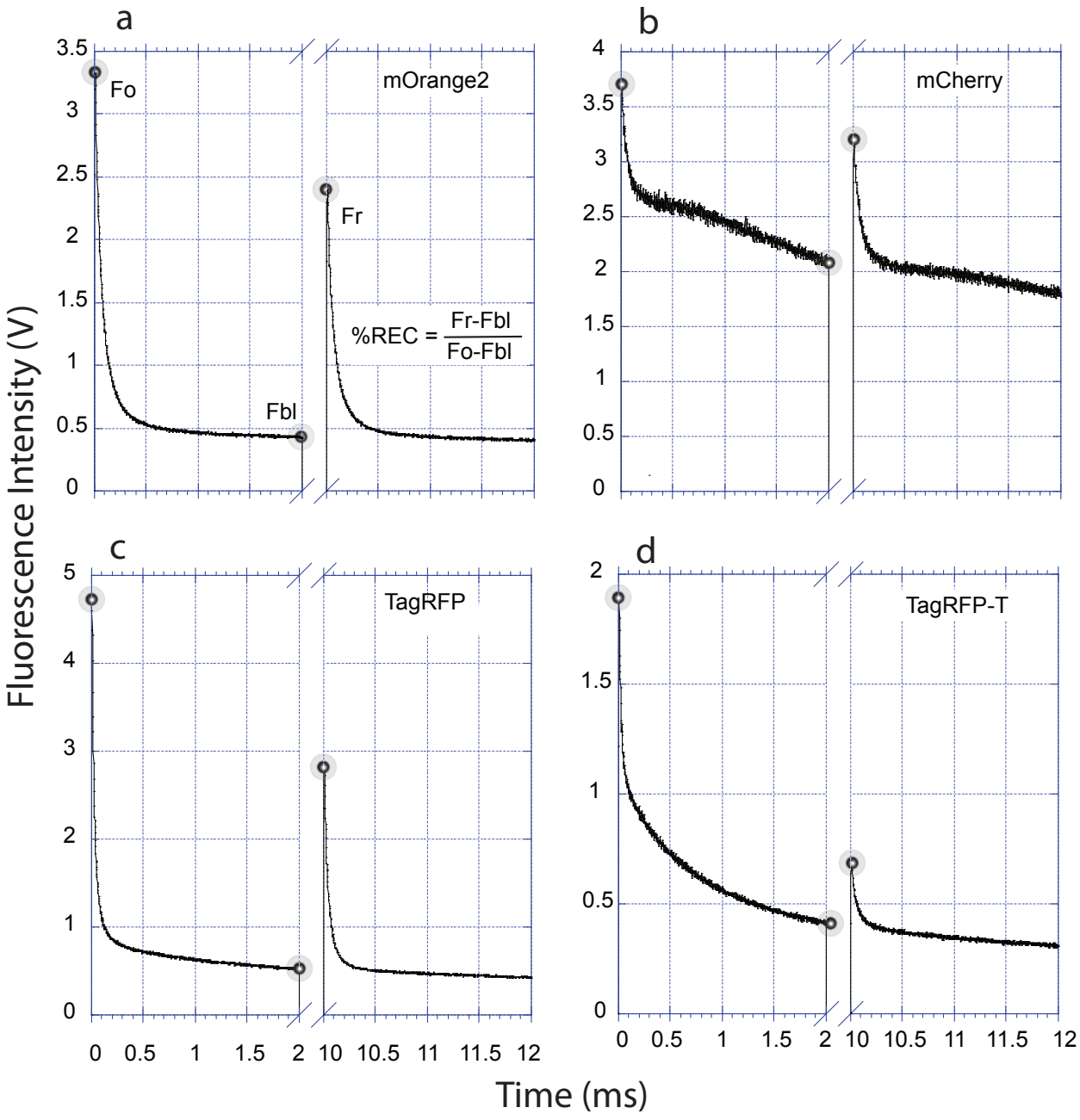

Figure 3.8: Measurements were conducted with a 2 ms, 25 kW/cm^2 pulse of illumination from a 532 nm CW laser. The cells were then kept in the dark for 8 ms allowing for fluorescence recovery before the next 2 ms pulse. This duty cycle was designed to resemble cytometry experimental parameters. However, due to experimental limitations, the intensity was reduced to an eighth of the cytometry bleach-beam (a) mOrange2 fluorescence recovery of 80 ± 5% (n=3). (b) mCherry fluorescence recovery of 92 ± 6% (n=3). (c) TagRFP fluorescence recovery of 76 ± 7% (n=3). (d) TagRFP-T fluorescence recovery of 58 ± 18% (n=3).

3.6 Conclusion

To our knowledge, this is the first cytometer designed to quantify photobleaching in mixed populations. This multibeam flow cytometer capitalizes on the spatiotemporal properties of the cells in microfluidic flow to measure photobleaching with a ratiometric approach, which inherently differs from previous experiments with one or two beams. We demonstrated the capability to characterize the individual cells within a mixed population and note that our experiment resolves two RFPs (Tag-RFP [16] and Tag-RFP-T [17]) that cannot be resolved by previously available spectral signatures (*e.g.*, fluorescence lifetime, excitation/emission spectra, absorption).

As revealed in these experiments and simulations, this three- beam pulse sequence probes both irreversible and reversible photobleaching. These two processes are highly interdependent and must be considered in tandem. To discriminate reversible from irreversible photobleaching, the excitation pulse sequence would need to operate on time scales that create a steady-state dark-state population. Generally, by controlling the cell velocity, excitation intensity, and dimensions of the beam and fluidic channel and by employing time-resolved fluorescence detection, it will be possible to implement specific probes of other photophysical dynamics, at high throughput. Furthermore, building on a recent suggestion in the literature [53], the method reported here can be integrated with measurements of fluorescence lifetime [86, 87] and microfluidic cell-sorting techniques [99,100] to enable the screening of genetic libraries of FPs on the basis of photostability and fluorescence quantum yield. Further evolution of the instrumentation towards this goal, to enable the development of more photostable FPs, is described in the next chapter.

Chapter 4

Microfluidic Cell Sorter for use in Developing Red Fluorescent Proteins with Improved Photostability

4.1 Abstract

Here we present a novel microfluidic cytometer for mammalian cells that rapidly measures the irreversible photobleaching of RFPs expressed within each cell and achieves high purity (>99%) selection of individual cells based on these measurements. The selection is achieved by using sub-millisecond timed control of a piezo-tilt mirror to steer a focused 1064-nm laser spot for optical gradient force switching following analysis of the fluorescence signals from passage of the cell through a series of 532-nm laser beams. In transit through each beam, the FPs within the cell undergo conversion to dark states, but the microfluidic chip enables the cell to pass sufficiently slowly that recovery from reversible dark states occurs between beams, thereby enabling irreversible photobleaching to be quantified separately from the reversible DSC. The microfluidic platform achieves sorting of samples down to sub-mL volumes with minimal loss, wherein collected cells remain alive and can subsequently proliferate. The instrument provides a unique first tool for rapid selection of individual mammalian cells on the merits of photostability and is likely to form the basis of subsequent lab-on-a-chip platforms that combine photobleaching with other spectroscopic measurements for on-going research to develop advanced RFPs by screening of genetic libraries.

4.2 Publication Status and Author Contributions

Davis, L.M., Lubbeck, J.L., Dean, K.M., Palmer, A.E., Jimenez, R. Microfluidic cell sorter for use in developing red fluorescent proteins with improved photostability. Submitted to Lab Chip.

J.L.L., K.M.D., A.E.P., and R.J. designed research. L.M.D. designed and built the optical trap, and also performed real-time programming. J.L.L. and K.M.D. performed research. L.M.D., A.E.P., and R.J. wrote the paper.

4.3 Introduction

In the previous chapter, we presented a microfluidic sorter capable of screening cells on the basis of the composite photobleaching process which is the concatenation of irreversible photobleaching and DSC. The microfluidic sorter described in this chapter offers the innovative capability of selecting RFPs with reduced irreversible photobleaching in mammalian cells. Irreversible photobleaching is a particularly important parameter to isolate, because it ultimately limits the number of fluorescence photons that can be collected from a single protein, which is typically 10 to 100 times fewer than that obtained from a fluorescent dye molecule [30, 49]. While DSC may be advantageous for a particular bioimaging format, irreversible photobleaching is always detrimental as it terminates single-molecule observation and limits super-resolution precision. The pathways and kinetics for DSC and photobleaching are poorly understood but in general are linked. Whereas photobleaching is caused by breaking of chemical bonds in the fluorophore, the mechanisms for DSC may include pH dependent protonation of part of the fluorophore moiety, or a conformational change of the fluorophore or its immediate environment, each with a relatively slow recovery ($\approx$10-1000 μs), and intersystem crossing to the triplet state with a faster recovery ($\approx$1 μs). The linking of the kinetics arises because irreversible photobleaching often results from absorption of light from an excited state, such as a triplet state or a dark state.

For wide-field modulated excitation of cells expressing RFP with laser pulses obtained using a continuous 532-nm laser and an AOM (cycles of 2 ms at 25 kW/cm^2 followed by 8 ms in the

dark), the fluorescence signal from various RFPs characteristically quickly decreases during each pulse due to conversion to a dark state and mostly recovers between pulses due to recovery from the dark state. Moreover, there is also a slower decrease of the maximum fluorescence signal from one pulse to the next, which provides a measure of irreversible photobleaching that is largely isolated from the faster fluorescence decrease arising from conversion into dark states [49]. To isolate and measure irreversible photobleaching in the microfluidic cell sorter, a similar modulated excitation as that formed by the AOM is achieved by allowing cells to flow at an appropriate speed through a series of laser beams upstream from the sorting region, as shown in Figure 4.1. In contrast to the traditional FACS, which employs flow speeds of 1-10 m/s, the microfluidic device enables a much slower flow, with transit times of up to ≈2 ms and with up to ≈8 ms intervals between beams, which are separated by ≈30 μm.

While the number of beams required to differentiate RFPs with substantially different photobleaching can be as few as two or three [101], a larger number of beams provides greater photobleaching and better resolution of RFPs with high photostability, and hence the instrument may be configured to use as many as 8 beams of 532-nm light to characterize photobleaching, although oftentimes only 3 or 4 are sufficient. The ratio of the maximum fluorescence signal from the final beam to that from the initial beam is independent of the level of expression of RFP within the cell and yields a simple and reliable measure of the irreversible photobleaching. In Chapter 3, this measure has been shown to be capable of distinguishing individual cells within a mixed population even when they cannot be resolved by other spectroscopic signatures, such as fluorescence lifetime, or excitation or emission spectra [101].

The microfluidic instrument described in this chapter is unique in that it combines this rapid measurement of irreversible photobleaching with immediate analysis for real-time sorting of live mammalian cells. Several methods can be used for sorting of cells within microfluidic devices. Early devices used switching of electro-osmotically driven flow [102,103], but are mostly impractical for manipulation of fragile mammalian cells [104]. Other possible cell sorting techniques include use of acoustic waves [105, 106], and fluidic displacement induced by pulsed laser cavitation bubble

formation [107]. Use of optical forces for sorting cells, which is based on early work on optical trapping of cells [108], is particularly suited for use within microfluidic devices. Optical sorting of cells in a microfluidic device has been demonstrated by switching on a tightly focused line from a 980-nm diode bar laser so cells flow along the line [109] and also by pushing a cell by the optical scattering force along the laser direction into a separate fluidic channel in a multilayer device [110]. Computer controlled holographic optical trapping with a high NA microscope objective to provide tight focusing has been reported for manipulating and sorting of human embryonic stem cells [111].

In this work, sorting using optical gradient force switching was chosen because it is compatible with a single layer microfluidic device, it does not require high NA optics and it is suitable for live mammalian cells [99]. As depicted in Figure 4.1, a single focused 1064-nm laser spot is turned on and moved at an angle across the microfluidic channel, to deflect a cell by the optical gradient force so that it follows the trajectory of the spot towards a separate exit channel. As the speed of translation of the laser spot is matched to the flow velocity, the optical force does not have to be strong enough to overcome the flow, hence strong axial trapping is not needed and only a low NA lens is required for focusing the laser beam. The technique has previously been demonstrated to maintain the viability of HeLa cells with a 1064-nm laser power of >10 W and exposure of several milliseconds, which provides sufficient optical forces for efficient cell selection [99]. Other authors have used a similar approach for sorting of mouse macrophage cells infected by a fluorescently labelled pathogen [112].

In each of these earlier works, the fluorescence signal from transit of a cell through a single laser beam was passed to a hardwired circuit with a leading-edge discriminator, which triggered custom electronics [99] or a programmed function generator [112] to drive an AOM after a pre-set delay to deflect the beam and translate the laser spot. In contrast, in the present work, analysis of the multi-beam photobleaching signature is performed in software on a separate computer using the Real-Time module of LabView (National Instruments) to achieve deterministic (about ± 0.005 ms), low-latency (< 3 ms), adjustably timed control of the sweep of the laser spot using a piezo-tilt mirror.

The instrument reported in this chapter is an application of miniaturization and automation that presents marked advantages over existing manual techniques used in developing new RFPs. Previous sorting techniques have relied on manual selection of bacterial colonies [17, 54], which is time-intensive, or fluorescence activated cell sorters (FACS), which are primarily limited to detection of fluorescence intensity, wavelength, and light scatter. In contrast to these previously used techniques, the present instrument enables high-speed automated selection of individual mammalian cells. It uses photobleaching irradiance levels similar to those used in many fluorescence imaging experiments ($\approx$2-25 kW/cm^2 [113,114]) and it achieves high purity (>99%) in the selected population, as demonstrated by experiments with known mixtures of cells. It hence provides an important new tool for efforts to develop novel RFPs with enhanced photostability and low toxicity in mammalian cells. It is likely to lead the lab-on-a-chip community to develop subsequent cell sorters that combine photobleaching with other spectroscopic measurements [115].

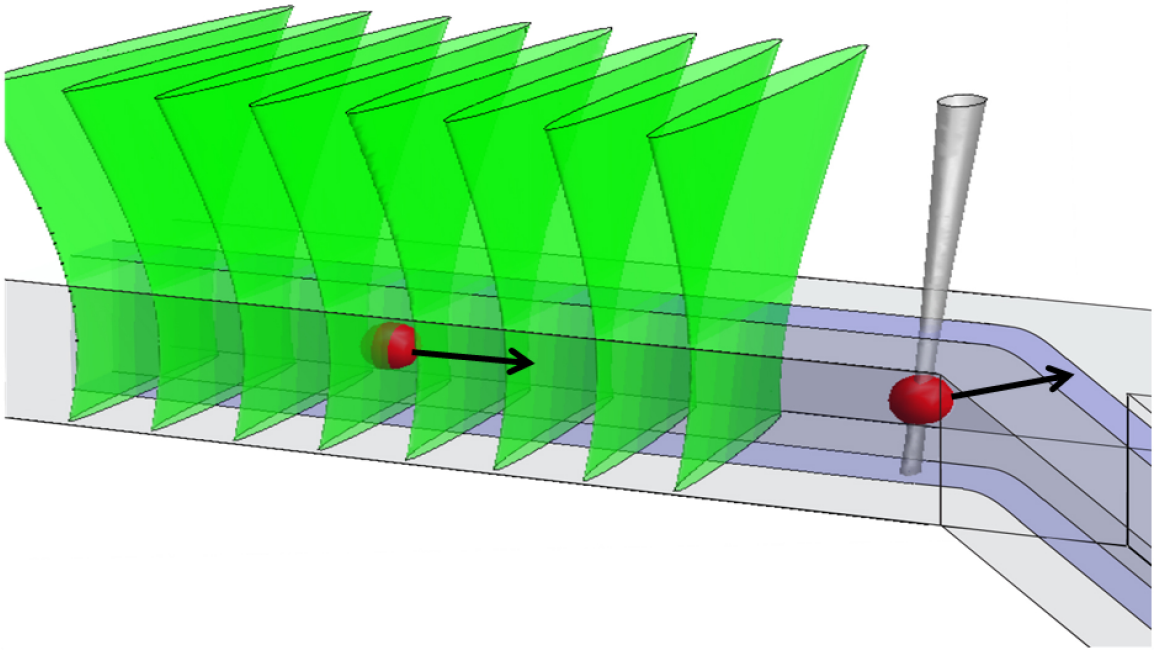

Figure 4.1: Schematic of a cell flowing through a series of line-focused 532-nm laser beams to yield a measure of irreversible photobleaching, which is used to decide its possible selection, made by turning on and translating a focused 1064-nm laser beam for optical gradient force switching.

4.4 Experimental

4.4.1 Microfluidic Chip, Microscope, and Detection

Figure 4.2 shows a schematic of the entire experimental system, with specific details for key components given in the figure or figure caption. An expanded diagram of the microfluidic chip is at the top left in the figure. The cell sorting uses up to 20 W of 1064-nm laser light, so to avoid absorption of this light by the device and possible burning or damage, the microfluidic chip (custom fabricated by Micronit, Netherlands) is made entirely from borosilicate glass. The ports of the chip are sealed to a polytetrafluoroethylene (PTFE) manifold using compression fit o-rings. For each of the 5 inlet/outlet ports, the manifold contains a reservoir connected at the top to an access hole, sealed by a cap screw, which is removed for loading and recovering samples with a micropipette, and also to a side line for delivery of compressed air to enable the headspace of the reservoir to be pressurized. The outlet reservoirs (channels E and F) are left open to atmospheric pressure and three adjustable, electronic pressure controls (Pneutronics, OEM EPS10-5-0-2) with a range of 0-2 psi above atmospheric pressure are used to regulate the inlet flow rates of the sample (in channel A, Figure 4.2) and two buffer streams (in channels B) to achieve hydrodynamic focusing of the sample stream (in channel D), and adjust its path within the microfluidic device so that it exits into the side channel (channel F).

As shown in Figure 4.2, the microfluidic chip (1) and manifold are mounted on an inverted microscope that uses a dry objective (2) for epi-illumination and collection of fluorescence. The beam from a 532-nm laser is split into 9 beams (only 5 are shown) of adjustable powers with a series of beamsplitters and neutral density filters. The beams pass through a cylindrical lens (3), enter the side port of the microscope and reflect from a dichroic mirror (4) to form line-focused beams within the microfluidic device (1) (8 of the beams in channel D, as depicted in Figure 4.1, and the 9-th monitor beam in channel E, for counting of selected cells, as discussed below). Any of the beams may be blocked, including the monitor beam; oftentimes only 4 or 5 beams are used. Red fluorescence from cells passing through these beams is isolated using filters (5, 6) (pass-band 545-

690 nm) and detected with a photomultiplier (operated at -650 V). The photomultiplier signal is conditioned by a custom-built trans-impedance amplifier (which gives 10V output for a 100 μA input and 0.16-10.6 kHz band-pass) and digitized at 125 kHz, 16-bit resolution by a multifunction data acquisition (DAQ) card (National Instruments PCI-6251 with NI-SCXI). This card also provides a digital output for switching the 1064-nm laser on/off and two 0-10 V analogue outputs for control of two actuators of the piezo-tilt mirror (7) through a low-voltage piezo amplifier. The DAQ card is operated in a separate computer (Target PC) controlled by the main computer (Host PC). For sorting of cells, the piezo-tilt mirror steers the beam from a 1064-nm laser, which is reflected from a dielectric mirror (8) and focused in through the top of the microfluidic chip by an aspheric lens (9). In order to visualize cells during operation of the sorter, trans-illumination of the chip is provided a Krypton bulb (10) and a long-pass filter (>750 nm) (11) and scattered light from cells is separated by a dichroic filter (12) for viewing with a CMOS camera.

4.4.2 Optical Design of Gradient Force Switching

The 1064-nm optical deflection beam is focused through the top cover-plate of the microfluidic device using an aspheric lens (9) with focal length f=11 mm. The lens is antireflection coated and provides high transmission (>99%) and low loss compared to a microscope objective. Although the lens is designed for use at a wavelength of 670 nm and for focusing through a laser diode window of 0.275 mm thickness with NA 0.3, Zemax optical design software indicates that when the Gaussian 1064-nm laser beam is focused by the lens through the 1.1 mm thick glass top of the microfluidic device at a NA of 0.25, the focused spot size, as seen in the inset of Figure 4.3, is close to the diffraction limited size of the Airy disk over the entire trajectory. As the depth of the microfluidic channel is only 25 μm compared to 50 μm in earlier work [99], a higher NA was chosen (0.25 rather than 0.2) to produce a sharper axial optical field gradient (the spot area doubles over the Rayleigh range of $\pm$4.1 μm rather than $\pm$6.3 μm).

The piezo-tilt mirror used to translate the focused spot within the microfluidic channel has an equilateral tripod mount that gives up to $\pm$600 μrad of tilt in total when two of the three

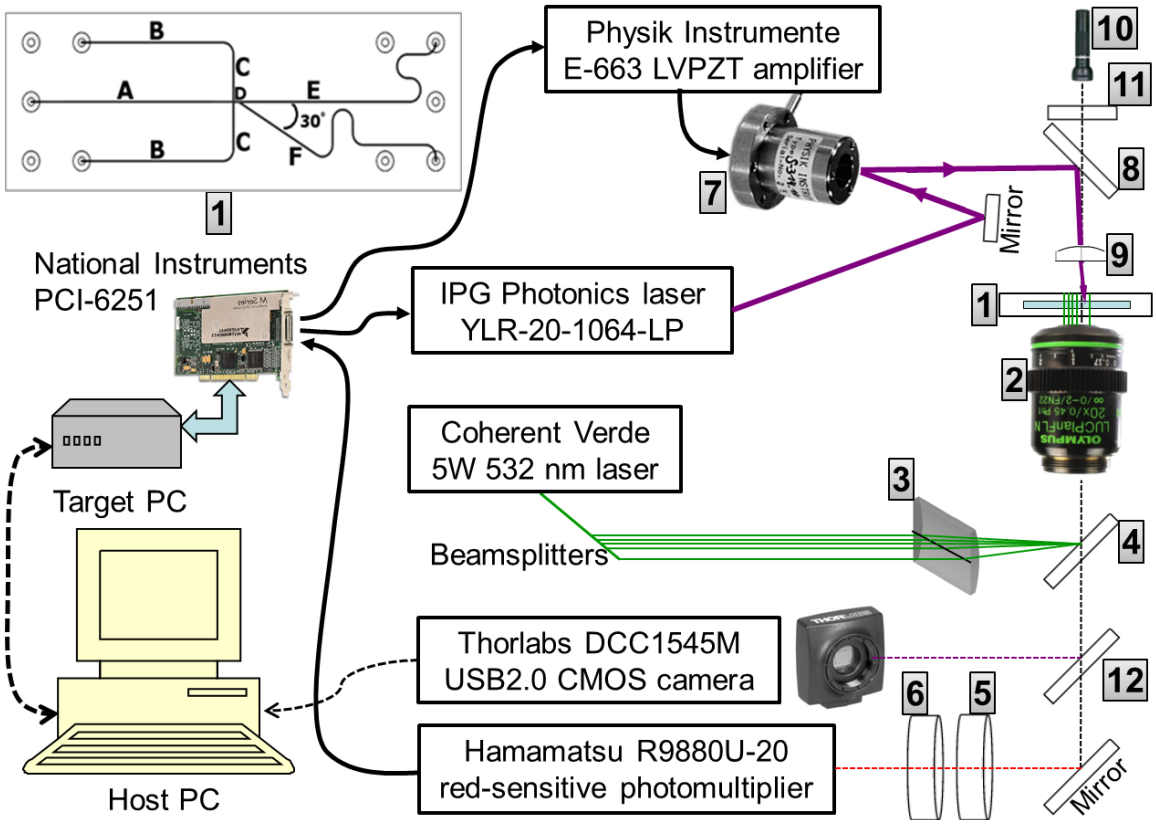

Figure 4.2: (1)=the microfluidic chip, shown within the system and at top left: Channel lengths (mm), widths (μm) are: A 20,100; B 15, 130; C 5, 130; D 0.5, 15, E 27, 125; F 27, 125. All channels are wet etched to 25 μm depth into a 0.7 mm thick borosilicate glass substrate, which is bonded to a 1.1 mm thick glass cover-plate that has powder-blasted vias of 0.6-1.7 mm (bottom-top) diameter ($\approx$1.2 μL volume). Key system components are: (2)=Olympus IX71, inverted microscope with Olympus LUC Plan FLN 20$\times$ UIS2 NA0.45/∞/cc0-2 mm objective; (3)=Thorlabs LJ1996L1-A, plano-convex cylindrical lens, focal length f=300 mm; (4)=Chroma z532 rdc, dichroic filter (reflects 532 nm, transmits >550 nm); (5)=Semrock FF01-720/SP-25, short-pass filter (transmits 320-690 nm, blocks >720 nm with optical density OD>7); (6)=Chroma HQ545LP, dichroic filter (transmits >545 nm, blocks <540 nm OD>5); (7)=Physik Instrumente S-315, piezo-tilt mirror, (8)=Newport 10QM20HM.15, dielectric mirror (reflects 1064 nm, transmits <900 nm); (9)=Thorlabs A397TM-C, aspheric lens, f=11 mm; (10)=Maglite, Krypton bulb; (11)=Semrock FF01-736/LP-25, long-pass filter (transmits >750 nm, blocks <736 nm OD>3); (12)=Semrock FF720-SDi01-25$\times$36 dichroic filter (transmits 400-700 nm, reflects 720-890 nm).

actuators are oppositely extended over their full range. The full angular tilt in a beam reflected from the mirror is two times that value, or 2400 μrad in total. If this tilt is applied at the entrance pupil of the 11 mm focal length aspheric lens, the scan distance of the spot would be 11 mm $\times$ 2.4 $\times$ 10-3 = 26.4 μm. To increase the scan distance, as shown in the optical layout in Figure 4.3, the piezo-tilt mirror (PM) is imaged onto the entrance pupil of the aspheric lens (L5) with a magnification of 3.33, using a pair of lenses (L3 and L4), which are spaced so that the collimated beam from the piezo-tilt mirror is re-collimated at the aspheric focusing lens. With adjustment of two of the three actuators, the laser spot can be scanned in the microfluidic channel over an area with longest diagonal of 88 μm. The tilt mirror is driven by a 3-channel 100 V amplifier controlled by 0-10 V analogue input signals. The minimum time taken to scan the full range is approximately 2 ms. Manipulation of beads has been demonstrated with the same piezo-tilt mirror [116].

To achieve the desired numerical aperture in focusing, the 1064-nm laser beam is expanded $\times$3.5 using a pair of plano-concave and plano-convex singlet lenses (L1 and L2) and the beam path is folded to form a more compact assembly for enclosure within a box, as seen in Figure 4.3.

4.4.3 Timing Set-Up

In setting up for sorting, the trajectory over which the 1064-nm laser spot scans is adjusted downstream from the photobleaching beams, as shown in Figure 4.4. The orientation and voltage limits of the piezo-tilt mirror are set to make a triangular trajectory, 1-2-3, shown by the dashed red line in Figure 4.4, where the 1064-nm laser turns on over path 1-2 and turns off over path 3-1. When a cell passes through the photobleaching beams (green lines at left in Figure 4.4), the signals are analyzed and if the cell is selected, the 1064-nm spot must turn on with correct start time and scan with a speed matched to that of the cell so that it intercepts the cell.

To accomplish this, the camera image is used to measure the displacements shown in Figure 4.4: A, between the first and last green photobleaching beams; B, between the last photobleaching beam and point 2 of the 1064-nm spot trajectory; C, the down-channel component between points 1 and 2 of the trajectory; and D, between the last photobleaching beam and the monitor beam,

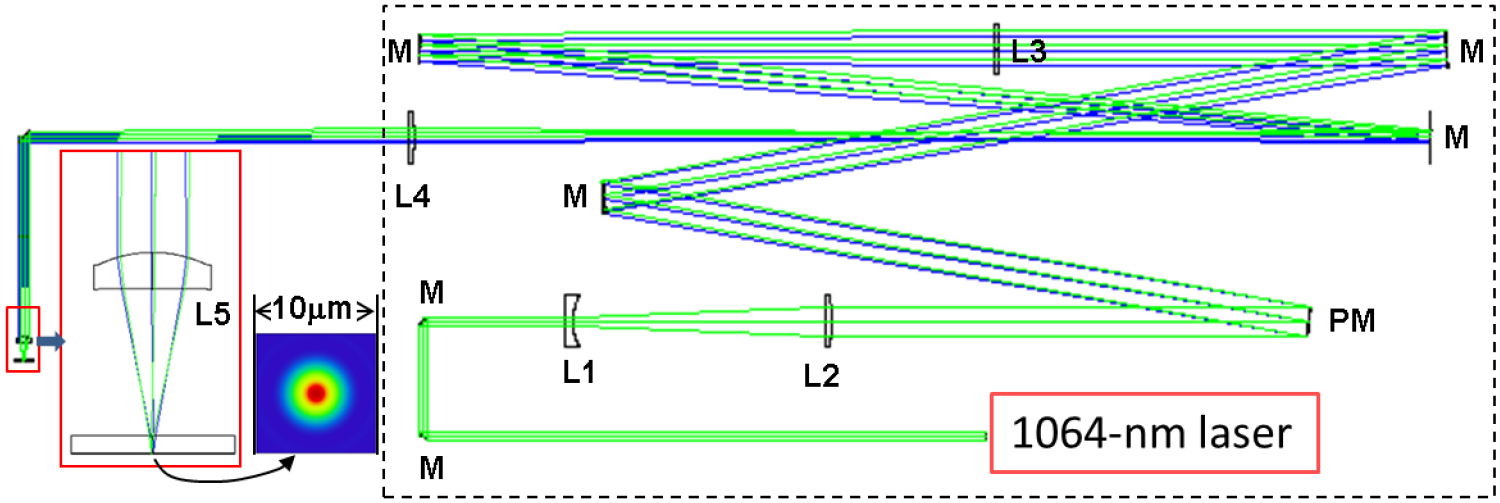

Figure 4.3: M=Mirror, PM=Piezo-tilt mirror (rays are shown for the extreme tilts), L=Lens (Thorlabs part #), L1=Plano-concave f=-50 mm (LC1715-C), L2=Plano-convex f=175 mm (LA1229-C), L3=Plano-convex f=1000 mm (LA1464-C), L4=Plano-convex f=300 mm (LA1484-C), L5=convex aspheric f=11 mm (A397TM-C). Separations between component vertices are: L1-L2=125.2 mm; PM-L3=998.5 mm; L3-L4=1289.0 mm; L4-L5= 289.4 mm. L1 orientation is reversed to balance spherical aberration. The inset shows the Huygens point-spread function of the laser beam focus.

which is positioned in the sort channel (channel E of Figure 4.2 as a means of counting cells that pass into that channel. The program on the Target PC measures T_A the time of passage of a cell between the 1^{st} and last photobleaching beams, which depends on the setting of the pressures that drive the flow. (Due to the pressure-driven parabolic flow profile, the passage time also depends on the exact depth of the cell within the channel, but all cells are carried close to the centre depth where the flow speed is greatest, so the variation is found to be only ± 9 % at most.)

The start time of the trajectory of the 1064-nm spot is adjusted so that the time delay T_B from the moment that a cell passes the last photobleaching beam to the time when the 1064-nm spot passes point 2 in its trajectory is T_B = (B/A) T_A. The speed of the trajectory along path 2-3 is adjusted so that T_C = (C/A) T_A. Finally, the delay for recognition of a cell passing through the monitor beam is T_D = F (D/A) T_D, where a factor of F ≈ 1.67 is used to account for a slow-down in the flow speed beyond the channel junction, as the microfluidic device is designed with a main channel of width 150 μm and two exit channels each of width 125 μm, so that the net flow speed slows by a factor of 0.6 (=1/1.67). If the monitor beam is used, a peak that follows one from a cell passing the last photobleaching beam within a delay of (1±δ) T_D is categorized as due to that same cell passing through the monitor beam, where $\delta \approx 0.1$ is a tolerance parameter. However, such a peak could also be due to a new cell entering beam 1 with the required delay. Thus the monitor beam gives a useful indication of successful cell selection for optimizing efficiency, but the categorization of peaks on the basis of their timing leads to over-counting of sorted cells, particularly when the incoming rate of cells is high, and hence it provides only a low-limit estimate for the purity of the selected cells. As discussed below, the purity of the selected cells is better determined by subsequent spectroscopic analysis of the selected population of cells.

4.4.4 Real-Time Data Analysis for Cell Selection

A program operating on the Target PC is used to analyse the digitized data stream from the photomultiplier, recognize isolated bursts composed of sets of peaks due to the passage of cells through the of 532-nm photobleaching beams, make selection decisions based on photobleaching,

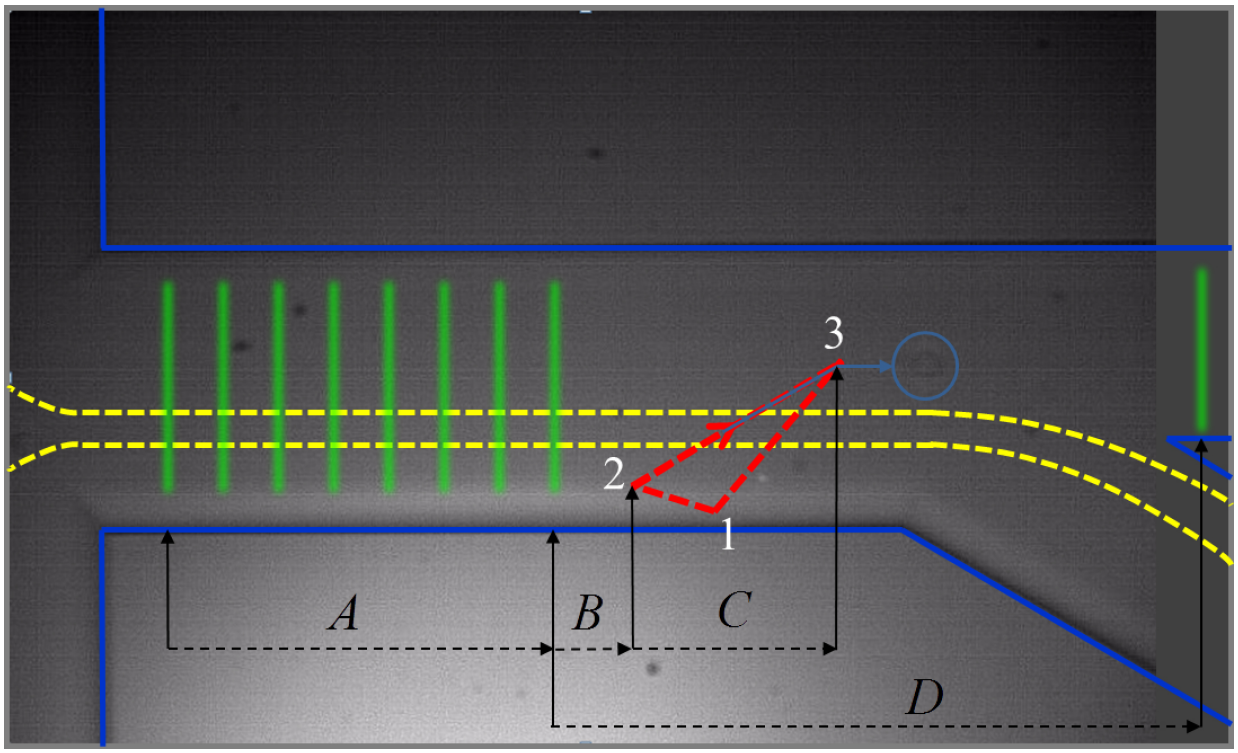

Figure 4.4: The 8 green lines at left represent line-focused 532-nm fluorescence excitation beams. The red dashed triangle is the trajectory of the 1064-nm optical deflection laser spot. The dashed yellow lines envelope the trajectories of cells as they pass into the exit channel at lower right. The image in this camera frame has captured a cell that was deflected along the light blue line to point 3, is now within the light blue circle, and will subsequently pass into the sort channel at upper right, to be counted as it passes through the 9-th 532-nm laser line at far right.

program the DAQ card outputs using the calculated timing for cell selection, and count cells that pass through the monitor beam if this is used. With low priority, this program also transmits analysis results to the Host PC and adjusts its operating parameters upon command from the Host. The Host runs a separate interactive program that graphically presents analysis results received from the Target and allows parameters to be transmitted to the Target for update.

4.4.4.1 Target PC Program

Table 4.1 gives a flow diagram of the main parts of the algorithm of the Target PC program, which finds peaks, counts them into bursts, and categorizes and counts bursts of different types. In the main loop, at line 9 the program awaits a block of data (typically 625 points in 5 ms), then at line 10 it finds the locations and amplitudes of peaks in the data stream using the LabView library routine Peak Detector, which is a point-by-point routine that retains needed data from prior calls. This finds peaks above an adjustable level (set at the current average plus an adjustable threshold so as to recognize a wide dynamic range but yet distinguish partially overlapping peaks) by fitting a quadratic of given width to the data stream (so that peaks of small width due to noise are not found). In the for-loop of lines 1137, the timings of peaks are used to count up peaks into bursts. The count, i, is reset to the beginning value (i = 0;) designating the first peak of a burst whenever the time since the last peak is not within the set limits (between $\underline{\text{Min}}$ and $\underline{\text{Max}}$ at lines 17 or 24, or for the monitor between (1-$\underline{\delta}$) $\underline{T_D}$ and (1+$\underline{\delta}$) $\underline{T_D}$ at line 33), or whenever the count equals the number of laser beams used (at lines 27 or 36). If this first peak follows the previous peak too closely, the burst that follows will be flagged as overlapping (line 40 or 41). An array (A[ ]) is used to store the amplitude of the first peak and the normalized amplitudes of subsequent peaks in a burst. After a cell has passed through all photobleaching laser beams, if all the amplitudes are between the lower limits and upper limits (which are defined in the arrays LL[ ] and UL[ ], *i.e.*, LL[j]<A[j]<UL[j] for j=0,1, , N) and the burst is not overlapping with a prior one (O=false at line 21), the time and speed for the motion of the 1064-nm laser spot is calculated (line 22, Calculate timing) using the procedure discussed in section 4.4.3, taking into account the positions of the peaks

in the data stream and the amount of time that has elapsed during the computation, as determined from readings of the Target PC clock. If the piezo-tilt mirror has completed its previous trajectory and if there is sufficient time to intercept the cell, a subprogram (line 22, Initiate selection), which will send the calculated voltages from the DAQ card with the calculated timing, is started; at this time the flag for Selected is set true.

After the peaks are counted for a cell passing through all photobleaching beams, the next peak will be reset to the beginning of a new burst if the monitor beam is not used (line 27) or will be tested to see if it corresponds to a monitor peak (line 30), in which case the next peak will be reset to the beginning of a new burst (line 36). With completion of a burst in either of the two cases of these possible resets after all photobleaching beams are counted, the type of the burst is determined and a counter for the particular burst type is incremented. Note that (in line 21) a burst may be selected only if it does not overlap with the prior burst. However, whether selected or not, it will be designated as overlapping if it overlaps with either the prior or the following burst (lines 27, 28 or 33, 34, or 36, 37).

4.4.4.2 Host PC Program

Figure 4.5 shows a screen shot of the Host PC program, captured during the execution of an experiment. The program, which runs on a PC that uses the Windows 7 operating system, receives the time and amplitude of each detected fluorescence peak over the network from the Target PC. It groups these peaks into bursts of peaks using the same algorithm that runs on the Target PC (as described above), but with its own (Host) values of adjustable parameters, to determine graphical representations of the passage of individual cells, and also the would-be sorting statistics displayed in the top right yellow box, *i.e.*, those that would be obtained on the Target PC if that had used the same parameters. Thus at the start of an experiment, the parameters on the Host PC can be adjusted to optimize the grouping of peaks into bursts. These revised parameters can then be downloaded over the network to replace the parameters used by the Target PC, or otherwise discarded and replaced by values uploaded from the Target PC. The Target PC also collects its

Table 4.1: Flow Diagram of Target Algorithm

```
1  N = 2, 3, 4, 5, 6, 7, or 8 = number of photobleaching beams used
2  M = 0, or 1 = if monitor beam is blocked, or used
3  i = N + M; // initialize count of peaks in the present burst
4  S = false; // initialize flag S to indicate if the burst is selected
5  O = false; // initialize flag O to indicate if the burst overlaps with the prior one
6  sou = 0; nou = 0; som = 0; nom = 0; sgu = 0; ngu = 0; sgm = 0; ngm = 0;
7  // initialize counters of bursts, s/n = selected/not selected, o/g = overlapping/good,
   m/u = monitored/unmonitored
8
9  Read block of data points, find the Average
10 Call Peak Detector (Threshold + Average, Width )
11 For each peak found {
12     Find Δt = time since last peak, A = peak amplitude
13     if ( i = 0, 1, , N-2 ) { // peak that precedes last photobleaching beam
14         if ( Min < Δt < Max ) {
15             i++; A[i] = A / A[0]; }
16         else {
17             Reset; } }
18     else if ( i = N-1 ) { // peak may be due to last photobleaching beam
19         if ( Min < Δt < Max ) {
20             i++; A[i] = A / A[0]; S = false;
21             if ( LL[ ] < A[ ] < UL[ ] and O = false ) {
22                 Calculate timing; Initiate selection; S = true; }}
23         else {
24             Reset; } }
25     else if ( i = N ) { // peak that follows that from last photobleaching beam
26         if ( M = 0 ) { // if no monitor beam is used
27             O2 = O; Reset;
28             if ( O or O2 ) { if ( S ) { sou++; } else {nou++; } } else { if ( S ) { sgu++; }
               else {ngu++; } } }
29         else { // if a monitor beam is used, i.e., M = 1
30             if ((1-δ) T_D < Δt < (1+δ) T_D ) {
31                 i ++; }
32             else {
33                 O2 = O; Reset2;
34                 if ( O or O2 ) { if ( S ) { sou++; } else {nou++; } } else {
                   if ( S ) } sgu++; }
                   else { ngu++; } } } }
35     else if ( i = N+1 ) { // peak that follows that from monitor beam
36         O2 = O; Reset;
37         if ( O or O2 ) { if ( S ) { som++; } else {nom++; } } else { if ( S ) { sgm++; }
           else { ngm++; } } } }
38 Go to line 9
39
40 Reset: i = 0; A[0] = A; if (Δt < Max ) { O = true; } else {O = false; } Return;
41 Reset2: i = 0; A[0] = A; if (Δt < (1+δ) T_D ) { O = true; } else {O = false; } Return;
```

[a] Adjustable parameters are underlined; ++ means increment the counter by 1.

own (true) statistics, which are sent to the Host PC and displayed in the light blue region near top right.

The adjustable parameters (indicated by pink numbered arrows) are: (1) Threshold, (2) Width, which together are used by the LabView point-by-point library routine *Peak Detector* to find the locations and amplitudes of peaks in the data stream; (3) Minimum (time delay), and (4) Maximum (time delay), which are used together with counting of the peaks in a burst to piece together the peaks into bursts of up to 8 peaks and to determine whether a burst is overlapping with a previous burst (designated as Overlapping) or not overlapping (designated as Good); (5) a set of Switch Parameters, which define the voltages at the 3 vertices of the piezo-mirror triangular trajectory(A0, A1, B0, B1, C0, C1), the time for motion along the legs of the trajectory, 12 (designated as T_AB), 23 (designated as T_BC and readjusted to be T_C), and 34 (designated as T_CA), the ratios *B/A* (Switch-Time Factor), *C/A* (Delay Factor), and F (*D/A*) (Check Delay Factor) needed to calculate the timings, the tolerance parameter δ (Tolerance) for designating a peak as due to a cell passing through the monitor beam, and an additional parameter (Extra Delay) to provide an empirically determined offset to T_B to account for slow-down of the flow near the junction and latency of the switch; (6) a set of values for peak amplitude ratios (listed within the green box), set by using the mouse to position cursors on the graph labelled *Normalized Peak Amplitudes*. These values select the photobleaching characteristics of cells that we wish to switch to the upper exit channel.

Note however, that the switch will only be attempted if the burst of fluorescence peaks from the cell is designated as Good (not Overlapping). The switch will also not be attempted if the calculated time to wait until the start of the switch cycle (shown as usToWait at lower left in Figure 4.5) is negative, in which case the cell is counted as Too Fast (in blue box at top right Figure 4.5); or if the piezo-mirror trajectory from the previous selection will not be completed in time, which is counted as Busy (in blue box at top right Figure 4.5). After the peak of a burst as a cell passes the last photobleaching beam, whether the switch of the cell is selected (S) or not selected (NS), a peak that follows within a delay of $(1\pm\delta)\,T_D$ is categorized as due to that same

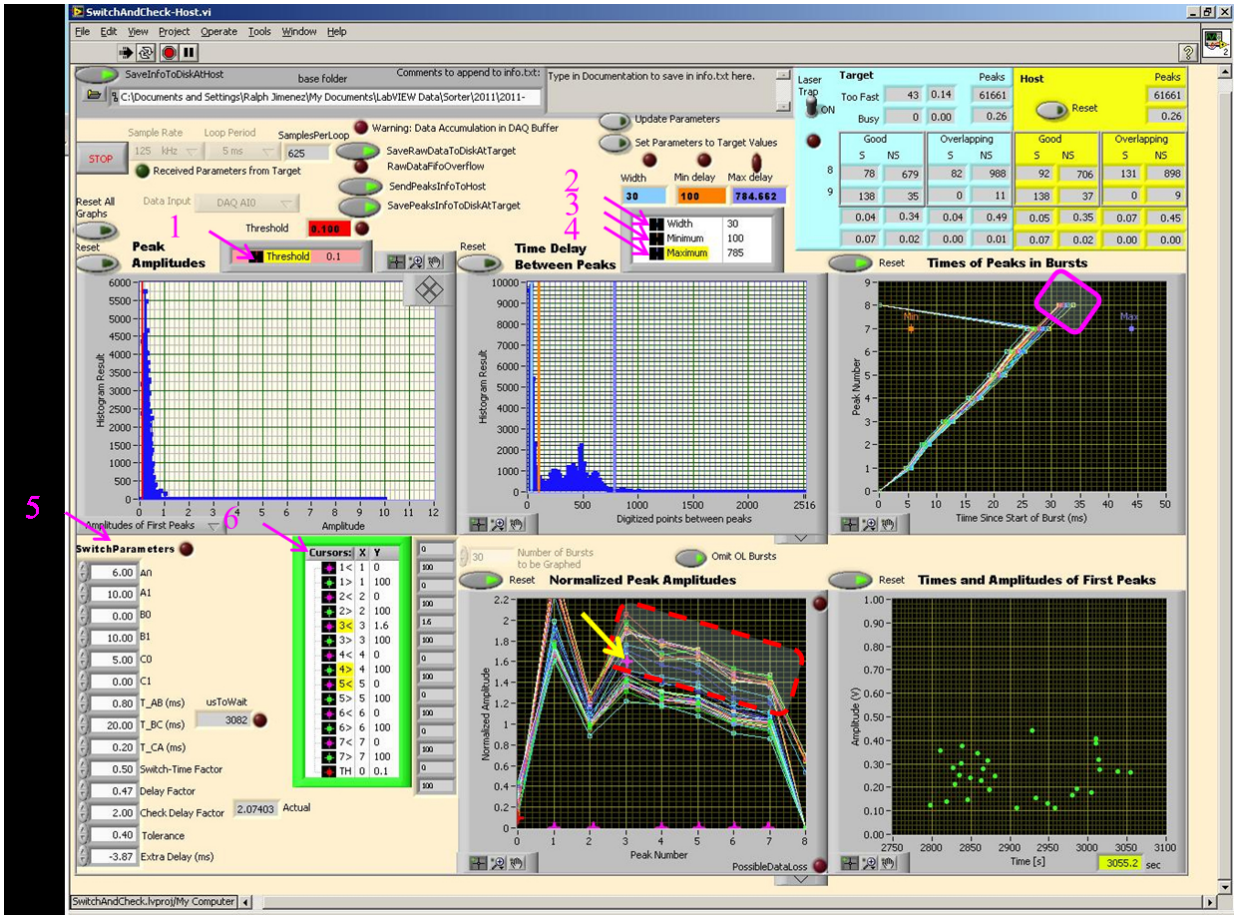

Figure 4.5: During this particular experiment, the 532-nm laser power was 0.98 W, with ≈ 0.1 W in each of the 9 beams, while the 1064-nm laser power was 14 W. The flow speed was 8 mm/s (240 μm/30 ms) and the time for the 1064-nm spot to move from 2 to 3 in Figure 4.4 was ≈ 15 ms.

cell passing the monitor beam and the burst is designated as having 9 peaks, but this may also be due to a new cell passing into beam 1. Thus the monitor beam provides an indication of a successful cell selection useful for setting up the instrument (and is visually indicated by extending the line in the graph of *Times of Peaks in Bursts*, as highlighted within the pink diamond shape in Figure 4.5), but as discussed earlier, it over-counts the cells that pass into the sort channel (the bursts that have 9 peaks), particularly those cells that were not selected. While the success of a sort must ultimately be determined by further analysis of the sorted population of cells (as is reported in section 4.5.3), the monitor beam provides data from which a lower limit of the purity of the sort can be determined. For the data displayed in Figure 4.5, this is: Relative purity > 9GS/(9GS+9GNS) = 138/(138+35) = 0.8.

4.4.5 Solution and Flow Conditions

In typical operating conditions, the speed of HeLa cells through the 532-nm beams is ≈6-8 mm/s. It is possible to operate about 3 times faster, which still gives enough time for dark-state relaxation between beams, although the camera frame rate then becomes too slow to follow cell selection. A faster flow rate not only speeds sorting, but it helps prevent cells sticking to the walls of the microfluidic device, particularly at the apex of the junction.

To reduce the HeLa cells sticking or settling in the reservoirs, OptiPrep^{TM} (60% weight/volume iodixanol in water) is added to the buffer for the cells. The iodixanol increases the specific density to make the cells buoyant, but the refractive index of the solution also increases. Hence to maintain a difference between the refractive index of the medium and the cell, as needed to generate optical forces, the concentration of iodixanol is kept at ≈8% weight/volume, similar to that used in earlier work [99], resulting in a refractive index of 1.3479 (≈1.36 for cells) and density of 1.049 g/ cm^3 (1.0357 g/cm^3 for HeLa cells [117].

4.5 Results and Discussion

4.5.1 Instrument Operating Conditions

Figure 4.6 shows a series of images captured by the camera of a HeLa cell passing through the 8 photobleaching beams (1, 2), being selected by the 1064-nm beam (3, 4), and then passing towards the selection channel (5, 6) and through the monitor beam (7).

The program only attempts to select cells that pass through the series of beams alone, without overlap between preceding or following cells. A greater number of 532-nm beams may provide better resolution of differences in irreversible photobleaching. However, there is an advantage to using fewer beams that span a smaller length of the microfluidic channel and to blocking the extra beam that is used to monitor cells passing into the sort channel–namely, the use of a smaller length of the flow channel reduces the overlapping of bursts from successive cells, which increases the effective rate at which cells may enter the sorter and be non-overlapping. In the approximation that cells enter at random times at a rate R, the time between cells is exponentially distributed with mean $1/R$, so the probability that a cell does not overlap with the prior or following ones is e^{-2RT}, where T is the passage time from the first to the last beam. The maximum rate of non-overlapping cells (labeled Good in Figure 4.5) is then $R_G = 1/(2T_e)$ when $R = 1/(2T)$. Both the rate of cells and their speed through the microfluidic device may be controlled by adjusting the pressures that drive the flow of the sample and the buffer streams. For the experiment of Figure 4.5, the time of passage from beam 1 to beam 8 (240 μm) is 30 ms, and from beam 1 to beam 9 (400 μm) is ≈113 ms, hence the maximum rate at which cells may be selected is $R_G \approx 1.6$ s^{-1}, or if the monitor beam and the check for successful switching are turned off, $R_G \approx 6.1$ s^{-1}. The actual selection rate will be $R_G\times$ the fraction of cells in the sample that have the desired photostability. As an indication of the fastest practical selection rate that can be expected, when the number of beams is reduced to 4 spread over ≈100 μm and the speed is increased by a factor of 3, so that $T = 4$ ms, the maximum rate of selectable cells is $R_G = 46$ s^{-1}, which enables samples of $\approx 10^5$ cells with enhanced photostability to be obtained within a few hours.

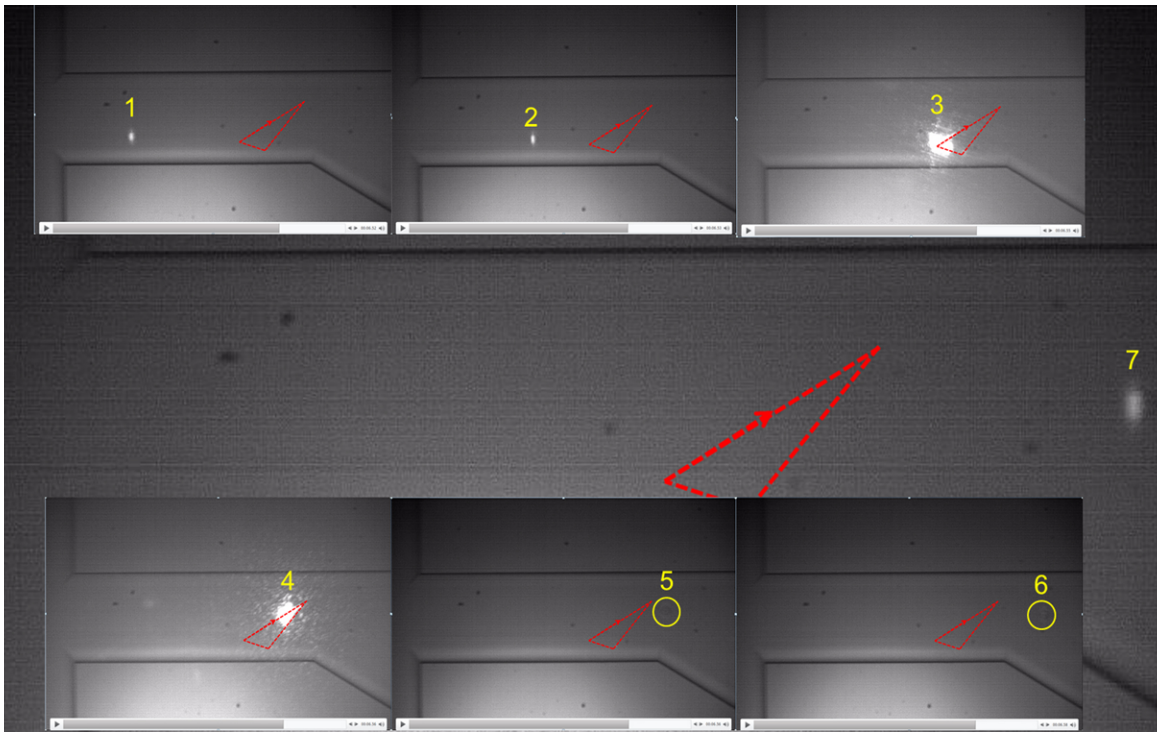

Figure 4.6: Series of images from a movie demonstrating cell selection. A HeLa cell passes through the 8 photobleaching beams (1, 2), is selected by the 1064-nm beam (3, 4), and then passes towards the selection channel (5, 6) and through the monitor beam (7).

4.5.2 Cell Selection Efficiency and Viability After Selection

To optimize operating conditions, experiments evaluating the selection efficiency and subsequent cell viability as a function of buffer conditions and 1064-nm laser power were undertaken using HeLa-S cells, which are suitable for use in experiments for developing new RFPs. To promote cell viability, especially during sorting experiments lasting longer than an hour, cells were suspended in a solution of phenol-red-free Minimum Essential Medium (Invitrogen, 41061-029), with 10% FBS (Invitrogen), 14% Optiprep (Sigma-Aldrich), and 1% Penicillin Streptomycin (Invitrogen, Pen Strep). This medium was chosen instead of a low-nutrient buffer (*e.g.*, HEPES-buffered Hanks Balanced Salt Solution), as it was found to give increased cell viability over time. Also, a medium free of phenol-red pH indicator was chosen to decrease background fluorescence.

Selection experiments using four photobleaching beams and the monitor beam for assessing success were performed for various 1064-nm laser powers using either (i) the cell suspension medium described above, or (ii) a buffer solution composed of calcium-, magnesium-, phenol-red-free Hanks Balanced Salt Solution (Invitrogen, 14175) with 1% Bovine Serum Albumin (Sigma-Aldrich, BSA) in the side channels (B of Figure 4.2) used for hydrodynamic focusing. In these experiments, the speed of cells through the photobleaching beams was kept constant at 6 mm/sec. The sample cell concentration was diluted to ≈250,000 cells/ml to decrease the rate R of cells entering the sorter and thereby decrease the probability of overlapping bursts and also increase the fidelity of the monitor beam for counting of successful selection events. For each power and fluid condition, 100 cells were assayed. As shown in Figure 4.7, the selection efficiency was found to be increased for the same 1064-nm laser power by using buffer in the side channels instead of media (possibly because the buffer contains no Optiprep and so leads to greater refractive index contrast and optical forces).

The viability for each 1064-nm laser power was then assessed for both solution conditions. In earlier work [99], mammalian cell viability was quantified by a trypan blue exclusion assay about 1 hour after exposure to the 1064-nm laser beam. However, this assay only accounts for immediate deterioration of the plasma membrane, and cannot identify cells in earlier stages of necrosis or

apoptosis. To account for slower forms of cellular death, the cell viability was measured 24 hours after microfluidic analysis for both sorted and non-sorted cells using a Calcein-AM based assay. Calcein-AM (Invitrogen) was added directly to the cells (final concentration of 1 mM) within a 96-well plate and allowed to incubate at room temperature for 30 minutes. Calcein-AM becomes fluorescent upon hydrolysis of the acetoxymethyl moiety by intracellular esterases. In contrast, dead cells remain non-fluorescent, or very weakly fluorescent, and can be identified by comparison of fluorescence and differential interference contrast (DIC) images. Using this method, for higher laser exposure conditions, cell viability was found to be decreased after 24 hours relative to the same assay when performed immediately after microfluidic sorting. Also, the viability was lowered when buffer was used in the side channels. However, the viability for each 1064-nm laser power was found to be identical (≈80%) when the selected cells were delivered into an on-chip reservoir pre-loaded with 750 μL of the running media to minimize the cells time spent in buffer to ≈0.5 sec (approximate transit time from interrogation region to outlet). Furthermore, cells were capable of continued replication over the course of several weeks.

4.5.3 Cell Selection Based on Irreversible Photobleaching

To demonstrate the effectiveness of the instrument for selecting cells that have RFPs with lower irreversible photobleaching, experiments were performed using samples containing known mixtures of HeLa-S cells expressing either mCherry (25% of cells) or mOrange2 (75% of cells). In these tests, the instrument was configured to use 4 photobleaching beams and a monitor beam, with 0.09 W of power in each photobleaching beam (peak irradiance $\approx 2 \times 10^4$ W cm^{-2}). The flow speed of cells through the beams was 6.0 mm s^{-1}. As shown in Figure 4.8, the ratios of the peak amplitudes (beam 4/beam 1) are ≈0.63 for cells with mCherry, and ≈0.40 for cells with mOrange2, whereas in a separate experiment using fluorescently labelled beads (Invitrogen, F-8858 fluospheres, 4 μm, 580/605) the ratio is ≈0.98. The operating parameters were adjusted to select mCherry cells with lower irreversible photobleaching from the mixture using a 1064-nm laser power of ≈12 W. Over a duration of ≈2.5 hours, 4000-5000 cells were selected. The purity of the selected sample

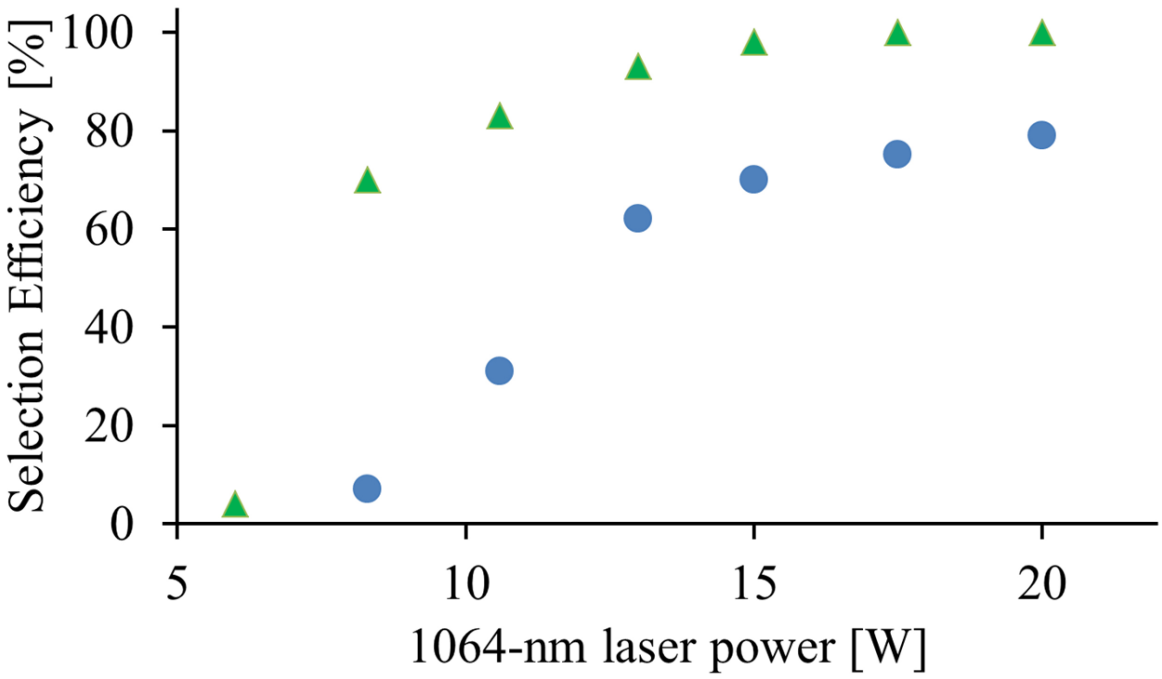

Figure 4.7: Cell selection efficiency vs. 1064-nm laser power for: (i) cell suspension medium (lower curve, •), or (ii) buffer without Optiprep (upper curve, ▲), in the side channels used for hydrodynamic focusing.

was then determined by imaging it using a wide-field fluorescence microscope in which mCherry and mOrange2 cells are spectrally distinguished by use of a set of appropriately chosen band-pass excitation filters (540/25 and 577/20). Figure 4.9 shows the spectra for these filters together with the excitation spectra of mCherry and mOrange2. As seen in Figure 4.10, the ratio of the fluorescence signals seen with each of these filters enables cells expressing mCherry or mOrange2 to be unequivocally distinguished. The purity of the selected sample was thus determined by counting the cells of either type in the image. As seen in Figure 4.11, cells expressing RFPs with lower irreversible photobleaching (mCherry) are selected from the mixture with greater than 99% purity, which is considerably higher than that typically achieved in FACS and other prior reported microfluidic cell sorters [99].

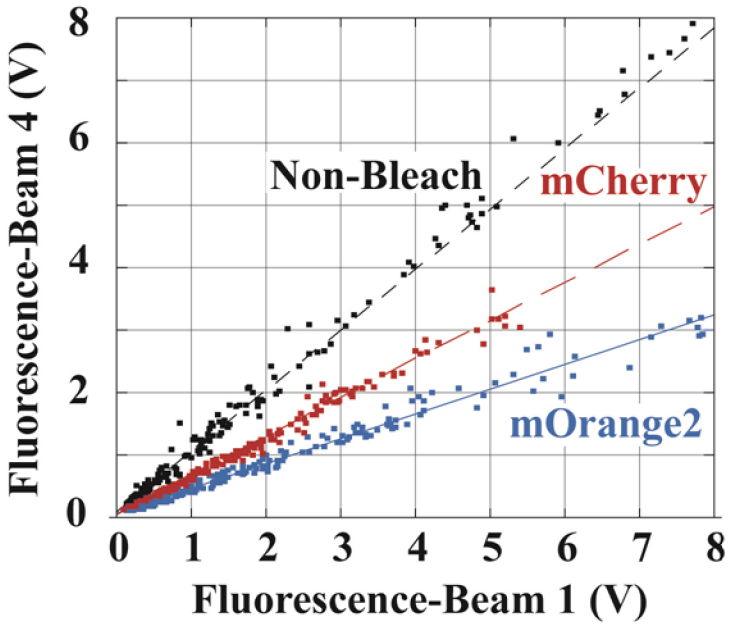

Figure 4.8: The non-bleach assay is obtained using fluorescent beads labelled with small molecule dyes that demonstrate negligible photobleaching in the cytometer (Invitrogen, F-8858 fluospheres, 4 μm, 580/605). The mCherry and mOrange2 curves are obtained from a mixture of HeLa-S cells expressing either mCherry or mOrange2. Note that mCherry is more photostable than mOrange2 under these excitation conditions.

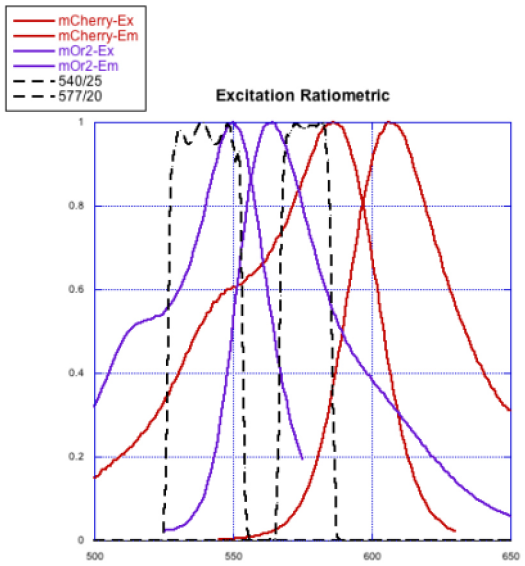

Figure 4.9: The fluorescence excitation (left) and emission (right) spectra of mOrange2 (solid purple curves) and mCherry (solid red curves) and the transmission (dashed black curves) of the two fluorescence excitation filters, 527-553 nm (left) and 567-587 nm (right). The identity of imaged cells is determined from the ratio of the fluorescence signals obtained from each of the excitation bands.

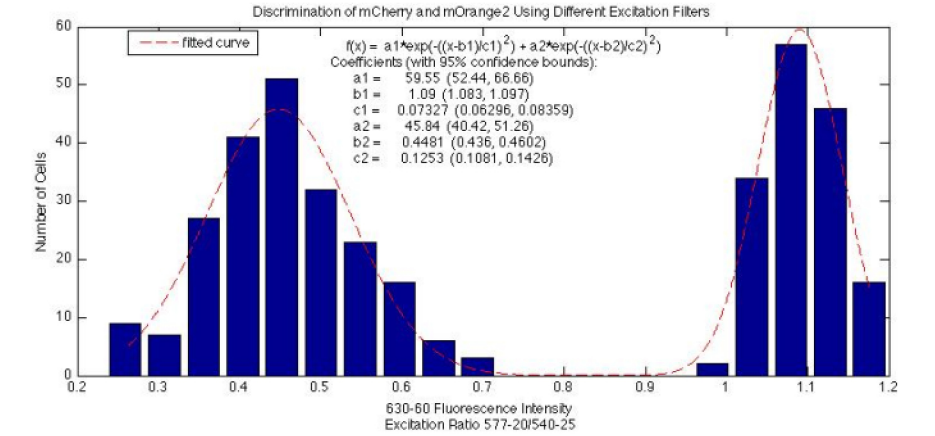

Figure 4.10: Histogram of Ratiometric Excitation (*i.e.*, fluorescence for 567-587 nm excitation / fluorescence for 527-553 nm excitation) showing clear resolution of mCherry cells (right peak) from mOrange2 cells (left peak).

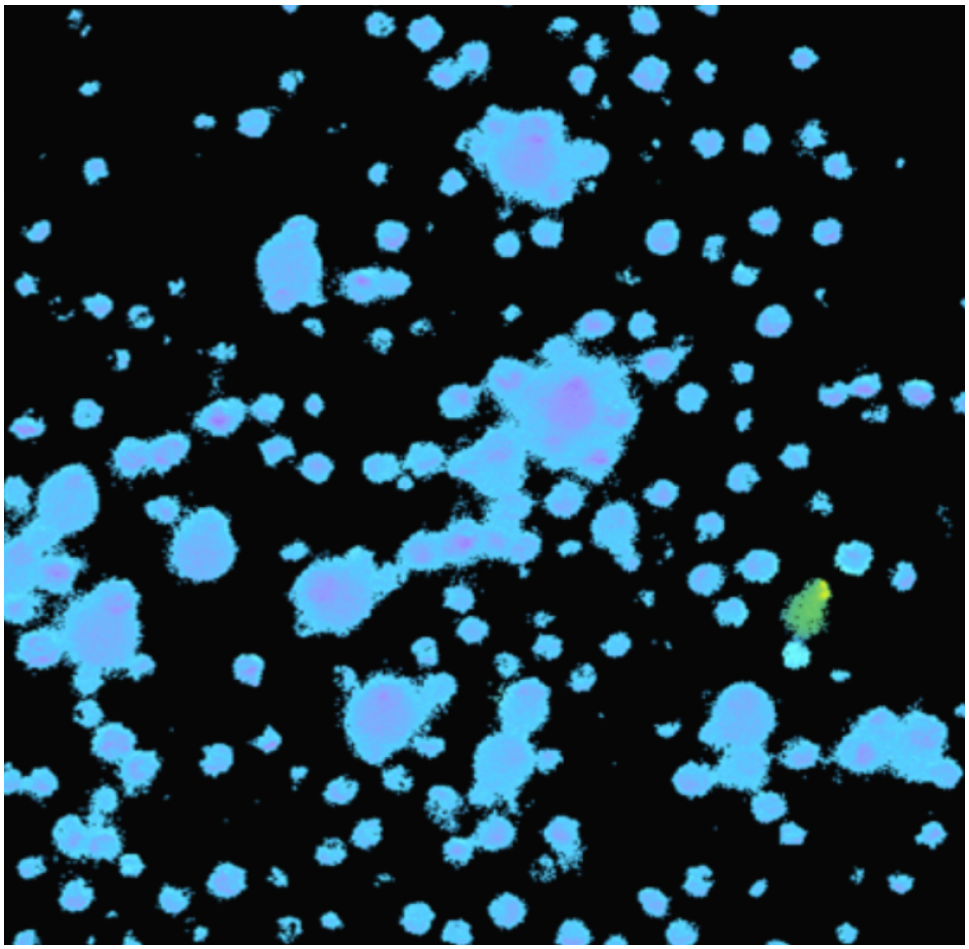

Figure 4.11: Blue/pink pseudo color represents cells expressing mCherry; green pseudo color represents mOrange2. Only one cell expressing mOrange2 is visible. Larger diameter objects are clusters of cells in close enough proximity that their edges are not resolvable.

4.6 Conclusion

This chapter reports a novel microfluidic cell sorter for live mammalian cells expressing RFPs that enables selection of cells with proteins that have enhanced photostability. The instrument uses the Real-Time module of LabView for analysis of multi-beam laser-induced fluorescence signals to determine irreversible photobleaching and to achieve sub-millisecond timing of the sweep of a 1064-nm laser spot to deflect individual selected cells by the optical gradient force to a separate collection channel. Suitable cell suspension media and laser operating conditions have been determined for efficiently selecting HeLa cells while maintaining their long-term viability and capability to proliferate. The effectiveness of the instrument has been demonstrated by selecting cells expressing a FP with higher photostability (lesser irreversible photobleaching) at a rate exceeding 0.5 s^{-1} from a sample containing a known mixture of cells expressing either mCherry (25%) or mOrange2 (75%). Subsequent analysis of the collected cells on the basis of differences in the fluorescence excitation and emission spectra of mCherry and mOrange2 found that >99% of the selected cells express mCherry, indicating a remarkably high purity in the selection. In the next chapter, this instrument is employed to develop new FPs with improved photostability.

Chapter 5

Using the Microfluidic Cell-Sorter to Sort Red Fluorescent Protein Libraries

5.1 Abstract

Here we present the successes and limitations of our microfluidic cell-sorter when used to sort and screen genetic libraries of RFPs expressed in HeLa cells. The results of screens were analyzed to determine if the library showed sufficient diversity to be sorted. A diverse library was identified and subjected to three rounds of sorting. The results demonstrate a population shift towards greater photostability after one round of sorting. The remaining mutants were analyzed and a novel mutant with $\approx 3\times$ the photostability of mCherry was discovered. However, this photostability increase was at the expense of a decreased quantum yield. The mutants with increased photostability were then subjected to additional mutagenesis in order to further increase photostability in future rounds of sorting. The successes of these first attempts at directed evolution highlight the power of this instrument while illuminating how to properly exploit them. Furthermore, the shortcomings of these attempts guide future library designs, sorting methodologies and instrument improvements.

5.2 Publication Status and Author Contributions

The work presented here is unpublished.

K.M.D., J.L.L., A.E.P., and R.J. designed research. K.M.D. designed fluorescent protein libraries. K.M.D. and J.L.L. performed research. K.M.D. performed spectroscopic measurements and data analysis.

5.3 Introduction

Currently, most new RFPs are developed by sorting libraries by automated colony pickers, manual selection of colonies, or FACS [17,18,53]. These automated approaches are higher throughput and therefore less time-intensive, however, they are typically limited to detection of fluorescence intensity, wavelength, and light scatter. Manual techniques provide more flexibility of the selection criteria but are very low throughput, limiting library sizes to 10-1,000s, or limiting the assayed-population of the library [16, 18]. This has resulted in most RFPs being optimized on the basis of brightness, maturation, or excitation/emission wavelengths [16–18, 20].

Irreversible photobleaching is a particularly important parameter to isolate, because it ultimately limits the image acquisition time and the number of emitted photons that can be collected from a single protein (which remains orders of magnitude fewer than a fluorescent dye molecule [30, 49]) [51, 114]. In the previous chapter, we reported an instrument with marked advantages over the aforementioned, existing sorting techniques used to develop new RFPs. This instrument is capable of high-speed automated selection of individual RFP-expressing mammalian cells on the basis of photostability. The photobleaching irradiance levels are similar to those used in many fluorescence imaging experiments (≈2-25 kW/cm^2 [113,114]) and it achieves high sort purity (>99%). For these reasons it is an important tool for efforts to develop a new RFP.

We develop, screen, and sort hypothesis-driven, targeted libraries of RFPs which are expressed in HeLa cells to ensure proper folding and maturation for *in vivo* imaging conditions. Our library sizes are on the order of 10^5 clones, and we are able to screen and sort them with $> 300\%$ coverage. We recognize that longer-range or synergistic mutations are difficult to predict and so error-prone mutagenesis is also incorporated. Furthermore, we present initial attempts at directed evolution techniques.

Additionally, in this chapter we explore the utility of this microfluidic cell-sorter as a RFP-library screener/sorter to select an RFP with greater photostability. Furthermore, library design and construction are considered and analyzed in the context of the advantages and limitations of

this tool as well as in the context of increasing the photostability of proteins. In this way, we take the approach of optimizing library development and instrument running procedures synergistically. Ultimately, this approach results in development of a mutant with $\approx 3\times$ greater photostability than mCherry. However, photostability is increased at the expense of quantum yield. The successes and limitations of this approach, presented herein, inform future attempts at library development and indicate opportunities to further develop this cell-sorter into a more powerful tool.

5.4 Experimental

A detailed description of the experimental setup and performance can be found in Chapter 4. The routine sorting methods and day-to-day operating procedure for sorting libraries is described below.

5.4.1 Sorting Methodologies

The microfluidic and manifold was cleaned and assembled before and after each run as described in Appendix B. The 532 nm excitation/photobleaching laser was set to 1 W resulting in 0.1 W in each of the 9 photobleaching and sort-checking beams. This resulted in a peak irradiance of $\approx 2\times10^4$ W cm^{-2}. The 1064 nm sorting beam was set to 8.3 W (50% current) and the cells were hydrofocused with buffer but suspended in phenol-free media as determined optimal in Chapter 4. The last four of the eight photobleaching beams were deemed unnecessary for optimal photostability-resolution in the libraries evaluated here and were therefore blocked prior to entering the microscope. Each of the remaining five 532 nm beams, the infrared (IR) sorting-beam, and the microfluidic channels were aligned to a pre-determined position specified by a pixel coordinate to maintain consistent timing parameters (Detailed in Chapter 4). As described in Chapter 4, extended interaction between the IR beam and the microfluidic setup and solutions can lead to boiling or burning in the channels. To avoid this, the IR beam was turned on and aligned at only 5% diode current, which is just above the lasing threshold.

The pressures on the reservoir of each channel were approximated prior to cell injection but

optimized upon addition of the cells to achieve a target cell velocity of approximately 6 mm/s which resulted in pressures of 0.5 ± 0.1 psi and 0.8 ± 0.1 psi on the respective lower and upper hydrofocusing channels (B, Figure 4.2) and 0.5 ± 0.1 psi on the center cell channel. The target velocities and hydrodynamic widths were monitored on the velocity histogram of the data acquisition program described in Chapter 4 to maintain day-to-day consistent flow parameters. The desired 20 μm hydrodynamic focus resulted in a 16% standard deviation in the velocity. The two hydrofocusing channel pressures were selected such that the hydrofocused channel was directed into the unsorted-outlet channel but was traveling close to the junction of the two outlets (Figure 4.4).

The PMT voltage was set to -700 V before the addition of cells but was increased (± 100 V) to achieve a median peak intensity of 1 V. This signal level was monitored on the Times and Amplitudes of First Peaks graph (Figure 4.5). The PMT voltage along with the Maximum Time Between Peaks, Minimum Time Between Peaks, and Width of Peaks (Figure 4.5) parameters were optimized to achieve a 50% (0.5) or greater value of Peaks Put Together. This observation indicated that the maximum number of cells was being analyzed because the fluorescence signal from each was being detected at each beam with minimum cell-overlap. This value typically increased 5-10% when the fifth sort-checking beam was blocked (see below).

After the aforementioned parameters were optimized, ≈100 cells were detected and the sorting threshold of the fourth photobleaching beam was selected based upon this representative sample (discussed in further detail below). At this point, the IR sort beam was set to 50% current to begin sorting cells. The sort-checking beam was on and detected by the program at the beginning of each sort. To turn the detection of the check beam on or off the Check Delay Factor (Figure 4.5) is set to the median Actual value or 0 respectively. Once it was verified that ≈70% of the sorted cells were detected by the check-beam (Figure 4.4), the check-beam was blocked (before entering the microscope) and the detection of the beam was turned off. This was done to allow the program to run at maximum speed (since upon detecting the photobleaching beams, it did not have to wait for the check-beam) and therefore minimize the number of overlapping cells. At this point, the outlet reservoirs were emptied via pipette and the sorted-outlet was preloaded with 750

μL DMEM supplemented with 30% FBS and 1% penicillin- streptomycin, cell media (BSA-free, phenol-containing). The sorting program was then restarted to achieve accurate statistics.

5.4.2 Library Construction

The original DNA templates for the parent proteins were amplified with gene- specific primers and cloned into pDonr221 using the Gateway recombination system (Life Technologies). In each case, a single clone was isolated and submitted to commercial DNA sequencing prior to mutagenesis. To introduce mutations in a site-specific manner, primers were designed with codon wildcards at the appropriate positions. Fragments of the gene were amplified, gel-purified, and subsequently reassembled using site-overlap extension.

After reassembly of the gene, an LR reaction with the modified pCLNCX vector was carried out for ≈18 hours at 25° C, followed by proteinase-K treatment at 37° C for ≈15 minutes, and subsequent ethanol precipitation and electroporation of *E. coli* (ElectroMax DH10B, Life Technologies). The library was allowed to grow overnight supplemented with ampicillin. After ≈15 hours of growth, 1 mL of the overnight culture was inoculated for further growth and plasmid DNA isolation (Midi-Prep Kit, Qiagen).

For generation of virus, HEK-293 FT cells were cotransfected with pCL-Ampho, pVSV-G, and the library using reduced serum media (Opti-MEM, Life Technologies) and standard transfection reagents (TransIT- LT1, Mirus Bio LLC). The virus containing supernatant was titrated onto HeLa cells and the cells were prepared for enrichment of the red-fluorescent clones using a Dako Cytomation Mo-Flo cytometer. In each case, the multiplicity of infection was kept below 10% to decrease the likelihood of multiple viral integrations per cell.

5.4.3 Cell Maintenance and Recovery

Prior to sorting, HeLa cells were cultured in Dulbeccos modified essential medium (DMEM) supplemented with 10% FBS and 1% penicillin-streptomycin, as previously described (Chapter 2). For microfluidics-based sorting, the library containing HeLa suspension cells were placed into a solu-

tion of phenol-free MEM-Alpha (Gibco) with the addition of 10% FBS, 1% penicillin-streptomycin, and 14% Opti-Prep. After the sorts, the cells were placed into a 96-well plate for maintenance at 37° C and 5% CO2. After several weeks of expansion, a population of the cells were frozen down in the presence of 10% DMSO, and the remainder of the cells were subjected to additional rounds of selection.

After several rounds of sorting, mRNA was isolated from ≈300,000 HeLa S cells (RNeasy Micro Kit, Qiagen). In each case, enough individual clones (≈ 20 were isolated, and submitted for commercial sequencing, to identify whether the population had converged.

5.5 Results and Discussion

5.5.1 Screened Libraries

The following libraries were screened but, due to their narrow photostability (as a measure of fluorescence intensity from beam 4 divided by that of beam 1) distribution, they were not sorted.

5.5.1.1 Error-Prone TagRFP-T

From studies performed in Chapter 2, TagRFP-T R67K N143S was known to be spectrally similar to mCherry but >2-fold brighter. It was therefore chosen as the starting template for a library using error-prone mutagenesis with >9 mutations per kilobase pair (kb) which resulted in 1,000,000 members of which 7% (70,000) were fluorescent (by FACS). Twenty clones were sequenced, 55% of which were found to be the parent sequence. Of the remaining non-parent population, 47% of the mutations were located on the outside of the barrel or in the disordered loops between the strands of the barrel and 41% of the mutations were already observed in the TagRFP to mKate evolutionary trajectory. Therefore, 12% of the mutations were novel and could potentially affect the photophysics of the protein. Due to the low diversity of this library, no attempts were made to sort it. However, it was screened and the coefficient of variation (CV) of the photostability distribution for this library was 100% (Figure 5.1) which is similar to a distribution of a monoclonal population

(mCherry, Figure 5.2).

5.5.1.2 Morello Library

This library (Morello-0) was created using mCherry as the parent and randomizing K70, S146, V177, and I197 to all 20 amino acid options coupled with error-prone PCR (>6 mutations/kb). These are the four mutations used to evolve TagRFP into mKate, whose emission at wavelengths longer than 650 nm is ≈200% brighter than that of TagRFP [18]. It was hypothesized that these same mutations may play analogous roles in improving mCherry. These mutations are depicted in Figure 5.3. This library had a photostability CV of 72% and had an average photostability (0.994) slightly higher than that of mCherry (0.959) which had a CV of 100% (Figure 5.2).

5.5.2 Kriek Library

Recent molecular dynamics (MD) simulations performed by Chapagain et al. [47, 48] on mCherry have indicated that the gap between β-strands 7 and 10 is larger relative to citrine (Figure 5.5), which was chosen for comparison because it is a naturally occurring monomer and a GFP homologue of mCherry. Side-by-side comparison of MD simulations on both these proteins show this region to be more dynamic in mCherry as well. It has long been hypothesized that this gap allows increased oxygen permeability and therefore, increased photobleaching. This study identifies three point mutations (W143K, Q163R, and R164E) which, in MD simulations, drastically decrease the gap between strands 7 and 10 and minimize the dynamic motions of strand 7. The gap was decreased and stabilized because key residues were exchanged for carefully chosen charged residues which attracted oppositely charged residues on the parallel strands . During a 10 ns MD simulation, this mCherry mutant remained stably folded, however, incorporating these exact mutations into mCherry resulted in a non-fluorescent protein. It is possible that the monomeric protein was unable to properly fold due to the addition of the positive inward facing residue, Lys143, as all other Lys residues on the barrel are outward facing due to the hydrophobic protein interior. Furthermore, it is possible that the protein folded properly, but the chromophore was unable to mature due to

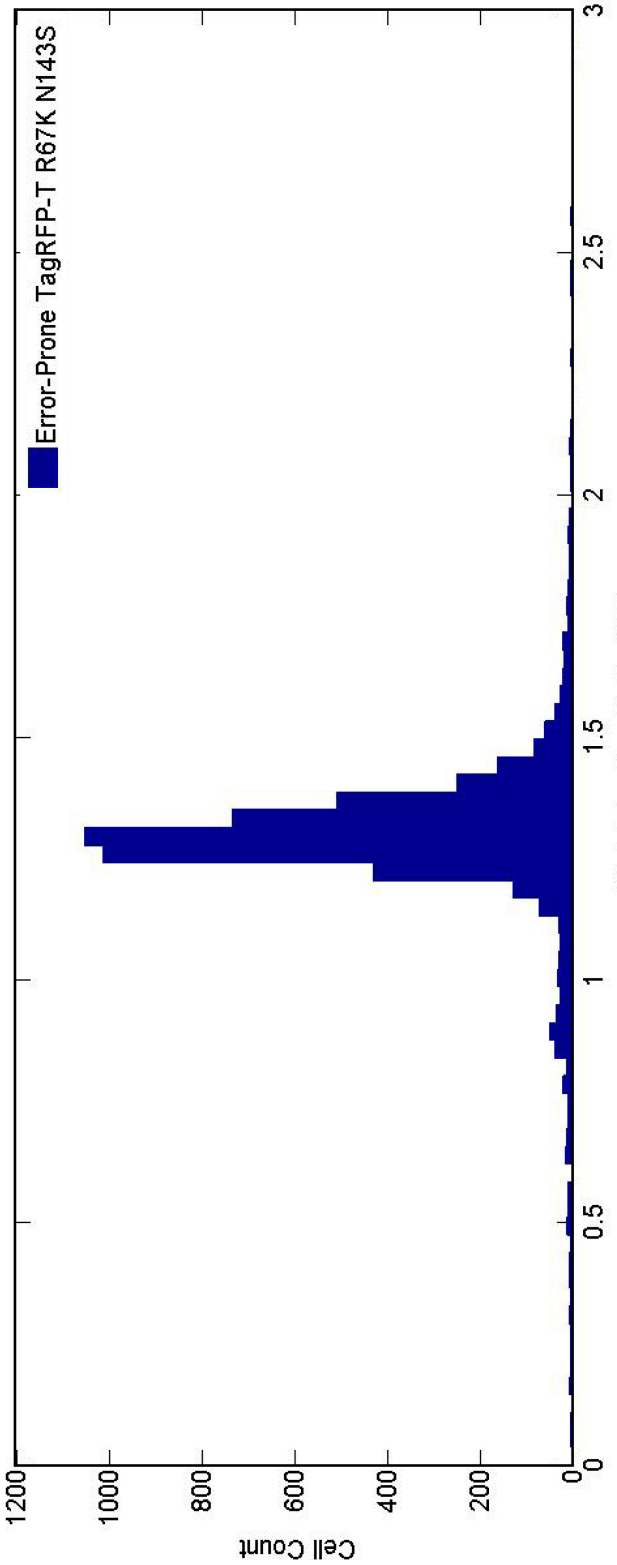

Figure 5.1: Histogram of photostability for error-prone TagRFP-T library.

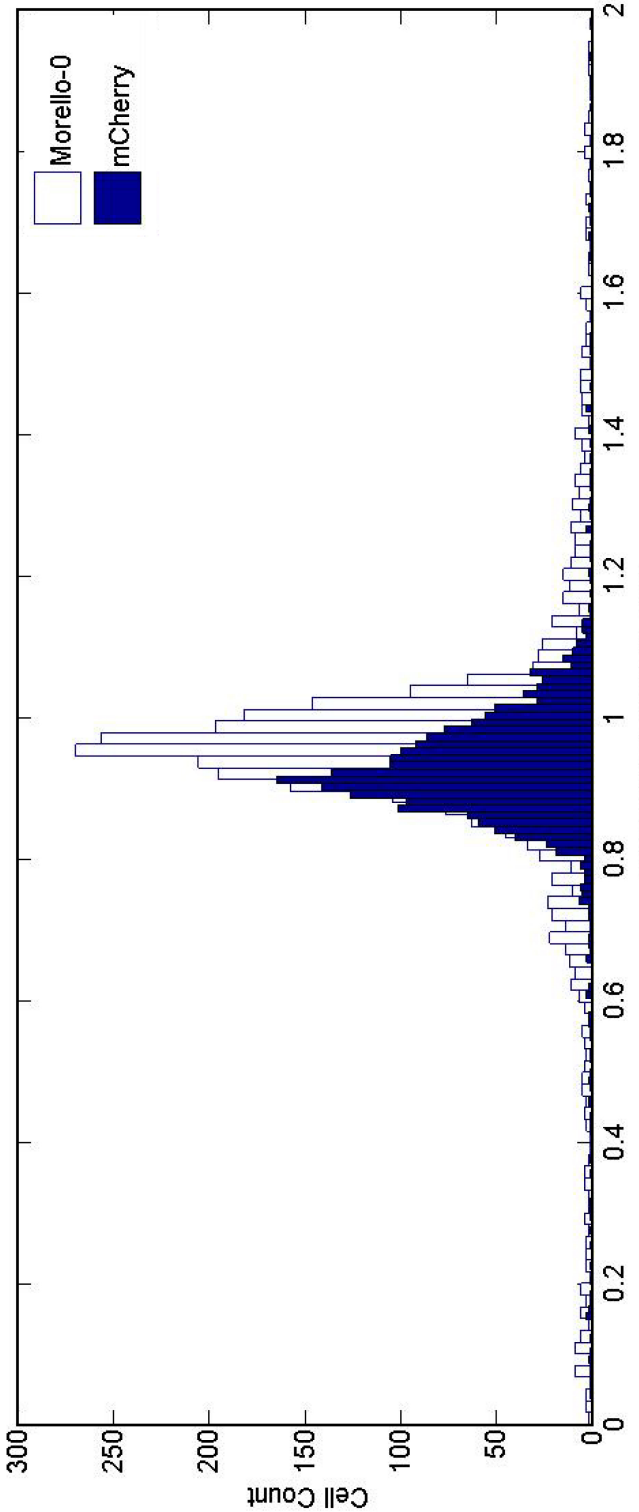

Figure 5.2: Morello is more photostable than mCherry (mean = 0.994, vs. 0.959) but is not diverse in photostability (CV = 72%, vs. 100%).

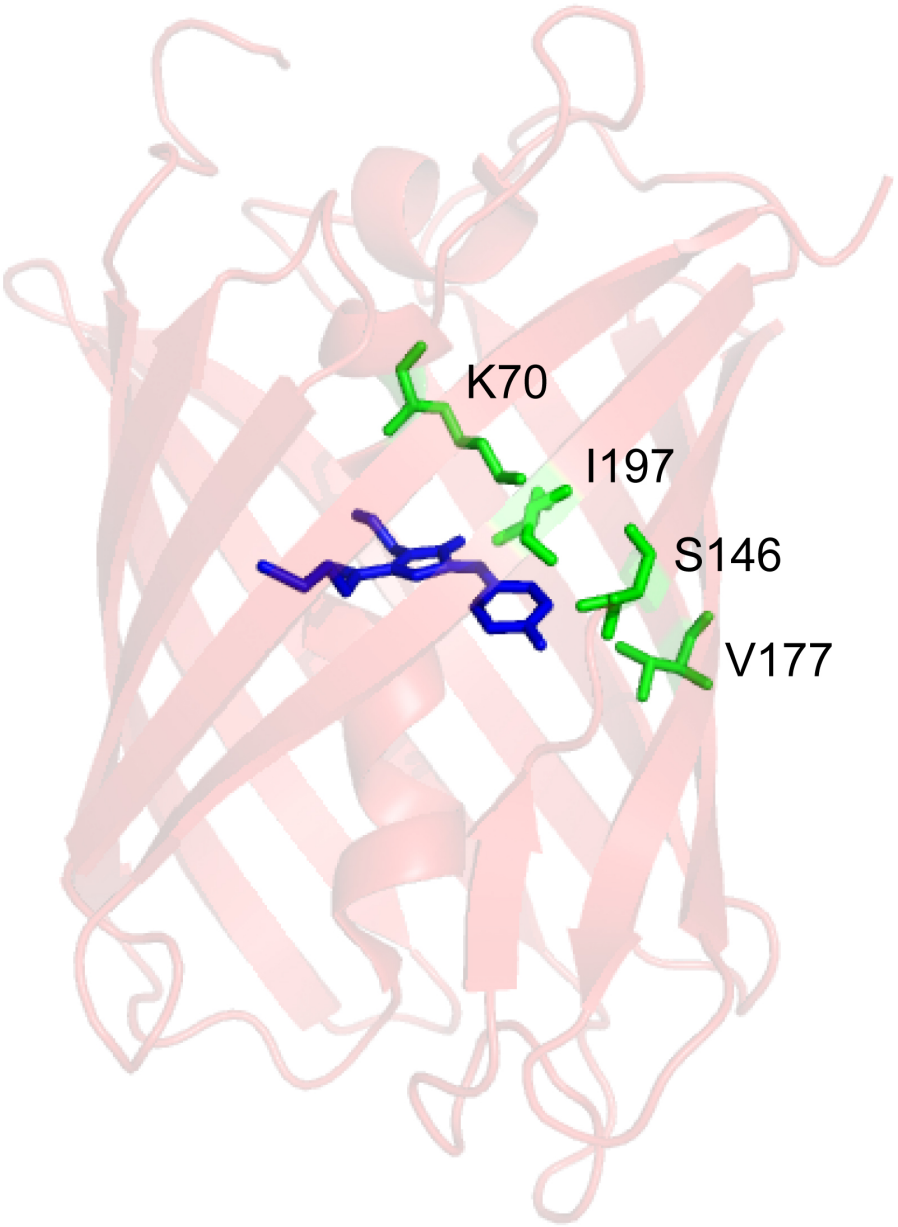

Figure 5.3: Morello library residues. The barrel is depicted in red, chromophore in blue, and mutated residues in green.

decreased oxygen permeability, thereby limiting the necessary oxidation reaction.

A thorough literature review revealed positions that had been frequently cited in the literature as having contributed to the development of an improved FP. Positions which had converged on a single amino acid were then eliminated from consideration. Hypothetically, the remaining indentified-positions had high mutational potential. Interestingly, two of the mutations identified in the MD simulations (W143 and Q163) fell into this category but R164 was revealed to be a critical mutation for monomerization [24]. The remaining positions identified in this search were V16, Q66, I161, I197, and A217 (Figures 5.4 and 5.6). Positions I197 and A217 were omitted due to difficulties in the site-overlap extension reaction.

The Kriek library (K0) was constructed using mCherry as the parent due to it being the most photostable RFP under laser excitation as compared to other mFruits (Chapter 2 [49]). V16 was randomized to E, D, A, K, N, or T. Q66 was randomized to K, E, Q, M, V, L, N, D, H, Y, I, or F. I161 was randomized to L, M, V, I, or F. W143 and K163 were randomized to all twenty amino acid options. The final library size was 144,000 members. Non-fluorescent members were removed by an initial brightness screen *via* FACS, and <10% were found to be fluorescent.

5.5.2.1 Initial Rounds of Sorting

The Kriek library was sorted three times (K1, K2, and K3). At each sort, the number of cells analyzed was greater than three times the estimated number of unique clones. For example, <10% of unique mutants remained after the FACS sort for fluorescent mutants. Therefore $> 3 \times (10\% \text{ of } 144{,}000) = 43{,}200$ cells were analyzed during the first round of sorting. For the first two rounds of sorting, cells in the top 25% of the photostability distribution were selected and recovered. As described earlier, the threshold for the selection was set after initially screening 100 cells. After each round of sorting, a shift towards greater photostability was observed (Figure 5.7). However, for the third sort, only the 10% most photostable cells were selected. Due to the decreased selected population, contamination from unselected cells accidently traveling into the sorted channel overwhelmed the selected population, and a population-shift towards decreased photostability was

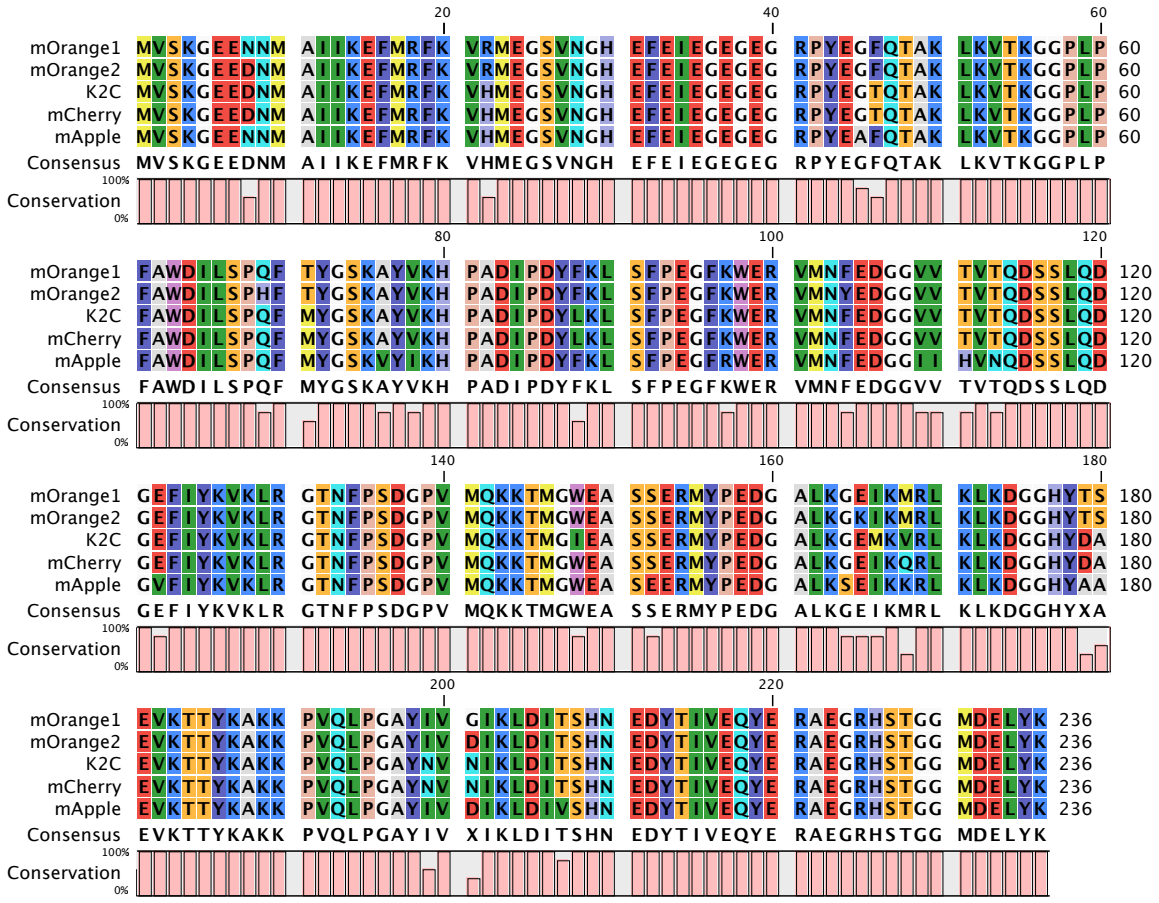

Figure 5.4: Sequence alignment for selected red mFruits showing conservation of each residue. Each residue is color coded for clarity.

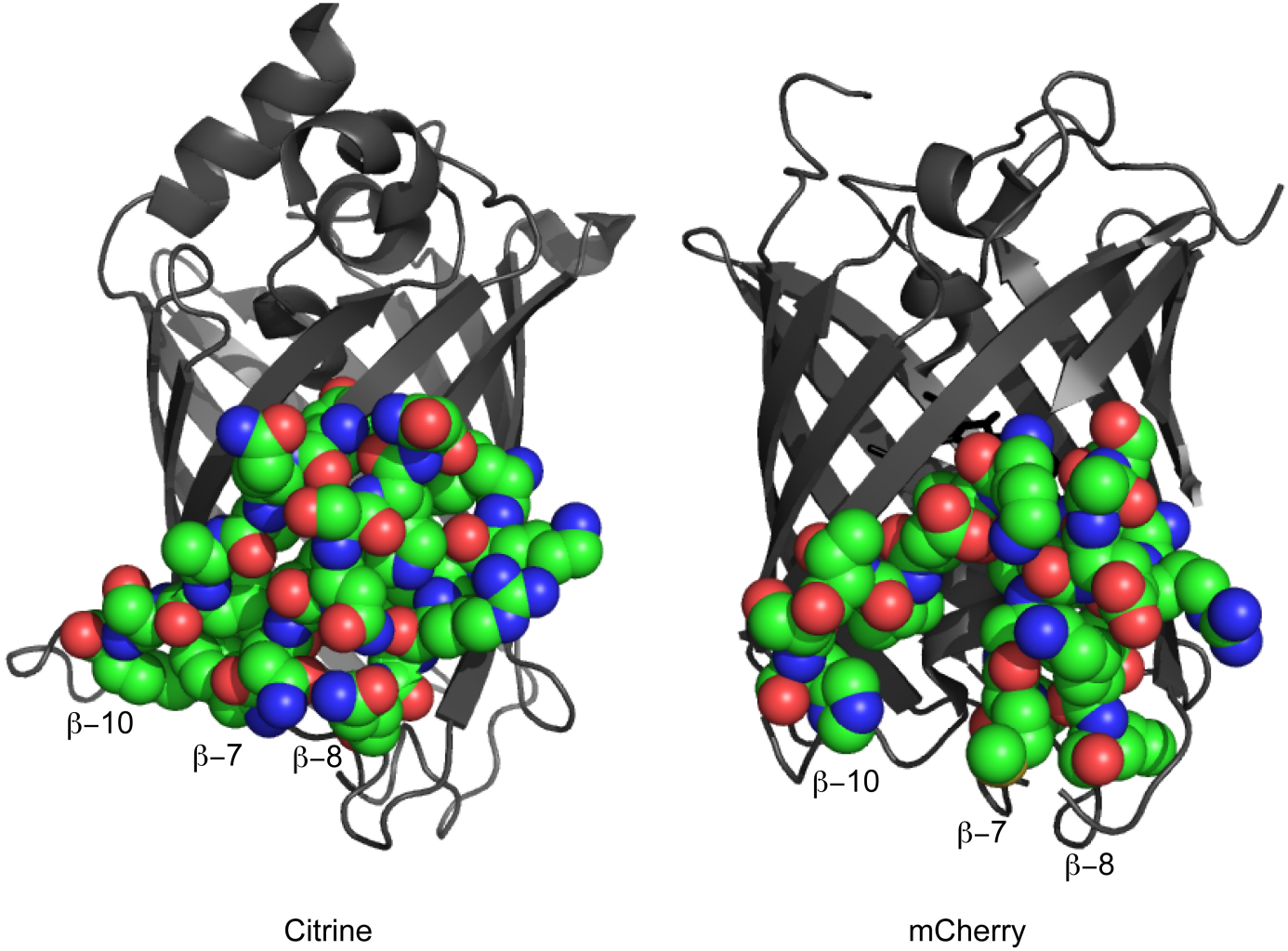

Figure 5.5: Gap between β-strands 7 and 10 of mCherry. The gap between strands 7 and 10 of citrine was found to have a relatively constant separation distance of $\approx$ 5 Åwhereas the gap between strands 7 and 10 of mCherry was found to fluctuate between $\approx$ 5-9 Å [48]. This gap is evident in this figure where the amino acids of strands 7, 8, and 10 are depicted as spheres sized accordingly to the atoms they represent (green is carbon, blue is nitrogen, and red is carbon).

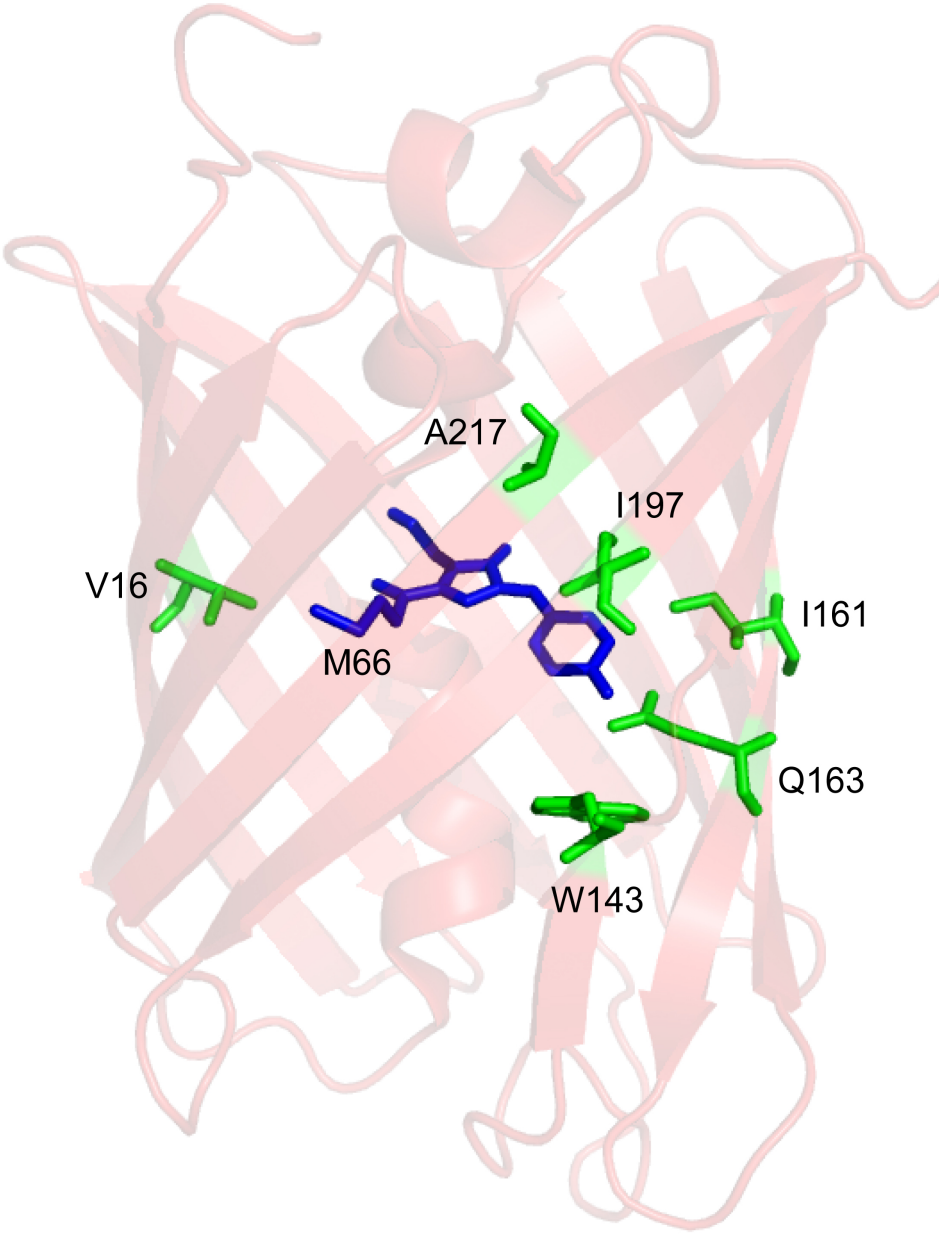

Figure 5.6: Residues on mCherry identified for potential library construction are depicted in green, the barrel in red, and the chromophore in blue.

observed (Figure 5.7). After each round of sorting, the sorted cells were recovered and maintained as described above. Once they had recovered and sufficiently multiplied, an aliquot was frozen and preserved for future reference or use. Due to day-to-day variabilities in the beam intensities (discussed in Chapter 3), data for Figures 5.7 and 5.8 was taken on the same day under identical conditions using these frozen samples to allow direct comparisons.

We observed that each round of sorting and subsequent shift towards increased photostability of the population resulted in a shift towards decreased brightness (as measured by the fluorescence signal from beam 1, Figure 5.8). This decreased brightness is most likely because photostability was increased by decreasing the fluorescence lifetime (discussed in Chapter 1). This hypothesis is supported by fluorescence lifetime data taken on some of the K2 mutants and is discussed later in further detail. In an effort to rescue the fluorescence brightness K2 was resorted with the added selection pressure of selecting mutants that were in the top 30% of brightness as well as in the top 20% of photostability. This sort resulted in fewer than 5% of the cells being selected. This population was named K4 and was used in future attempts at directed evolution detailed later.

5.5.2.2 Successful Mutants and Their Spectroscopic Characteristics

Sequencing was carried out on several mutants from the K2 and K4 populations. mCherry was present in many of the results, however, the novel mutants shared many of the same mutations (detailed in Table 5.1). Purified protein samples were created for many of these mutants and their quantum yields and absorption, excitation and emission spectra were measured and summarized in Table 5.2. The mutant K2C is red shifted relative to mCherry and the other K2 mutants. Examining the K2, K4, and mCherry mutants revealed that K2C, mCherry I161M Q163V, and mCherry W143I I161M were the most red shifted relative to the other mutants and they all contained the I161M point mutation. A literature search revealed that the mutation I161M was found in two screens designed to shift the fluorescence wavelength further into the red region [66, 118].

The mutants' photostabilities were then evaluated off-chip. First, purified protein samples of the mutants were sonicated in octanol to form emulsions and then examined under 561 nm CW laser-

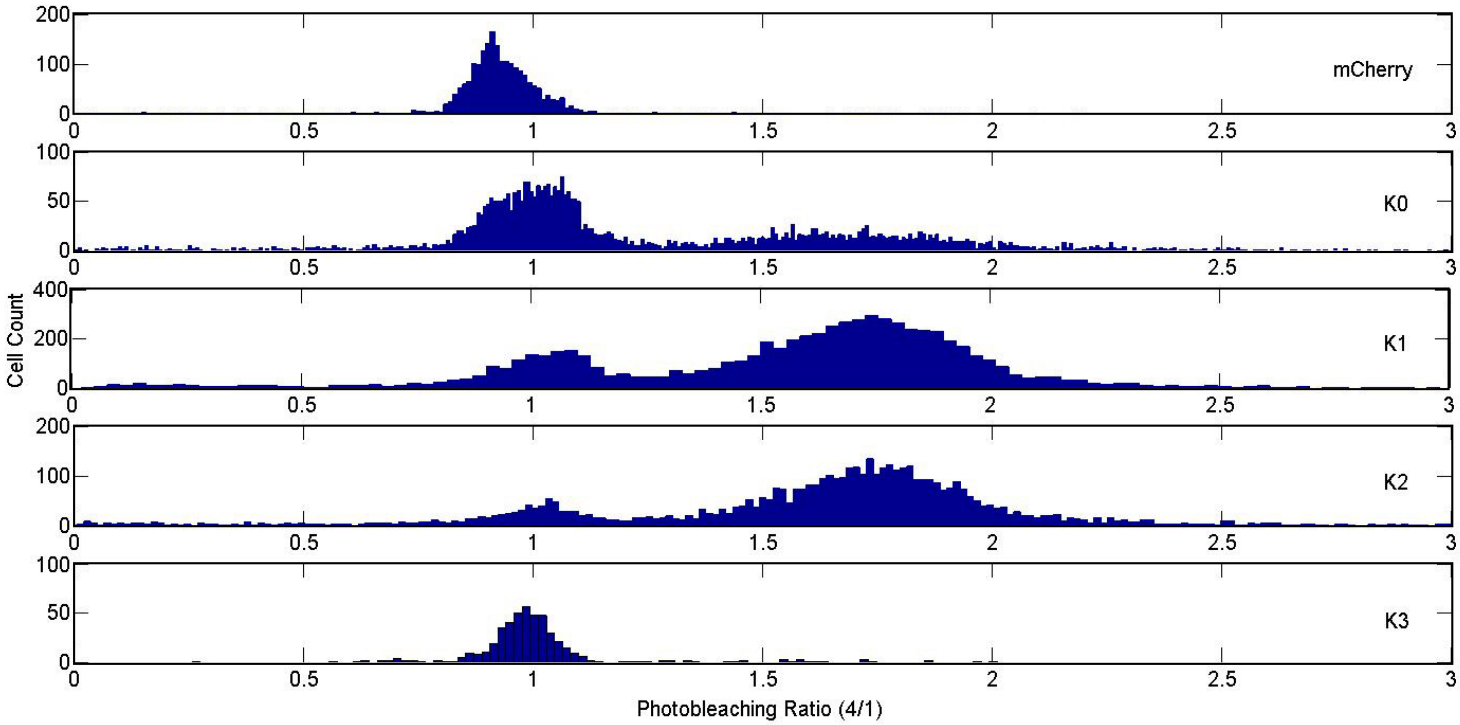

Figure 5.7: All data in this graph was taken on the same day on the cytometer in screening mode. Each cell population was flushed out of the cytometer with phenol-free media between each run for >5 min to eliminate cross-contamination.

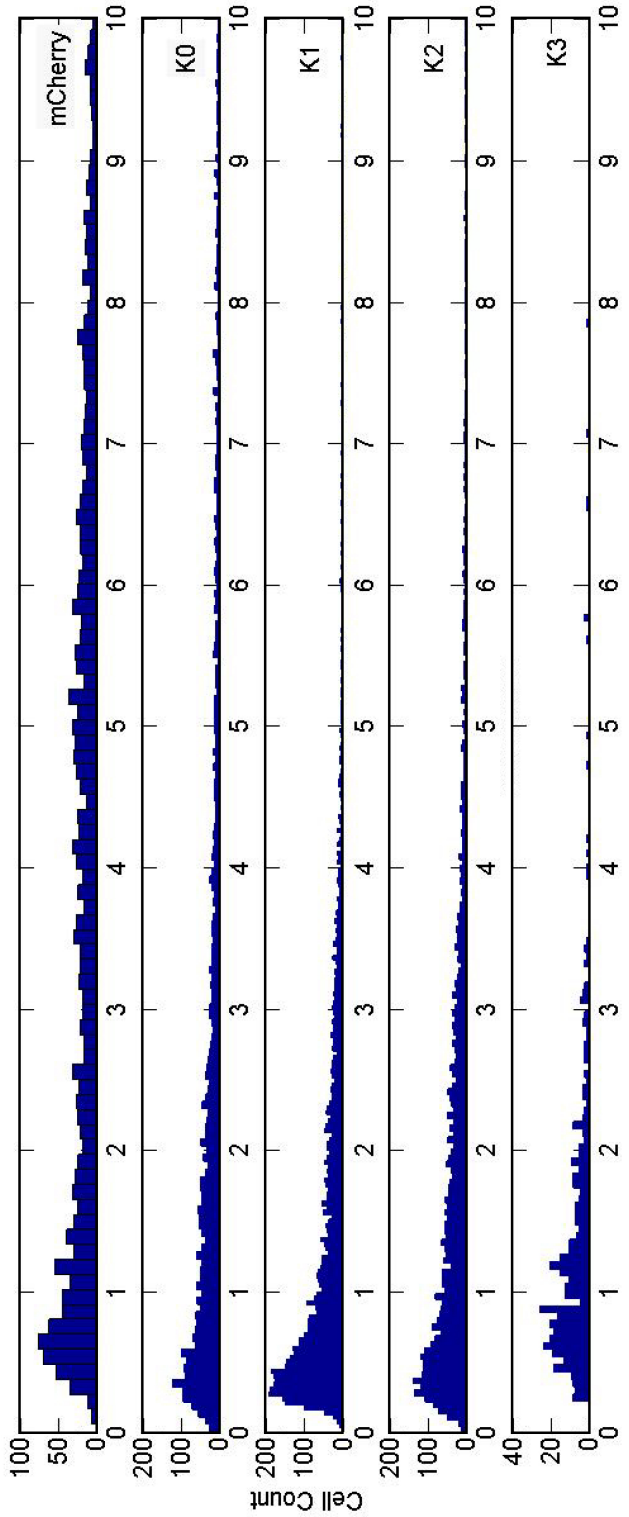

Figure 5.8: After each sort for photostability, the cell population shifted towards decreased brightness.

Table 5.1: Mutations observed for K2 and K4. In mutants with V16A mutations, an unintended mutation, likely arising from primer synthesis, also incorporated H17R.

RFP	V16	M66	W143	I161	Q163
K2A			A	L	I
K2B			C	V	T
K2C			I	M	V
K2D	A	Q	M	V	L
K2E	A	Q	S	V	L
K2F	A	Q	M	V	W
K4A			A	L	I
K4B			S	V	L
K4C			S	V	L
K4D			A	L	I
K4F		Q	A	L	I
K4H			S	V	L
K4I			A	L	I
K4J			S	V	L
K4K					
K4L			A	L	I
K4M			A	L	I
K4P			A		
K4Q			A	L	I
K4S					
K4T			A	L	I

Table 5.2: Spectral properties of novel mutants.

RFP	λ_{abs} (nm)	λ_{ex} (nm)	λ_{em} (nm)	ϕ_{fl}
K2A	588	510	610	0.12
K2B	585	586	607	0.12
K2C	592	593	613	0.08
K2D	588	588	607	N.D.
K2E	583	583	603	N.D.
K2F	587	588	606	N.D.
mCherry	587	591	608	0.23
mCherry W143I	583	583	611	N.D.
mCherry I161M	588	592	617	N.D.
mCherry Q163V	585	586	614	N.D.
mCherry W143I I161M	589	592	618	N.D.
mCherry W143I Q163V	587	588	618	N.D.
mCherry I161M Q163V	588	590	612	N.D.

N.D. = Not Determined

svaning confocal conditions. K2C was the most photostable mutant, with other mutants showing modest improvements over mCherry. Given this result, the other mutants were no longer pursued. K2C was then evaluated relative to mCherry by nuclear localizing both proteins within adherent HeLa cells. Photostabilty was measured under several *in vivo* conditions as photostability is known to be non-linear with excitation intensity [49]. Photobleaching measurements were conducted with 100% and 10% laser powers in a 561 nm CW laser-scanning confocal mode and in a wide field epifluorescence mode (Figure 5.9). For laser illumination, both K2C and mCherry were fit with a biexponential and the weighted lifetime was used for comparison. At 100% laser power, K2C was ≈50% more photostable than mCherry (58 s *vs* 37 s, Figure 5.9, bottom panel). At 10% laser power, K2C was ≈180% more photostable than mCherry (1700 s *vs* 600 s, Figure 5.9, center panel). Under widefield CW conditions, K2C is ≈150% more photostable than mCherry (284 s *vs* 111 s, Figure 5.9, top panel).

K2C, while more photostable than mCherry, had a quantum yield ≈3-fold lower than mCherry (Table 5.2). As discussed in Chapter 1, quantum yield is known to scale linearly with fluorescence lifetime. To ascertain if K2C's fluorescence lifetime decreased, resulting in greater photostability but decreased quantum yield, time-correlated single photon measurements were preformed. K2C's fluorescence lifetime was determined to be ≈2-fold lower than that of mCherry (Figure 5.10, indicating that a decreased fluorescence lifetime most likely contributed to the improved photostability and decreased quantum yield of K2C.

5.5.2.3 Additional Mutagenesis and Sorting on Kriek-2 and Kriek-4 Successful Mutants

The DNA of the successful mutants from K2 and K4 (Detailed in 5.5.2.2) were combined equally and subjected to two different-further rounds of mutagenesis to create two new libraries: Kriek2.1 (K2.1) and Kriek2.2 (K2.2). K2.1 consisted of the K2 mutants randomized at positions 59, 62, and 199 to all 20 amino acid options (resulting in 900,000 mutants, 12% of which were fluorescent by FACS, Figure 5.11). These positions were chosen due to their proximity to the

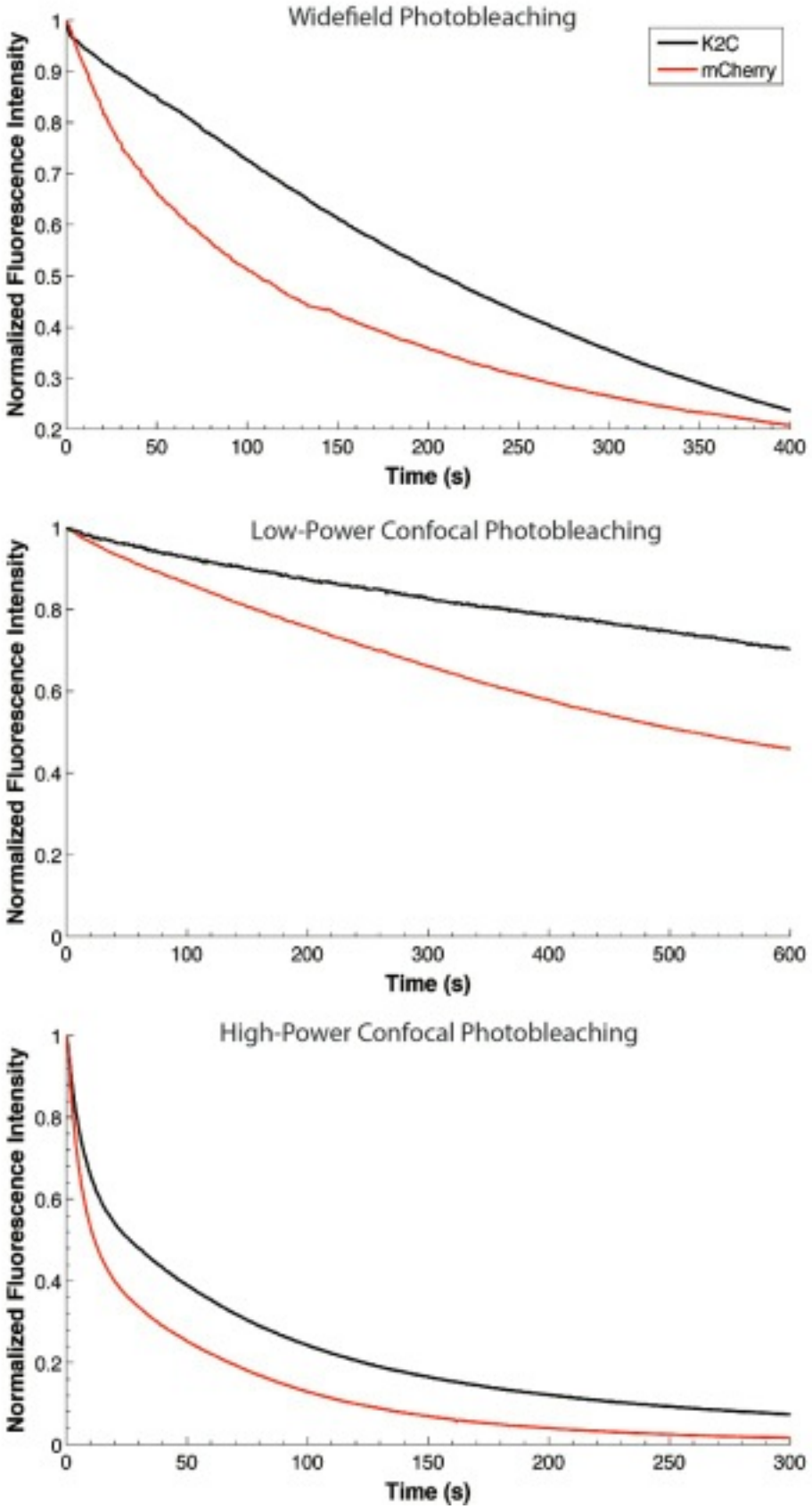

Figure 5.9: Photobleaching curves for K2C and mCherry. Under wide field photobleaching conditions, K2C was 150% more photostable than mCherry (Top Panel). For high-power confocal photobleaching (100% laser power), K2C was 50% more photostable than mCherry (Middle Panel). For low-power confocal photobleaching (100% laser power), K2C was 180% more photostable than mCherry (Bottom Panel).

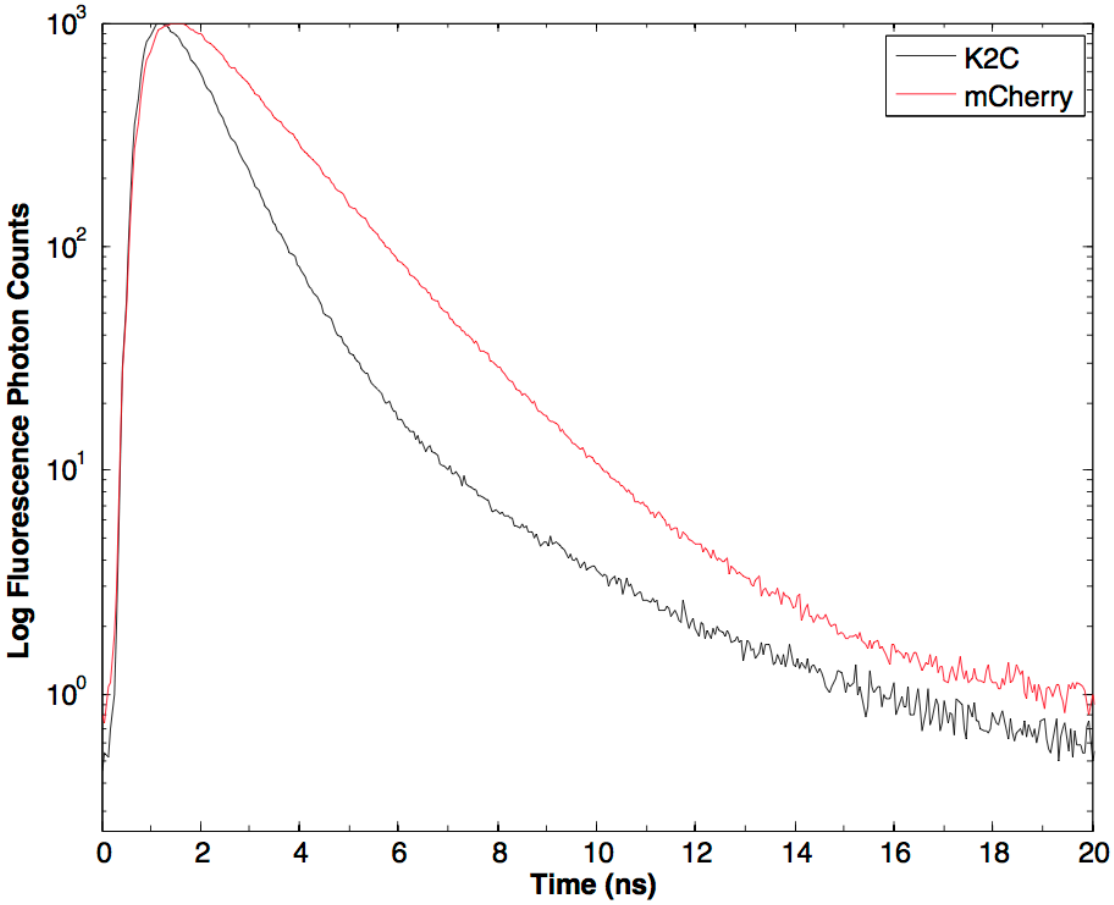

Figure 5.10: Fluorescence lifetime of K2C (≈1.0 ns) and mCherry (≈1.9 ns).

mutations present in K2 and K4 as they could potentially act synergistically with these mutations.

K2.2 consisted of the K2 and K4 mutants randomized at positions 70, 197, and 215 to all 20 amino acid options. These positions were selected based on their proximity to Glu215, an amino-acid known to undergo decarboxylation and thought to be involved in irreversible photobleaching (Figure 5.12) [71, 119–124]. K70 is located above the chromophore and reported as important to the photstability of the TagRFP variants [49]. I197 is the position analogous to the Π-stacking T203Y mutation in Citrine and Venus [23, 125].

Both K2.1 and K2.2 showed a decrease in average photostability and similar photostability distributions (CV = 160% and 95% respectively) relative to the parent (K2, CV = 140%) and were therefore not sorted (Figure 5.13 and 5.14).

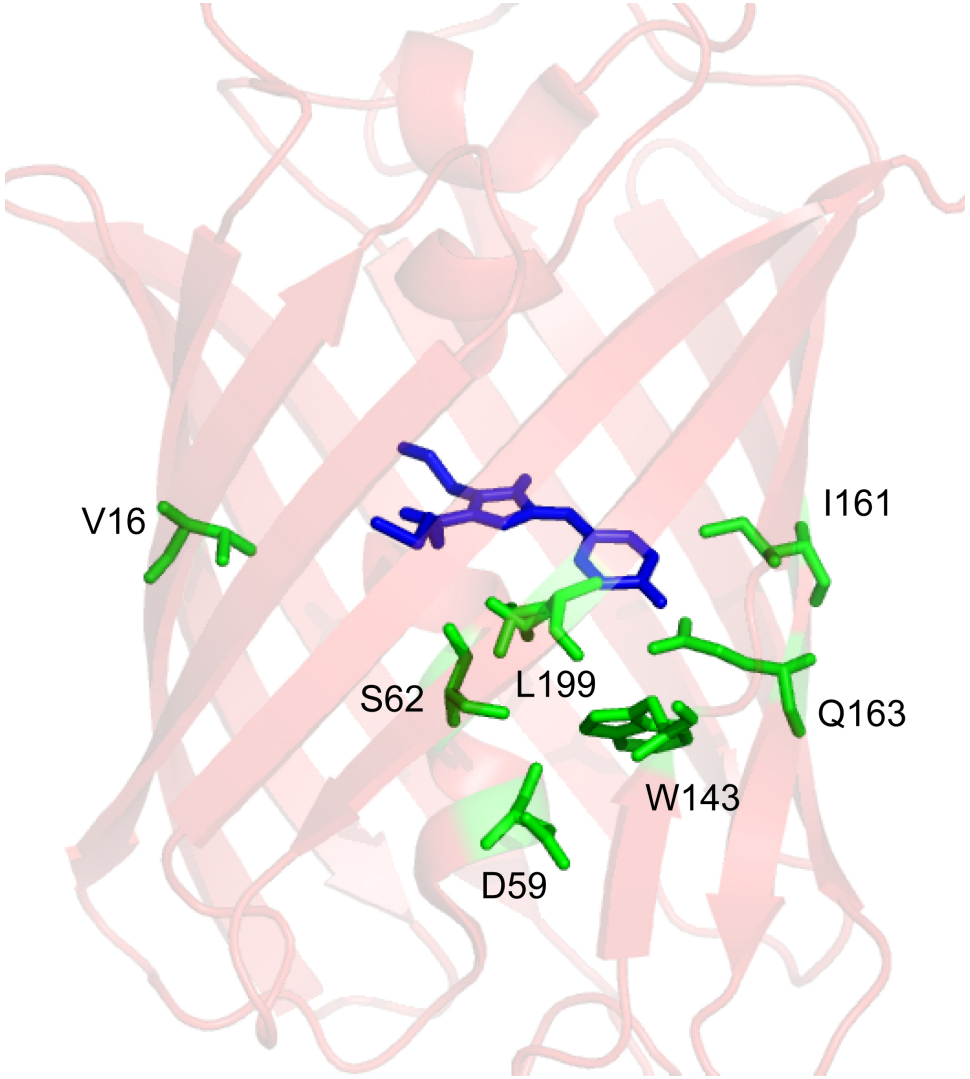

Figure 5.11: Residues randomized for K2.1 library are depicted in green, the barrel in red, and the chromophore in blue.

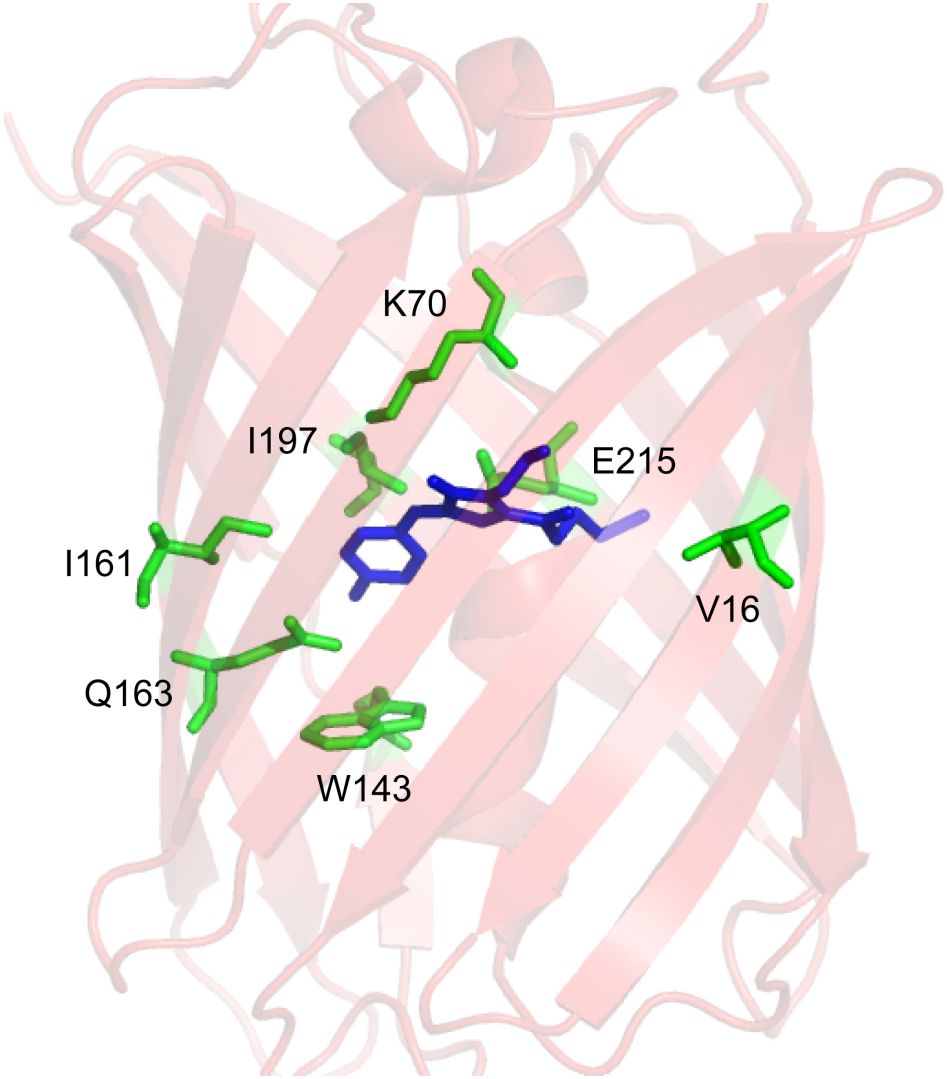

Figure 5.12: Residues randomized for K2.2 library are depicted in green, the barrel in red, and the chromophore in blue.

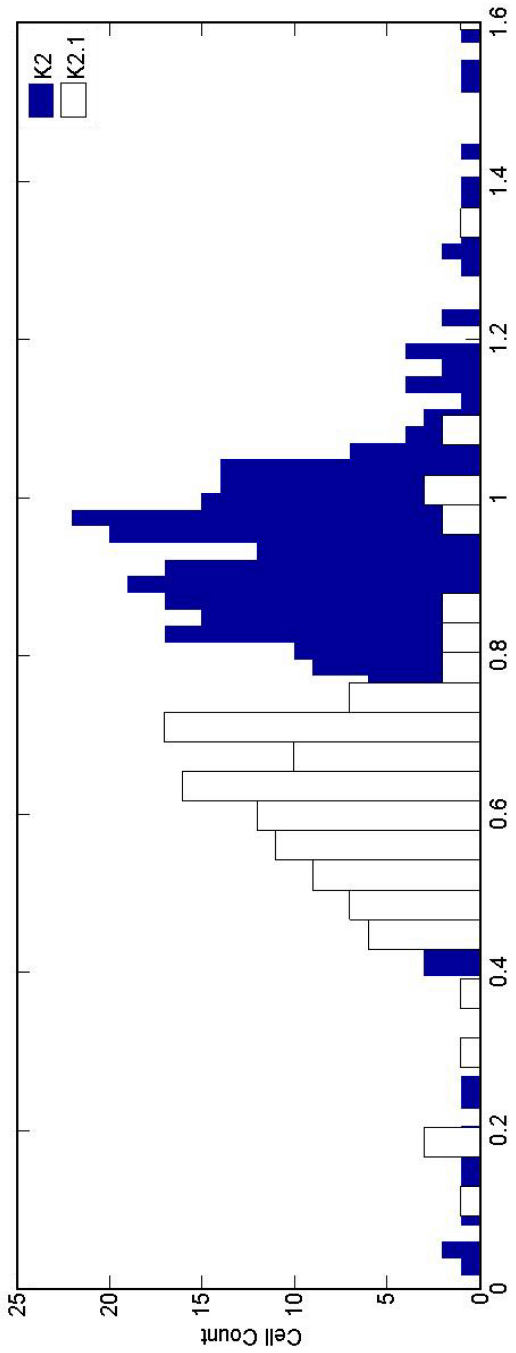

Figure 5.13: Histogram of photostability of K2.1 relative to K2.

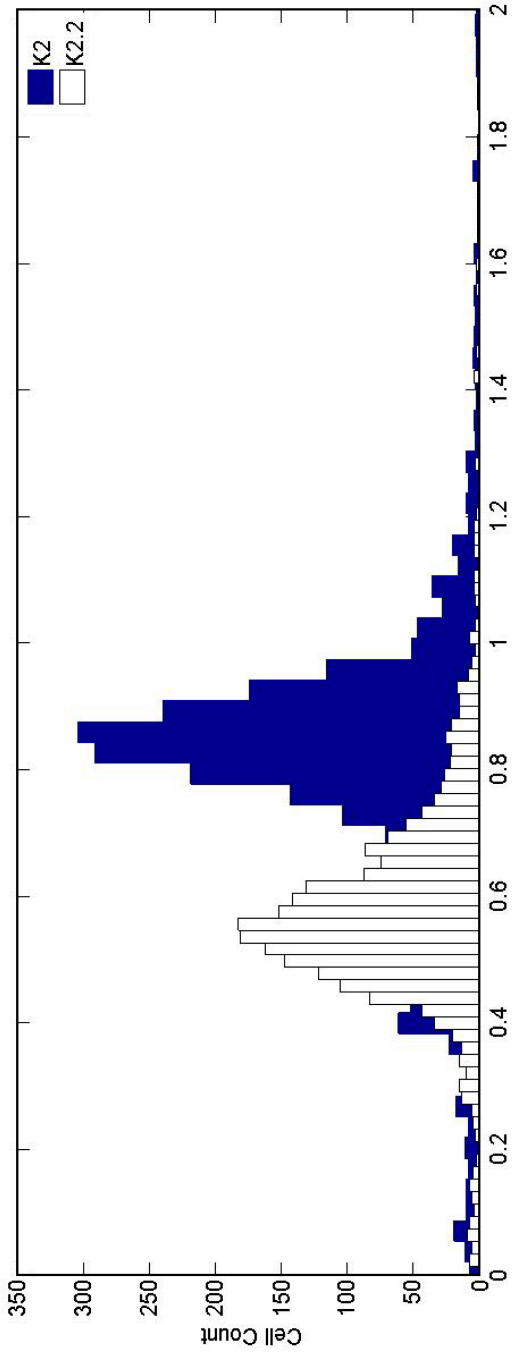

Figure 5.14: Histogram of photostability of K2.2 relative to K2.

5.6 Conclusions and Future Directions

This chapter details our initial attempts at library construction, screening, and sorting. The results from the libraries screened thus far indicate that greater diversity in the initial library is needed. It also indicates that residue choice and not necessarily library size plays a critical role in achieving diversity in photostability. Furthermore, since many libraries are not diverse enough to merit sorting, it would be useful to screen libraries for photostability before they are expressed in HeLa cells, which is the rate-limiting step. Preliminary results (data not shown) show that screening *E. coli* in the microfluidic platform gives excellent signal-to-noise and hydrofocusing characteristics but that fitting the fluorescent peaks from the *E. coli* is difficult due to cell division. *E. coli* divide such that the two cells (resulting from the division of one) remain fused along the long axis of the cell. When they are in this configuration, they give rise to doublet peaks which pose extreme difficulties for data acquisition and processing. Therefore, additional efforts need to be made to eliminate these fused cells and thus accelerate library development. This would also aid in identifying key residues which drastically affect the photostability. It is much less labor intensive to screen a library as opposed to sorting it, and so it would be more efficient to drastically mutate areas of the protein with saturated mutagenesis, screen the library in bacteria, and determine if that region of the protein significantly altered the photostability as determined by the photostability distribution. Regions of sequence that do significantly alter the photostability would merit more attention during library development. In this way, our efforts would benefit from this additional information and be guided by failures and successes, instead of existing, published successes.

Sorting of the Kriek library demonstrated that a library can converge with only two rounds of sorting. However, the sorted cells are far less healthy than unsorted cells (due to interaction with the sorting laser). This leaves the sorted population vulnerable to contamination by unsorted cells. These factors indicate that an optimal sorting protocol would consist of selecting $\approx$20% of the most photostable cells each sort and sorting fewer times.

Observing the diversity of all of the screened and sorted libraries, it is clear that additional

mutagenesis should be applied between sorts (*i.e.* directed evolution) to achieve drastically improved photostabilities. Currently, the microfluidic sorter is limited to library sizes of 100,000s (assuming 10% fluorescence by FACS) due to the slower sort-rate relative to FACS (Chapter 4). Creating libraries of this size and finding a drastically improved mutant has a very low probability as evidenced by the extensive mutagenic efforts detailed in the literature and our results in this chapter. However, creating an extremely large library and choosing the most photostable mutants would be prohibitively inefficient. Therefore, directed-evolution is the best solution.

Our first attempts at directed-evolution are outlined in this chapter but additional efforts are needed to guide this course of action. However, these efforts would be better informed by successful mutants that show simultaneous improvements in photostability and brightness. Unfortunately, as detailed above, shifts towards increased photostability resulted in decreased brightness. This result is not surprising. As discussed in Chapter 1, selecting on the basis of one criterion often optimizes that criterion at the expense of others. To counter this, both criteria need to be optimized simultaneously. In this chapter, an attempt to this end was made by sorting on the basis of photostability and brightness of beam 1. However, the brightness of beam 1 is an extensive measurement of the concatenation of many parameters including cell cycle, RFP quantum yield, cell size, and RFP maturation. These considerations indicate that the selections should employ an intensive metric of RFP brightness (*i.e.* quantum yield), which will be discussed in Chapter 6.

Chapter 6

Preliminary Frequency Domain Lifetime Measurements in Flow

6.1 Abstract

Development of the next generation of fluorescent probes hinges on multiparametric sorting methodologies. Our ability to exploit the power of sorting a single population on the basis of multiple photophysical parameters is currently limited by sorting technology which, to date, has not been extensively developed to meet this need. Here we present the development of a microfluidic-based cell sorter which can screen cells on the basis of fluorescence lifetime (a proxy for quantum yield). This instrumentation, coupled with the sorting and photostability-assesing capabilities presented in the preceding chapters provides the foundation of a multiparametric sorter. This new instrument is a unique tool for high-throughput, rapid analysis and selection of individual mammalian cells which, with further development, can be used to generate advanced RFPs. Furthermore, through analysis of successful RFP mutants, key and, possibly, synergistic mutations can be identified to help elucidate the complex relationship between the structure and photophysics of these FPs.

6.2 Publication Status and Author Contributions

The work presented here is unpublished.

K.M.D., J.L.L., A.E.P., and R.J. designed research. J.L.L. built intensity modulation setup. K.M.D. and J.L.L. performed research. J.L.L. performed data analysis.

6.3 Introduction

Photostability is an important parameter to improve in FPs as it limits the number of photons that can be collected from a single protein and it limits imaging acquisition time [51,114]. However, it is known that mutations which improve one photophysical property often diminishes another [15, 55]. In the previous chapter we demonstrated a microfluidic-cell sorter capable of sorting libraries of RFPs on the basis of photostability. A new mutant with increased photostability was discovered, but the photostability was optimized at the expense of the quantum yield. These experimental results have illustrated the need for multiparametric sorts as recently discussed in [53]. To address this need, we present progress towards a multiparametric cell-sorter capable of sorting cells on the basis of photostability and quantum yield.

Currently, the predominant methods for improving the quantum yield of FPs rely on fluorescence activated cell sorting (FACS) to sort libraries on the basis of the fluorescence intensity elicited from a continuous wave (CW) laser beam [15, 23, 24, 126, 127]. Unfortunately, this measurement is the concatenation of many parameters including quantum yield, extinction coefficient, excitation/detection wavelengths, protein maturation, DSC, cell size and genome integration site. For this reason, it is a qualitative measurement of quantum yield and therefore could lead to inaccurately including or excluding library members during a sort. For library enrichments which require multiple rounds of sorting, an intensive measurement of quantum yield is desired to decrease variability throughout these many selection rounds.

The fluorescence lifetime (τ) is linearly related to the the quantum yield (ϕ_{fl}) by:

$$\phi_{fl} = \tau \times k_{rad} \tag{6.1}$$

Where k_{rad} is the emissive rate of the fluorophore. Therefore, measurements of the fluorescence lifetime provide an intensive measurement of quantum yield. Recently, fluorescence lifetime was used as a metric to manually select colonies for increased quantum yield [54] and resulted in a 50% increase in quantum yield.

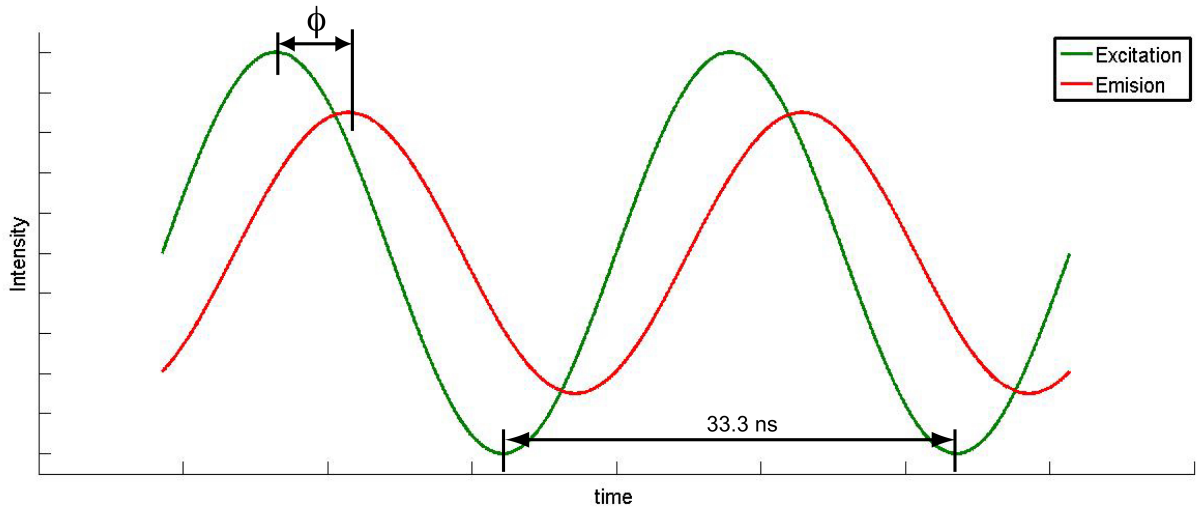

Figure 6.1: Emission is delayed in time relative to the 30 MHz modulated excitation by the phase angle (ϕ) which is linearly related to the fluorescence lifetime τ.

Measuring fluorescence lifetime in flow requires accurately determining the lifetime during the 1-2 ms the cell spends in the interrogation beam, indicating that frequency domain measurements are best suited for this task. In frequency domain lifetime measurements, the excitation light is rapidly intensity-modulated at a rate similar to the fluorescence lifetime (25-30 MHz in the case of FPs). The emission is delayed relative to the excitation due to the time lag between absorption and emission (Figure 6.1). The delay is measured as a phase shift (ϕ) between the excitation and emission. The lifetime is linearly related to the phase shift by the excitation modulation frequency in radians/s ($\omega = 2\pi\times$ Hz) [51].

$$\tan(\phi) = \omega\tau \tag{6.2}$$

However, extra delays between the excitation and emission light can result from delays in the electronics or optics and so careful calibration (such as that detailed in [128]) is necessary.

There is precedence for fluorescence lifetime detection on a high-throughput instrument which takes measurements on cells or beads in flow [86,87,129] but implementing this parameter in tandem with our photobleaching metric has necessitated careful electronics and optics design. Additionally,

these studies have not comprehensively measured lifetimes of FPs or FPs with multi-exponential fluorescence lifetimes or long-lived dark states. Therefore, preliminary data is presented in this chapter, but further experiments and data analysis are required before multiparametric sorts are implemented.

6.4 Experimental Results and Discussion

Here we present preliminary results for fluorescence lifetime detection and multi parametric screening. Further data analysis and experimentation is required before a comprehensive analyses can be made. Detailed day-to-day running procedures can be found in Chapter 5.

6.4.1 Experimental Setup

The experimental setup has been described in detail in Chapter 4. However, for fluorescence lifetime detection, an extra 1 W/cm^2 532 nm beam was added prior to photobleaching beams and was modulated at 29.5 MHz by an electro-optic modulator (EOM). The experimental setup is depicted in Figure 6.2.

The resulting modulated fluorescence from the lifetime beam was collected on the same PMT as the photobleaching signals. A schematic of the electronics is provided in Figure 6.3. The current from the PMT was sent to a custom-built radio frequency amplifier which amplified the signal and separated the low frequency components of the signal ($<$ 1 MHz) and sent them to a custom-built operational amplifier (Appendix D) which turned the current into a voltage, further amplified the signal (to a total gain of 10 fold), and AC coupled the signal. The AC coupled signal contained the photobleaching information (low frequency fluorescence intensities) and was sent to the data acquisition card for further processing on the computer. The remaining radio-frequency (RF) components of the signal were sent to a 20 dB amplifier and then to the custom-built I/Q demodulator. Before the signal was processed on the I/Q demodulator, it was input to an automatic gain control (AGC) circuit on-board of the demodulator which controlled the gain of the input signal to keep it at a constant root mean square (RMS) value of 100 mV. This signal was then sent to the

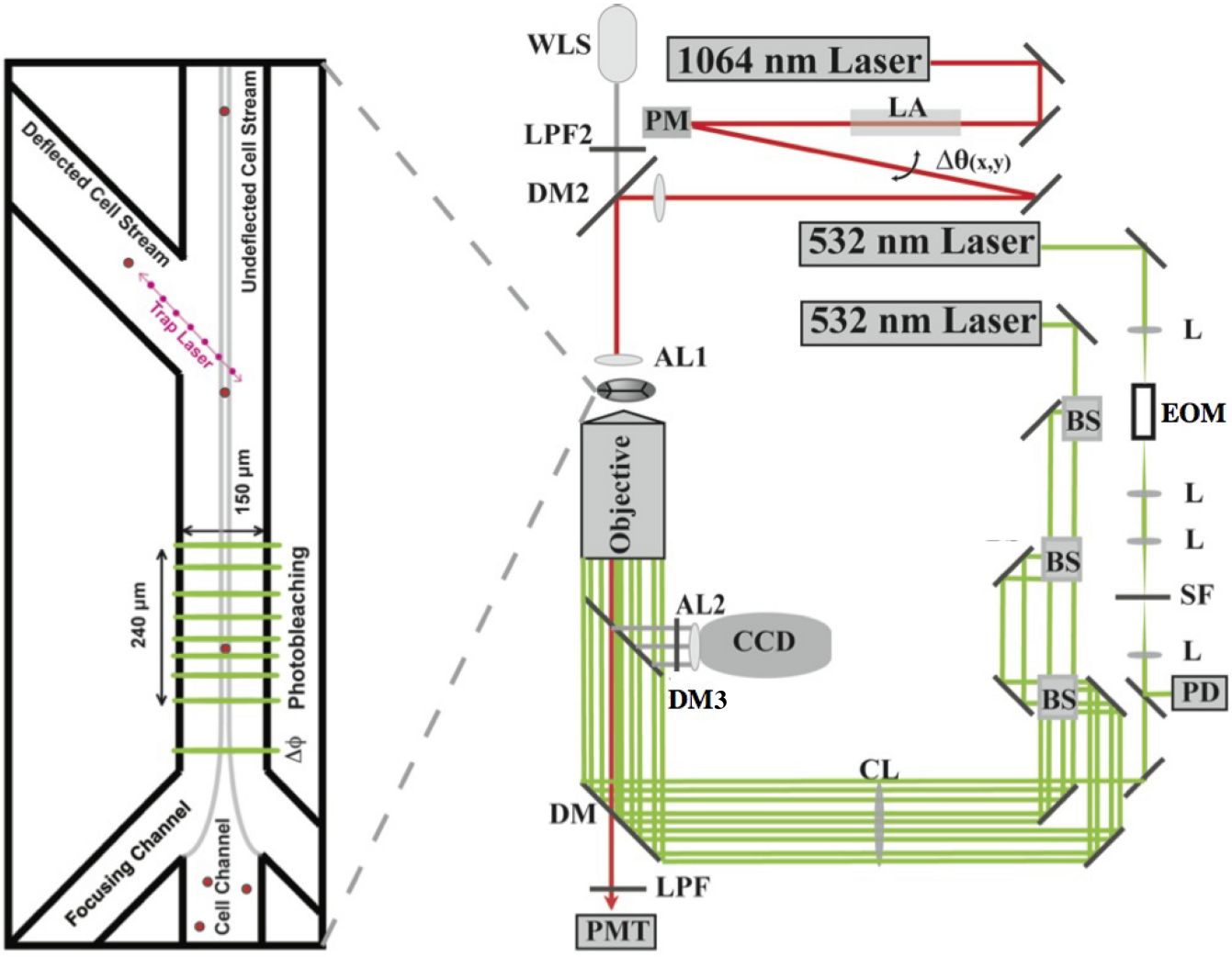

Figure 6.2: Optical setup for fluorescence lifetime and photostability detection where LA are columnizing optics, L's are focal-length matched mirrors, SF is a spatial filter, PD is a photodiode, BS are 50:50 beam splitters, CL is a cylindrical lens, CCD is a camera, DM2 is a notch 532 nm dichroic, LPF2 is a 760 nm long pass filter, PM is a piezo-tilt mirror, AL2 is a 523 and 1064 nm notch filter, DM3 is a 400-700 nm transmitting, 720-890 nm reflecting dichroic, DM is a 532 nm notch dichroic mirror, WLS is a wight light source, AL1 is a high numerical aperture aspheric lens, and LFP is a 540 nm long pass filter.

I/Q demodulation chip which output the in phase (I) and quadrature (Q) components (Appendix D).

An I/Q demodulator compares the 29.5 MHz sine wave from the arbitrary wave form generator (AWG, which is the same signal used to modulate the EOM) with the resulting fluorescence signal. First, the reference signal from the wave form generator is split along two paths. One path maintains the phase of the sine wave and the other shifts it 90°. Each reference signal is then mixed (frequency multiplied) with the RF fluorescence signal. Fluorescence signal which was mixed with the 90°-shifted reference signal carries the Q component and the fluorescence signal which was mixed with the 0°-shifted reference signal carries the I component. The I and Q peaks were then found using a Gaussian-fitting routine on LabView and the arbitrary phase shift (ϕ_{arb}) was then calculated as:

$$\arctan(Q/I) = \phi_{arb} \tag{6.3}$$

The I/Q demodulator can impose an additional phase shift to the signal in steps of 22.5°. This parameter was adjusted to maintain I≈Q to ensure an ≈45° arbitrary phase shift for maximum signal to noise levels. All phase shifts are reported as arbitrary as the electronics add additional phase shifts to the phase shift resulting from the fluorescence lifetime. These extra phase shifts arise from the distance the photons travel in the setup, additional lengths of cables between the electronics, and delays caused by the electronics themselves [51, 128]. However, differences in PMT voltage settings were not found to appreciably change the detected arbitrary phase shift unlike those reported in [129]. Additionally, phase shifts caused by the setup add linearly to the lifetime phase shift [128].

6.4.2 Measurements on Texas Red Labeled Beads

Fluorescent beads labeled with Texas Red dye (Bangs Laboratories) were assayed in the lifetime cytometer. Texas Red had a reported lifetime of 4.15 ns at pH=7 [130]. This lifetime measurement was made on purified dye in buffer and so the lifetime of the dye when conjugated to

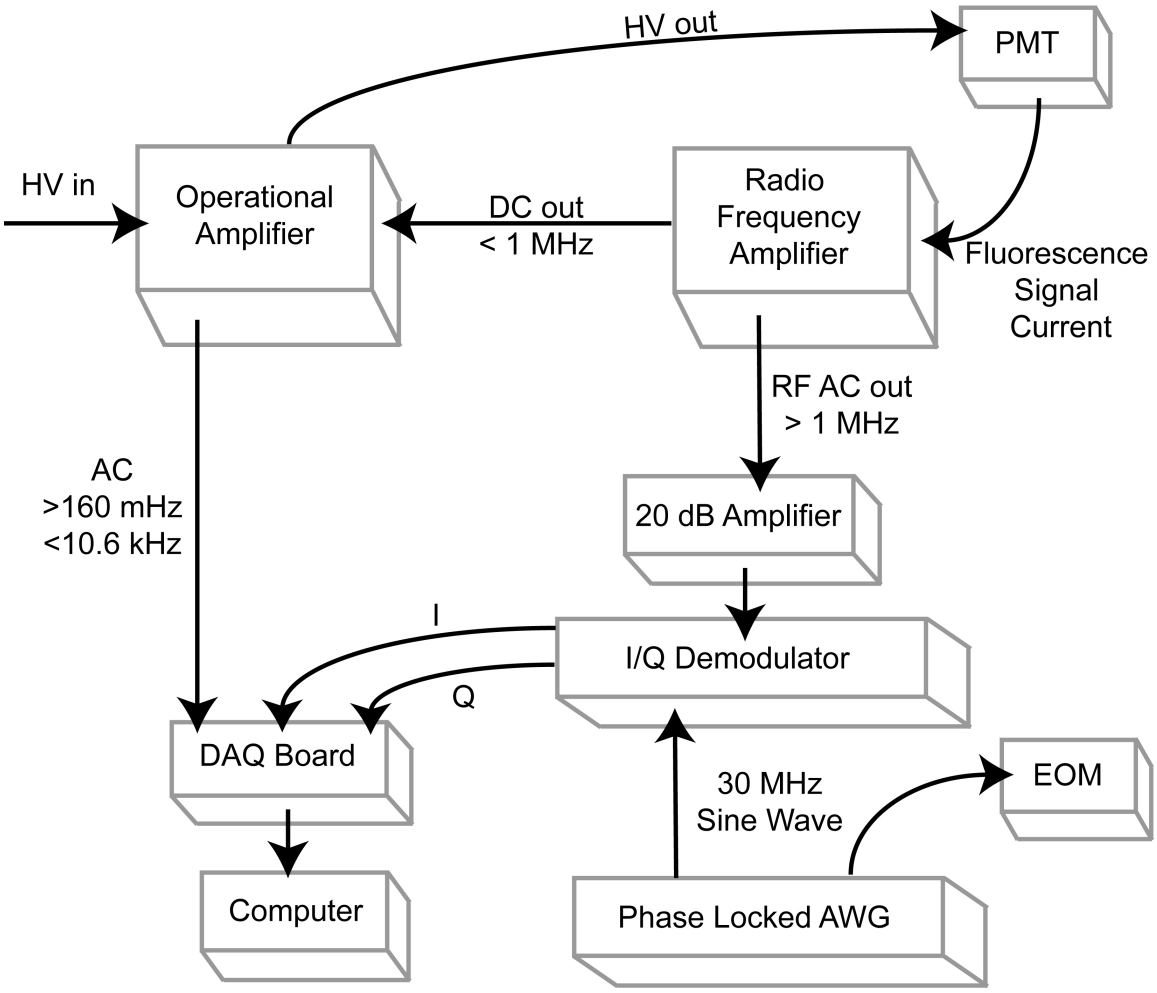

Figure 6.3: Electronics of the lifetime and photobleaching setup.

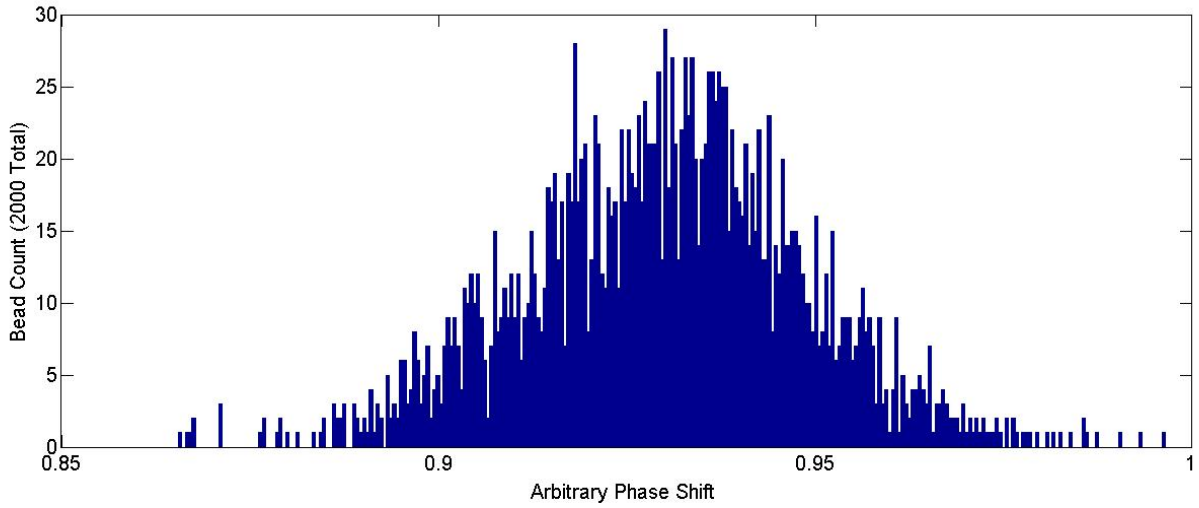

Figure 6.4: Arbitrary phase shift histogram of Texas Red beads. The mean was 0.9297 and the standard deviation was 0.0196, resulting in a coefficient of variation (CV) of 2%.

the beads suspended in a 20% (w/v) glycerol solution should be determined experimentally. The beads showed a narrow standard deviation of 0.0196 and an average phase shift of 0.9297 (arbitrary units) resulting in a CV of 2% (Figure 6.4) which is approaching that reported in literature (1% [129]).

6.4.3 Measurements on Cells Expressing Red Fluorescent Proteins

Given the low CV of the beads assayed, cells expressing mOrange2 were next assayed. mOrange2 has a lifetime of 3.28 ns (measured on purified protein [49]) and also showed a very narrow standard deviation of 0.0171 and a mean of 0.7234 (arbitrary units) resulting in a CV of 2.4% (Figure 6.5).

Three populations of cells, each expressing either mOrange2, mCherry, or TagRFP-T, were then assayed individually to determine their arbitrary phase shifts and then mixed together to test the instrument's resolving power (Figure 6.6). mCherry showed a larger arbitrary phase shift (0.9721 arbitrary units) than TagRFP-T (0.8403 arbitrary units) which was larger than mOrange2 (0.7233 arbitrary units). These phase shifts are in opposite order of the proteins' lifetimes which

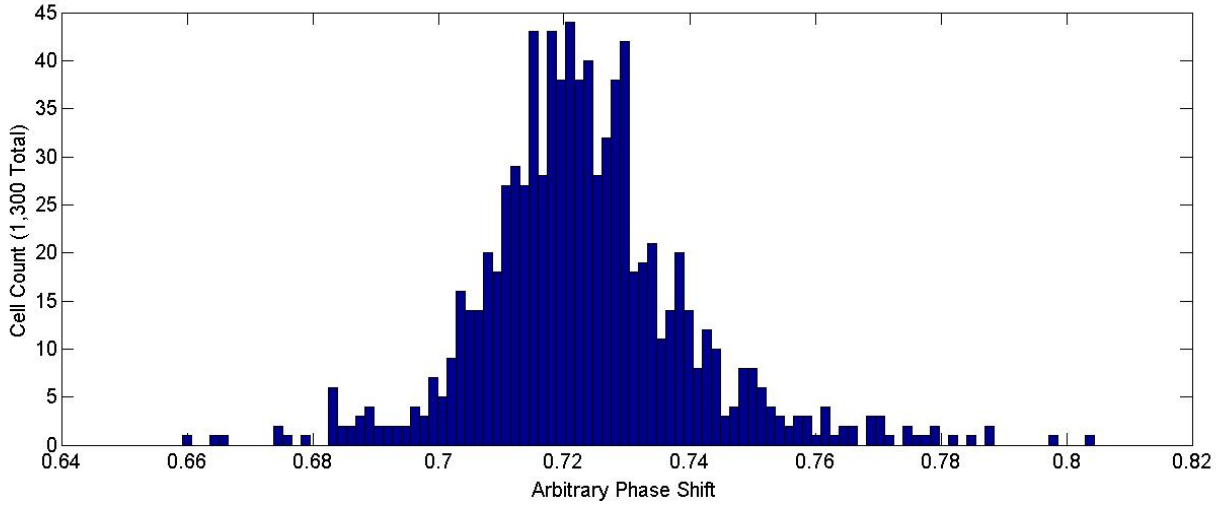

Figure 6.5: Arbitrary phase shift histogram of HeLa cells expressing mOrange2. The mean was 0.7234 and the standard deviation was 0.0171, resulting in a CV of 2.4%.

were 1.87 ns, 2.71 ns, and 3.28 ns for mCherry, TagRFP-T and mOrange2 respectively [49]. It remains unclear whether the arbitrary phase shift caused by the electronics added to the phase shift resulting from the fluorescence lifetime could result in this ordering. Texas Red, which has a reported lifetime longer than that of mOrange2, showed an arbitrary phase shift intermediate to that of mCherry and TagRFP-T. Therefore, while the proteins were resolved, the correlation between the fluorescence lifetime and arbitrary phase shift does not appear to be linear. However, as discussed earlier, the reported lifetime of Texas Red was not measured under the exact conditions that the dye was assayed on our cytometer and so this must be verified to conclude that the relationship between the fluorecence lifetime and arbitrary phase shift is indeed non-linear. Additionally, DSC has been shown to have a non-negligible contribution to fluorescence lifetime measurements when the excitation frequency approaches that of the dark-state lifetime [131]. While our excitation frequency is much faster than the dark-state lifetimes of these FPs, calculations should be done to fully understand their contribution.

Detection of the lifetimes of the cells also proved difficult. While the fluorecence signal from each cell was of a typical magnitude (0.2-10 V), The signal to noise value for the I and Q data was prohibitively low, frequently approaching 1, which meant most peaks on these channels were not detected. It is interesting to note that, I and Q data peak magnitudes correlate with fluorescence intensity (theoretically and experimentally) but the phase shifts from the lifetimes do not (theoretically and experimentally). For these cells, I and Q peaks were only detected for the brightest cells (fluorescence signal $>$ 9 V). It is also interesting to note that cells and beads which had longer lifetimes (which would theoretically result in larger phase shifts) were the best detected due to large signal to noise values ($>$ 2) on the I and Q data (data not shown).

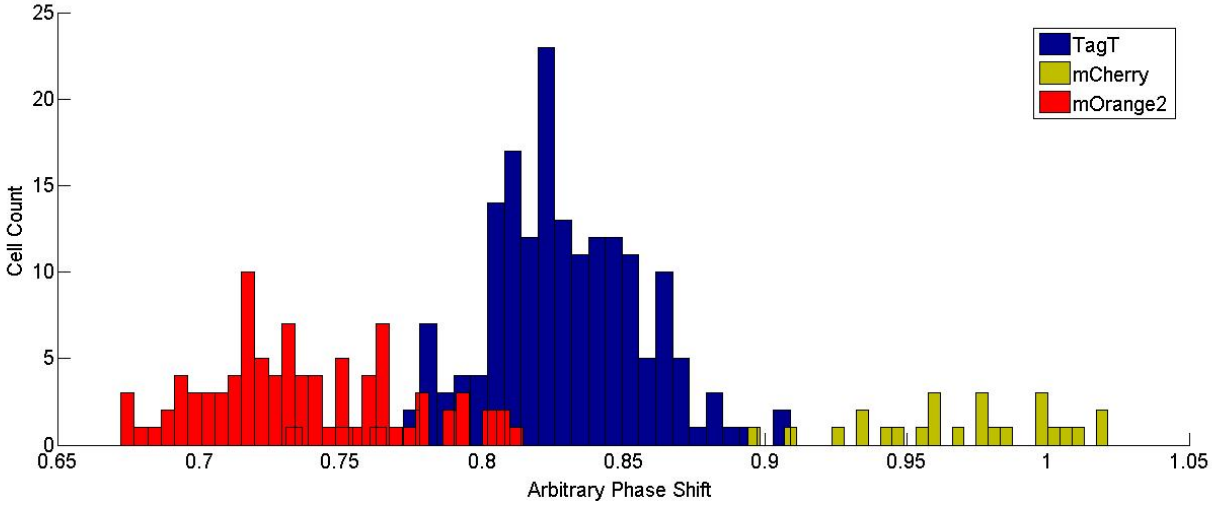

Figure 6.6: Arbirtrary fluorescence phase shifts of a mixture of TagFRP-T, mOrange2, and mCherry. Standard deviations are not reported due to low sample numbers.

6.5 Conclusions and Future Directions

We have presented the completed experimental setup for a multiparametric cell-sorter capable of differentiating RFPs on the basis of photostability and fluorescence lifetime. Preliminary data indicates that the instrument is capable of resolving RFPs on the basis of their fluorescence lifetimes with narrow CVs. However, the correlation between fluorescence lifetimes and arbitrary phase shift must be further examined to reliably sort cells for increased quantum yield. To solve this problem, the lifetime of the Texas Red beads should be measured under our experimental conditions. Additionally, computational studies (such as those presented in [131]) should be carried out to understand the contribution of dark states in FPs to lifetime measurements. Lastly the phase shift induced by our electronics should be carefully investigated (such as that detailed in [128]) to determine if it could lead to an inverse-linear correlation between fluorescence lifetime and arbitrary phase shift.

Detection of cells must also be made more reliable as only the brightest cells or cells with the largest fluorescence lifetimes (phase shifts) are currently detected. Solutions to this problem require a better understanding of the phase shift caused by the electronics. With this knowledge, it is possible that the electronics could be reconfigured to offer better signal to noise or that a simple amplifier which AC couples the I and Q data (such as that used for the photobleaching signal in Figure 6.3) could be added after the I/Q demodulator. Once these issues are solved, libraries will be enriched on the basis of quantum yield and photostability to fully demonstrate the capabilities of this new instrument.

Bibliography

[1] M. Chalfie, Y. Tu, G. Euskirchen, W. W. Ward, D. C. Prasher, et al., "Green fluorescent protein as a marker for gene expression," Trends in Genetics, vol. 10, no. 5, pp. 151–151, 1994.

[2] R. Y. Tsien, "The green fluorescent protein," Annual Review of Biochemistry, vol. 67, pp. 509–544, Jun 1998.

[3] D. C. Prasher, V. K. Eckenrode, W. W. Ward, F. G. Prendergast, M. J. Cormier, et al., "Primary structure of the aequorea victoria green-fluorescent protein," Gene, vol. 111, no. 2, p. 229, 1992.

[4] S. Inouye and F. I. Tsuji, "¡ i¿ aequorea¡/i¿ green fluorescent protein: Expression of the gene and fluorescence characteristics of the recombinant protein," Febs Letters, vol. 341, no. 2, pp. 277–280, 1994.

[5] A. Miyawaki, A. Sawano, T. Kogure, et al., "Lighting up cells: labelling proteins with fluorophores.," Nature Cell Biology, p. S1, 2003.

[6] N. C. Shaner, P. A. Steinbach, and R. Y. Tsien, "A guide to choosing fluorescent proteins," Nature methods, vol. 2, no. 12, pp. 905–909, 2005.

[7] V. V. Verkhusha and K. A. Lukyanov, "The molecular properties and applications of anthozoa fluorescent proteins and chromoproteins," Nature biotechnology, vol. 22, no. 3, pp. 289–296, 2004.

[8] B. N. Giepmans, S. R. Adams, M. H. Ellisman, and R. Y. Tsien, "The fluorescent toolbox for assessing protein location and function," Science Signalling, vol. 312, no. 5771, p. 217, 2006.

[9] J. Zhang, R. E. Campbell, A. Y. Ting, R. Y. Tsien, et al., "Creating new fluorescent probes for cell biology," Nature Reviews Molecular Cell Biology, vol. 3, no. 12, pp. 906–918, 2002.

[10] R. B. Robey, O. Ruiz, A. V. Santos, J. Ma, F. Kear, L.-J. Wang, C.-J. Li, A. A. Bernardo, and J. A. Arruda, "ph-dependent fluorescence of a heterologously expressed aequorea green fluorescent protein mutant: in situ spectral characteristics and applicability to intracellular ph estimation," Biochemistry, vol. 37, no. 28, pp. 9894–9901, 1998.

[11] S. W. Hell, "Far-field optical nanoscopy," Science, vol. 316, pp. 1153–1158, May 2007.

[12] D. J. Stephens and V. J. Allan, "Light microscopy techniques for live cell imaging," Science Signalling, vol. 300, no. 5616, p. 82, 2003.

[13] T. Ha and P. Tinnefeld, "Photophysics of fluorescent probes for single-molecule biophysics and super-resolution imaging," Annual Review of Physical Chemistry, vol. 63, no. 1, pp. 595–617, 2012. PMID: 22404588.

[14] H. Niwa, S. Inouye, T. Hirano, T. Matsuno, S. Kojima, M. Kubota, M. Ohashi, and F. I. Tsuji, "Chemical nature of the light emitter of the aequorea green fluorescent protein," Proceedings of the National Academy of Sciences, vol. 93, no. 24, pp. 13617–13622, 1996.

[15] N. C. Shaner, R. E. Campbell, P. A. Steinbach, B. N. G. Giepmans, A. E. Palmer, and R. Y. Tsien, "Improved monomeric red, orange and yellow fluorescent proteins derived from discosoma sp. red fluorescent protein," Nature Biotechnology, vol. 22, pp. 1567–1572, Nov 2004.

[16] E. M. Merzlyak, J. Goedhart, D. Shcherbo, M. E. Bulina, A. S. Shcheglov, A. F. Fradkov, A. Gaintzeva, K. A. Lukyanov, S. Lukyanov, T. W. J. Gadella, and et al., "Bright monomeric red fluorescent protein with an extended fluorescence lifetime," Nature Methods, vol. 4, pp. 555–557, Jun 2007.

[17] N. C. Shaner, M. Z. Lin, M. R. McKeown, P. A. Steinbach, K. L. Hazelwood, M. W. Davidson, and R. Y. Tsien, "Improving the photostability of bright monomeric orange and red fluorescent proteins," Nature Methods, vol. 5, pp. 545–551, May 2008.

[18] D. Shcherbo, E. M. Merzlyak, T. V. Chepurnykh, A. F. Fradkov, G. V. Ermakova, E. A. Solovieva, K. A. Lukyanov, E. A. Bogdanova, A. G. Zaraisky, S. Lukyanov, and et al., "Bright far-red fluorescent protein for whole-body imaging," Nature Methods, vol. 4, pp. 741–746, Aug 2007.

[19] D. A. Zacharias and R. Y. Tsien, "Molecular biology and mutation of green fluorescent protein," Methods of Biochemical Analysis, Green Fluorescent Protein: Properties, Applications and Protocols, vol. 47, p. 83, 2005.

[20] R. Heim, A. B. Cubitt, and R. Y. Tsien, "Improved green fluorescence," Nature, vol. 373, 1995.

[21] R. Heim, D. C. Prasher, and R. Y. Tsien, "Wavelength mutations and posttranslational autoxidation of green fluorescent protein," Proceedings of the National Academy of Sciences, vol. 91, no. 26, pp. 12501–12504, 1994.

[22] R. Heim, R. Y. Tsien, et al., "Engineering green fluorescent protein for improved brightness, longer wavelengths and fluorescence resonance energy transfer," Current Biology, vol. 6, no. 2, pp. 178–182, 1996.

[23] O. Griesbeck, G. S. Baird, R. E. Campbell, D. A. Zacharias, and R. Y. Tsien, "Reducing the environmental sensitivity of yellow fluorescent protein," Journal of biological chemistry, vol. 276, no. 31, pp. 29188–29194, 2001.

[24] R. E. Campbell, O. Tour, A. E. Palmer, P. A. Steinbach, G. S. Baird, D. A. Zacharias, and R. Y. Tsien, "A monomeric red fluorescent protein," Proceedings of the National Academy of Sciences, vol. 99, no. 12, pp. 7877–7882, 2002.

[25] H.-w. Ai, J. N. Henderson, S. J. Remington, and R. E. Campbell, "Directed evolution of a monomeric, bright and photostable version of clavularia cyan fluorescent protein: structural characterization and applications in fluorescence imaging," Biochemical Journal, vol. 400, no. Pt 3, p. 531, 2006.

[26] A. W. Nguyen and P. S. Daugherty, "Evolutionary optimization of fluorescent proteins for intracellular fret," Nature biotechnology, vol. 23, no. 3, pp. 355–360, 2005.

[27] M. Chattoraj, B. A. King, G. U. Bublitz, and S. G. Boxer, "Ultra-fast excited state dynamics in green fluorescent protein: multiple states and proton transfer.," Proceedings of the National Academy of Sciences, vol. 93, pp. 8362–8367, Aug 1996.

[28] P. Abbyad, W. Childs, X. Shi, and S. G. Boxer, "Dynamic stokes shift in green fluorescent protein variants," Proceedings of the National Academy of Sciences, vol. 104, pp. 20189–20194, Dec 2007.

[29] M. Drobizhev, S. Tillo, N. S. Makarov, T. E. Hughes, and A. Rebane, "Color hues in red fluorescent proteins are due to internal quadratic stark effect," The Journal of Physical Chemistry B, vol. 113, pp. 12860–12864, Oct 2009.

[30] G. S. Harms, L. Cognet, P. H. Lommerse, G. A. Blab, and T. Schmidt, "Autofluorescent proteins in single-molecule research: Applications to live cell imaging microscopy," Biophysical Journal, vol. 80, pp. 2396–2408, May 2001.

[31] R. M. Dickson, A. B. Cubitt, R. Y. Tsien, and W. E. Moerner, "on/off blinking and switching behaviour of single molecules of green fluorescent protein," Nature, vol. 388, July 1997.

[32] A. A. Heikal, S. T. Hess, G. S. Baird, R. Y. Tsien, and W. W. Webb, "Molecular spectroscopy and dynamics of intrinsically fluorescent proteins: Coral red (dsred) and yellow (citrine)," Proceedings of the National Academy of Sciences, vol. 97, pp. 11996–12001, Oct 2000.

[33] D. Sinnecker, P. Voigt, N. Hellwig, and M. Schaefer, "Reversible photobleaching of enhanced green fluorescent proteins," Biochemistry, vol. 44, no. 18, pp. 7085–7094, 2005. 924EU Times Cited:28 Cited References Count:33.

[34] P. Schwille, S. Kummer, A. A. Heikal, W. E. Moerner, and W. W. Webb, "Fluorescence correlation spectroscopy reveals fast optical excitation-driven intramolecular dynamics of yellow fluorescent proteins," Proceedings of the National Academy of Sciences, vol. 97, pp. 151–156, Jan 2000.

[35] U. Haupts, S. Maiti, P. Schwille, and W. W. Webb, "Dynamics of fluorescence fluctuations in green fluorescent protein observed by fluorescence correlation spectroscopy," Proceedings of the National Academy of Sciences, vol. 95, pp. 13573–13578, Nov 1998.

[36] G. Jung, J. Wiehler, and A. Zumbusch, "The photophysics of green fluorescent protein: influence of the key amino acids at positions 65, 203, and 222," Biophysical journal, vol. 88, no. 3, pp. 1932–1947, 2005.

[37] J. Hendrix, C. Flors, P. Dedecker, J. Hofkens, and Y. Engelborghs, "Dark states in monomeric red fluorescent proteins studied by fluorescence correlation and single molecule spectroscopy," Biophysical Journal, vol. 94, pp. 4103–4113, May 2008.

[38] J. N. Henderson, H. W. Ai, R. E. Campbell, and S. J. Remington, "Structural basis for reversible photobleaching of a green fluorescent protein homologue," Proceedings of the National Academy of Sciences of the United States of America, vol. 104, no. 16, pp. 6672–6677, 2007. 159ME Times Cited:32 Cited References Count:44.

[39] K. A. Lukyanov, D. M. Chudakov, S. Lukyanov, and V. V. Verkhusha, "Photoactivatable fluorescent proteins," Nature Reviews Molecular Cell Biology, vol. 6, no. 11, pp. 885–890, 2005.

[40] G. Donnert, C. Eggeling, and S. W. Hell, "Major signal increase in fluorescence microscopy through dark-state relaxation," Nature Methods, vol. 4, pp. 81–86, Dec 2007.

[41] K. Mudalige, S. Habuchi, P. M. Goodwin, R. K. Pai, F. De Schryver, and M. Cotlet, "Photophysics of the red chromophore of hcred: Evidence for cistrans isomerization and protonation-state changes," The Journal of Physical Chemistry B, vol. 114, pp. 4678–4685, Apr 2010.

[42] F. Malvezzi-Campeggi, M. Jahnz, K. G. Heinze, P. Dittrich, and P. Schwille, "Light-induced flickering of dsred provides evidence for distinct and interconvertible fluorescent states," Biophysical Journal, vol. 81, pp. 1776–1785, Sep 2001.

[43] A. Schenk, S. Ivanchenko, C. Röcker, J. Wiedenmann, and G. Nienhaus, "Photodynamics of red fluorescent proteins studied by fluorescence correlation spectroscopy," Biophysical Journal, vol. 86, Jan 2004.

[44] X. Ragàs, L. P. Cooper, J. H. White, S. Nonell, and C. Flors, "Quantification of photosensitized singlet oxygen production by a fluorescent protein," ChemPhysChem, vol. 12, pp. 161–165, Jan 2011.

[45] L. Greenbaum, C. Rothmann, R. Lavie, and Z. Malik, "Green fluorescent protein photobleaching: a model for protein damage by endogenous and exogenous singlet oxygen," Biological chemistry, vol. 381, no. 12, pp. 1251–1258, 2000.

[46] A. Diaspro, S. Krol, B. Campanini, F. Cannone, and G. Chirico, "Enhanced green fluorescent protein (gfp) fluorescence after polyelectrolyte caging," Opt. Express, vol. 14, pp. 9815–9824, 2006.

[47] C. K. Regmi, Y. R. Bhandari, B. S. Gerstman, and P. P. Chapagain, "Exploring the diffusion of molecular oxygen in the red fluorescent protein mcherry using explicit oxygen molecular dynamics simulations," The Journal of Physical Chemistry B, 2013.

[48] P. P. Chapagain, C. K. Regmi, and W. Castillo, "Fluorescent protein barrel fluctuations and oxygen diffusion pathways in mcherry," The Journal of chemical physics, vol. 135, no. 23, pp. 235101–235101, 2011.

[49] K. M. Dean, J. L. Lubbeck, J. K. Binder, L. R. Schwall, R. Jimenez, and A. Palmer, "Analysis of red-fluorescent proteins provides insight into dark-state conversion and photodegradation," Biophysical Journal, vol. 101, no. 4, pp. 961–969, 2011. 810CS Times Cited:0 Cited References Count:30.

[50] N. C. Shaner, G. H. Patterson, and M. W. Davidson, "Advances in fluorescent protein technology," Journal of Cell Science, vol. 120, no. 24, pp. 4247–4260, 2007. 249QG Times Cited:192 Cited References Count:79.

[51] J. R. Lakowicz, Principles of fluorescence spectroscopy. New York: Springer, 2006.

[52] M. Ormo, A. B. Cubitt, K. Kallio, L. A. Gross, R. Y. Tsien, S. J. Remington, et al., "Crystal structure of the aequorea victoria green fluorescent protein," SCIENCE-NEW YORK THEN WASHINGTON-, pp. 1392–1395, 1996.

[53] F. V. Subach, K. D. Piatkevich, and V. V. Verkhusha, "Directed molecular evolution to design advanced red fluorescent proteins," Nature Methods, vol. 8, pp. 1019–1026, Nov 2011.

[54] J. Goedhart, L. Van Weeren, M. A. Hink, N. O. Vischer, K. Jalink, and T. W. Gadella, "Bright cyan fluorescent protein variants identified by fluorescence lifetime screening," Nature methods, vol. 7, no. 2, pp. 137–139, 2010.

[55] T. Nagai, K. Ibata, E. S. Park, M. Kubota, K. Mikoshiba, and A. Miyawaki, "A variant of yellow fluorescent protein with fast and efficient maturation for cell-biological applications," Nature biotechnology, vol. 20, no. 1, pp. 87–90, 2002.

[56] S. Pletnev, D. Shcherbo, D. M. Chudakov, N. Pletneva, E. M. Merzlyak, A. Wlodawer, Z. Dauter, and V. Pletnev, "A crystallographic study of bright far-red fluorescent protein mkate reveals ph-induced cis-trans isomerization of the chromophore," Journal of Biological Chemistry, vol. 283, pp. 28980–28987, Aug 2008.

[57] S. Kredel, K. Nienhaus, F. Oswald, M. Wolff, S. Ivanchenko, F. Cymer, A. Jeromin, F. J. Michel, K.-D. Spindler, R. Heilker, and et al., "Optimized and far-red-emitting variants of fluorescent protein eqfp611," Chemistry and Biology, vol. 15, pp. 224–233, Mar 2008.

[58] M. Chalfie and K. Kobs, Green fluorescent protein: properties, applications and protocols. Hoboken, N. J.: Wiley-Interscience, 2006.

[59] T. Karstens and K. Kobs, "Rhodamine b and rhodamine 101 as reference substances for fluorescence quantum yield measurements," The Journal of Physical Chemistry, vol. 84, pp. 1871–1872, Jul 1980.

[60] D. Magde, J. H. Brannon, T. L. Cremers, and J. Olmsted, "Absolute luminescence yield of cresyl violet. a standard for the red," The Journal of Physical Chemistry, vol. 83, pp. 696–699, Mar 1979.

[61] F. Mueller, P. Wach, and J. G. McNally, "Evidence for a common mode of transcription factor interaction with chromatin as revealed by improved quantitative fluorescence recovery after photobleaching," Biophysical Journal, vol. 94, pp. 3323–3339, Apr 2008.

[62] J. L. Fiore, J. H. Hodak, O. Piestert, C. D. Downey, and D. J. Nesbitt, "Monovalent and divalent promoted gaaa tetraloop-receptor tertiary interactions from freely diffusing single-molecule studies," Biophysical Journal, vol. 95, pp. 3892–3905, Oct 2008.

[63] J. C. Butcher, Numerical methods for ordinary differential equations. Chichester, England; Hoboken, NJ: Wiley, 2008.

[64] A. C. Hindmarsh, P. N. Brown, K. E. Grant, S. L. Lee, R. Servan, D. E. Shumaker, and C. S. Woodward, SUNDIALS: Suite of nonlinear and differential/algebraic equation solvers. Acm T Math Software, 2005.

[65] M. Z. Lin, M. R. McKeown, H.-L. Ng, T. A. Aguilera, N. C. Shaner, R. E. Campbell, S. R. Adams, L. A. Gross, W. Ma, T. Alber, and et al., "Autofluorescent proteins with excitation in the optical window for intravital imaging in mammals," Chemistry and Biology, vol. 16, pp. 1169–1179, Nov 2009.

[66] L. Wang, W. C. Jackson, P. A. Steinbach, and R. Y. Tsien, "Evolution of new nonantibody proteins via iterative somatic hypermutation," Proceedings of the National Academy of Sciences, vol. 101, pp. 16745–16749, Nov 2004.

[67] O. M. Subach, V. N. Malashkevich, W. D. Zencheck, K. S. Morozova, K. D. Piatkevich, S. C. Almo, and V. V. Verkhusha, "Structural characterization of acylimine-containing blue and red chromophores in mtagbfp and tagrfp fluorescent proteins," Chemistry and Biology, vol. 17, pp. 333–341, Apr 2010.

[68] K. Nienhaus, H. Nar, R. Heilker, J. Wiedenmann, and G. U. Nienhaus, "Transcis isomerization is responsible for the red-shifted fluorescence in variants of the red fluorescent protein eqfp611," Journal of the American Chemical Society, vol. 130, pp. 12578–12579, Sep 2008.

[69] W. Yan, D. Xie, and J. Zeng, "The 559-to-600 nm shift observed in red fluorescent protein eqfp611 is attributed to cis–trans isomerization of the chromophore in an anionic protein pocket," Physical Chemistry Chemical Physics, vol. 11, no. 29, p. 6042, 2009.

[70] G. Patterson, S. Knobel, W. Sharif, S. Kain, and D. Piston, "Use of the green fluorescent protein and its mutants in quantitative fluorescence microscopy," Biophysical Journal, vol. 73, pp. 2782–2790, Nov 1997.

[71] G.-J. Kremers, K. L. Hazelwood, C. S. Murphy, M. W. Davidson, and D. W. Piston, "Photoconversion in orange and red fluorescent proteins," Nature Methods, vol. 6, pp. 355–358, Apr 2009.

[72] Z. Petrášek and P. Schwille, "Photobleaching in two-photon scanning fluorescence correlation spectroscopy," ChemPhysChem, vol. 9, pp. 147–158, Jan 2008.

[73] G. Nishimura and M. Kinjo, "Systematic error in fluorescence correlation measurements identified by a simple saturation model of fluorescence," Analytical Chemistry, vol. 76, pp. 1963–1970, Apr 2004.

[74] I. Gregor, D. Patra, and J. Enderlein, "Optical saturation in fluorescence correlation spectroscopy under continuous-wave and pulsed excitation," ChemPhysChem, vol. 6, pp. 164–170, Jan 2005.

[75] S. Veettil, N. Budisa, and G. Jung, "Photostability of green and yellow fluorescent proteins with fluorinated chromophores, investigated by fluorescence correlation spectroscopy," Biophysical Chemistry, vol. 136, pp. 38–43, Jul 2008.

[76] B. Hinkeldey, A. Schmitt, and G. Jung, "Comparative photostability studies of bodipy and fluorescein dyes by using fluorescence correlation spectroscopy," ChemPhysChem, vol. 9, pp. 2019–2027, Oct 2008.

[77] C. Eggeling, J. Widengren, L. Brand, J. Schaffer, S. Felekyan, and C. A. M. Seidel, "Analysis of photobleaching in single-molecule multicolor excitation and frster resonance energy transfer

measurementsä," The Journal of Physical Chemistry A, vol. 110, no. 9, pp. 2979–2995, 2006. PMID: 16509620.

[78] C. Eggeling, A. Volkmer, and C. A. M. Seidel, "Molecular photobleaching kinetics of rhodamine 6g by one- and two-photon induced confocal fluorescence microscopy," ChemPhysChem, vol. 6, pp. 791–804, May 2005.

[79] H. M. Shapiro, "Multistation multiparameter flow-cytometry - a critical-review and rationale," Cytometry, vol. 3, no. 4, pp. 227–243, 1983. Pw418 Times Cited:104 Cited References Count:200.

[80] C. G. Wade, R. H. Rhyne, W. H. Woodruff, D. P. Bloch, and J. C. Bartholomew, "Spectra of cells in flow cytometry using a vidicon detector," Journal of Histochemistry and Cytochemistry, vol. 27, no. 6, pp. 1049–1052, 1979. Hb751 Times Cited:14 Cited References Count:16.

[81] G. Goddard, J. C. Martin, M. Naivar, P. M. Goodwin, S. W. Graves, R. Habbersett, J. P. Nolan, and J. H. Jett, "Single particle high resolution spectral analysis flow cytometry," Cytometry Part A, vol. 69A, no. 8, pp. 842–851, 2006. 089WE Times Cited:16 Cited References Count:53.

[82] P. F. Mullaney, M. A. Vandilla, J. R. Coulter, and P. N. Dean, "Cell sizing - a light scattering photometer for rapid volume determination," Review of Scientific Instruments, vol. 40, no. 8, p. 1029, 1969. D8859 Times Cited:136 Cited References Count:10.

[83] H. R. Hulett, W. A. Bonner, J. Barrett, and Herzenbe.La, "Cell sorting - automated separation of mammalian cells as a function of intracellular fluorescence," Science, vol. 166, no. 3906, p. 747, 1969. E5938 Times Cited:128 Cited References Count:7.

[84] W. A. Bonner, R. G. Sweet, H. R. Hulett, and Herzenbe.La, "Fluorescence activated cell sorting," Review of Scientific Instruments, vol. 43, no. 3, p. 404, 1972. L8456 Times Cited:303 Cited References Count:8.

[85] H. R. Hulett, W. A. Bonner, R. G. Sweet, and Herzenbe.La, "Development and application of a rapid cell sorter," Clinical Chemistry, vol. 19, no. 8, pp. 813–816, 1973. Q3301 Times Cited:124 Cited References Count:5.

[86] J. A. Steinkamp, T. M. Yoshida, and J. C. Martin, "Flow cytometer for resolving signals from heterogeneous fluorescence emissions and quantifying lifetime in fluorochrome-labeled cells particles by phase-sensitive detection," Review of Scientific Instruments, vol. 64, no. 12, pp. 3440–3450, 1993. Mm177 Times Cited:31 Cited References Count:35.

[87] J. P. Houston, M. A. Naivar, and J. P. Freyer, "Digital analysis and sorting of fluorescence lifetime by flow cytometry," Cytometry Part A, vol. 77A, no. 9, pp. 861–872, 2010. 646AU Times Cited:0 Cited References Count:18.

[88] H. H. Engelhard, J. L. Krupka, and K. D. Bauer, "Simultaneous quantification of c-myc oncoprotein, total cellular protein, and dna content using multiparameter flow-cytometry," Cytometry, vol. 12, no. 1, pp. 68–76, 1991. En249 Times Cited:24 Cited References Count:43.

[89] G. Vandenengh and C. Farmer, "Photobleaching and photon saturation in flow-cytometry," Cytometry, vol. 13, no. 7, pp. 669–677, 1992. Jn954 Times Cited:30 Cited References Count:18.

[90] R. M. P. Doornbos, B. G. deGrooth, and J. Greve, "Experimental and model investigations of bleaching and saturation of fluorescence in flow cytometry," Cytometry, vol. 29, no. 3, pp. 204–214, 1997. Ye060 Times Cited:7 Cited References Count:44.

[91] J. B. Knight, A. Vishwanath, J. P. Brody, and R. H. Austin, "Hydrodynamic focusing on a silicon chip: Mixing nanoliters in microseconds," Physical Review Letters, vol. 80, no. 17, pp. 3863–3866, 1998. Zj826 Times Cited:389 Cited References Count:17.

[92] J. T. Verdeyen, Laser electronics. Prentice Hall series in solid state physical electronics, Englewood Cliffs, N.J.: Prentice Hall, 3rd ed., 1994. 93002184 Joseph T. Verdeyen. ill. ; 25 cm. Includes bibliographical references and index.

[93] D. Li, Encyclopedia of Microfluidics and Nanofluidics. Boston, MA: Springer-Verlag, 2008. [electronic resource] / edited by Dongqing Li. Access is available to the Yale community. Springer eBooks. Yale Internet Resource None Online resource.

[94] Z. Wang, J. El-Ali, M. Engelund, T. Gotsaed, I. R. Perch-Nielsen, K. B. Mogensen, D. Snakenborg, J. P. Kutter, and A. Wolff, "Measurements of scattered light on a microchip flow cytometer with integrated polymer based optical elements," Lab on a Chip, vol. 4, no. 4, pp. 372–377, 2004. 839VY Times Cited:102 Cited References Count:46.

[95] D. P. Schrum, C. T. Culbertson, S. C. Jacobson, and J. M. Ramsey, "Microchip flow cytometry using electrokinetic focusing," Analytical Chemistry, vol. 71, no. 19, pp. 4173–4177, 1999. 241RM Times Cited:150 Cited References Count:29.

[96] Y. Morimoto, W. H. Tan, and S. Takeuchi, "Three-dimensional axisymmetric flow-focusing device using stereolithography," Biomedical Microdevices, vol. 11, no. 2, pp. 369–377, 2009. 417QR Times Cited:8 Cited References Count:27.

[97] X. L. Mao, S. C. S. Lin, C. Dong, and T. J. Huang, "Single-layer planar on-chip flow cytometer using microfluidic drifting based three-dimensional (3d) hydrodynamic focusing," Lab on a Chip, vol. 9, no. 11, pp. 1583–1589, 2009. 448NN Times Cited:37 Cited References Count:43.

[98] X. Shu, N. C. Shaner, C. A. Yarbrough, R. Y. Tsien, and S. J. Remington, "Novel chromophores and buried charges control color in mfruits," Biochemistry, vol. 45, no. 32, pp. 9639–47, 2006. GM72033/GM/NIGMS NIH HHS/United States NS27177/NS/NINDS NIH HHS/United States Journal Article Research Support, N.I.H., Extramural Research Support, Non-U.S. Gov't Research Support, U.S. Gov't, Non-P.H.S. United States.

[99] M. M. Wang, E. Tu, D. E. Raymond, J. M. Yang, H. C. Zhang, N. Hagen, B. Dees, E. M. Mercer, A. H. Forster, I. Kariv, P. J. Marchand, and W. F. Butler, "Microfluidic sorting of mammalian cells by optical force switching," Nature Biotechnology, vol. 23, no. 1, pp. 83–87, 2005. 885ZK Times Cited:122 Cited References Count:34.

[100] C. H. Chen, S. H. Cho, F. Tsai, A. Erten, and Y. H. Lo, "Microfluidic cell sorter with integrated piezoelectric actuator," Biomedical Microdevices, vol. 11, no. 6, pp. 1223–1231, 2009. 518UT Times Cited:12 Cited References Count:23.

[101] J. L. Lubbeck, K. M. Dean, H. Ma, A. E. Palmer, and R. Jimenez, "Microfluidic flow cytometer for quantifying photobleaching of fluorescent proteins in cells," Analytical Chemistry, vol. 84, no. 9, pp. 3929–3937, 2012.

[102] P. C. H. Li and D. J. Harrison, "Transport, manipulation, and reaction of biological cells on-chip using electrokinetic effects," Analytical Chemistry, vol. 69, no. 8, pp. 1564–1568, 1997.

[103] A. Y. Fu, C. Spence, A. Scherer, F. H. Arnold, S. R. Quake, et al., "A microfabricated fluorescence-activated cell sorter," Nature biotechnology, vol. 17, no. 11, pp. 1109–1111, 1999.

[104] V. Kiermer, "Facs-on-a-chip," Nature Methods, vol. 2, no. 2, pp. 91–91, 2005.

[105] T. Franke, S. Braunmüller, L. Schmid, A. Wixforth, and D. Weitz, "Surface acoustic wave actuated cell sorting (sawacs)," Lab on a Chip, vol. 10, no. 6, pp. 789–794, 2010.

[106] M. V. Patel, A. R. Tovar, and A. P. Lee, "Lateral cavity acoustic transducer as an on-chip cell/particle microfluidic switch," Lab on a Chip, vol. 12, no. 1, pp. 139–145, 2012.

[107] T.-H. Wu, Y. Chen, S.-Y. Park, J. Hong, T. Teslaa, J. F. Zhong, D. Di Carlo, M. A. Teitell, and P.-Y. Chiou, "Pulsed laser triggered high speed microfluidic fluorescence activated cell sorter," Lab on a Chip, vol. 12, no. 7, pp. 1378–1383, 2012.

[108] A. Ashkin, J. Dziedzic, and T. Yamane, "Optical trapping and manipulation of single cells using infrared laser beams," Nature, vol. 330, no. 6150, pp. 769–771, 1987.

[109] R. Applegate Jr, J. Squier, T. Vestad, J. Oakey, D. Marr, et al., "Optical trapping, manipulation, and sorting of cells and colloids in microfluidic systems with diode laser bars," Optics express, vol. 12, no. 19, pp. 4390–4398, 2004.

[110] S. K. Hoi, C. Udalagama, C. H. sow, F. Watt, and A. A. Bettiol, "Microfluidic sorting system based on optical force switching," Applied Physics B-Lasers and Optics, vol. 97, pp. 859–865, 2009.

[111] X. Wang, S. Chen, M. Kong, Z. Wang, K. D. Costa, R. A. Li, and D. Sun, "Enhanced cell sorting and manipulation with combined optical tweezer and microfluidic chip technologies," Lab on a Chip, vol. 11, no. 21, pp. 3656–3662, 2011.

[112] T. D. Perroud, J. N. Kaiser, J. C. Sy, T. W. Lane, C. S. Branda, A. K. Singh, and K. D. Patel, "Microfluidic-based cell sorting of francisella tularensis infected macrophages using optical forces," Analytical chemistry, vol. 80, no. 16, pp. 6365–6372, 2008.

[113] C. Eggeling, J. Fries, L. Brand, R. Günther, and C. Seidel, "Monitoring conformational dynamics of a single molecule by selective fluorescence spectroscopy," Proceedings of the National Academy of Sciences, vol. 95, no. 4, pp. 1556–1561, 1998.

[114] J. Pawley, Handbook of biological confocal microscopy. Springer, 2006.

[115] J. L. Lubbeck, K. M. Dean, L. M. Davis, A. E. Palmer, and R. Jimenez, "Microfluidic cytometer for simultaneous high-throughput screening of fluorescent proteins on the basis of fluorescence lifetime, photostability, and brightness," Biophysical Journal, vol. 102, p. 208, 2012.

[116] C. Mio, T. Gong, A. Terray, and D. Marr, "Design of a scanning laser optical trap for multiparticle manipulation," Review of Scientific Instruments, vol. 71, no. 5, pp. 2196–2200, 2000.

[117] G. Czerlinski, D. Reid, A. Apostol, K. Bauer, and D. Scarpelli, "Determination of the density of cells from sedimentation studies at 1g," Journal of Biological Physics, vol. 15, no. 2, pp. 29–32, 1987.

[118] R. A. Chica, M. M. Moore, B. D. Allen, and S. L. Mayo, "Generation of longer emission wavelength red fluorescent proteins using computationally designed libraries," Proceedings of the National Academy of Sciences, vol. 107, no. 47, pp. 20257–20262, 2010.

[119] J. J. van Thor, T. Gensch, K. J. Hellingwerf, and L. N. Johnson, "Phototransformation of green fluorescent protein with uv and visible light leads to decarboxylation of glutamate 222," Nature Structural & Molecular Biology, vol. 9, no. 1, pp. 37–41, 2001.

[120] F. V. Subach, G. H. Patterson, S. Manley, J. M. Gillette, J. Lippincott-Schwartz, and V. V. Verkhusha, "Photoactivatable mcherry for high-resolution two-color fluorescence microscopy," Nature methods, vol. 6, no. 2, pp. 153–159, 2009.

[121] S. Habuchi, M. Cotlet, T. Gensch, T. Bednarz, S. Haber-Pohlmeier, J. Rozenski, G. Dirix, J. Michiels, J. Vanderleyden, J. Heberle, et al., "Evidence for the isomerization and decarboxylation in the photoconversion of the red fluorescent protein dsred," Journal of the American Chemical Society, vol. 127, no. 25, pp. 8977–8984, 2005.

[122] J. N. Henderson, R. Gepshtein, J. R. Heenan, K. Kallio, D. Huppert, and S. J. Remington, "Structure and mechanism of the photoactivatable green fluorescent protein," Journal of the American Chemical Society, vol. 131, no. 12, pp. 4176–4177, 2009.

[123] V. Adam, P. Carpentier, S. Violot, M. Lelimousin, C. Darnault, G. U. Nienhaus, and D. Bourgeois, "Structural basis of x-ray-induced transient photobleaching in a photoactivatable green fluorescent protein," Journal of the American Chemical Society, vol. 131, no. 50, pp. 18063–18065, 2009.

[124] A. F. Bell, D. Stoner-Ma, R. M. Wachter, and P. J. Tonge, "Light-driven decarboxylation of wild-type green fluorescent protein," Journal of the American Chemical Society, vol. 125, no. 23, pp. 6919–6926, 2003.

[125] R. M. Wachter, M.-A. Elsliger, K. Kallio, G. T. Hanson, and S. J. Remington, "Structural basis of spectral shifts in the yellow-emission variants of green fluorescent protein," Structure, vol. 6, no. 10, pp. 1267–1277, 1998.

[126] B. J. Bevis and B. S. Glick, "Rapidly maturing variants of the discosoma red fluorescent protein (dsred)," Nature biotechnology, vol. 20, no. 1, pp. 83–87, 2002.

[127] B. P. Cormack, R. H. Valdivia, S. Falkow, et al., "Facs-optimized mutants of the green fluorescent protein (gfp).," Gene, vol. 173, no. 1 Spec No, p. 33, 1996.

[128] M. Booth and T. Wilson, "Low-cost, frequency-domain, fluorescence lifetime confocal microscopy," Journal of microscopy, vol. 214, no. 1, pp. 36–42, 2004.

[129] B. G. Pinsky, J. J. Ladasky, J. R. Lakowicz, K. Berndt, and R. A. Hoffman, "Phase-resolved fluorescence lifetime measurements for flow cytometry," Cytometry, vol. 14, no. 2, pp. 123–135, 2005.

[130] H. Brismar, O. Trepte, and B. Ulfhake, "Spectra and fluorescence lifetimes of lissamine rhodamine, tetramethylrhodamine isothiocyanate, texas red, and cyanine 3.18 fluorophores: influences of some environmental factors recorded with a confocal laser scanning microscope.," Journal of Histochemistry & Cytochemistry, vol. 43, no. 7, pp. 699–707, 1995.

[131] X. Zhu and W. Min, "Frequency-domain phase fluorometry in the presence of dark states: A numerical study," Chemical Physics Letters, vol. 516, no. 1, pp. 40–44, 2011.

[132] J. P. Brody, P. Yager, R. E. Goldstein, and R. H. Austin, "Biotechnology at low reynolds numbers," Biophysical Journal, vol. 71, no. 6, pp. 3430–3441, 1996.

Appendix A

Mathematica Code for Designing Microfluidic Geometries

The following code was created in mathematica from the equations found in the paper "Biotechnology at low Reynolds Numbers" by Brody et al. [132]. It is used by iteratively changing the channel geometries until the target running pressure (≈1-2 psi) is achieved for the given cell velocity (5 mm/s, in our case).

2 D device

Resistance:

R = Resistance (in units of $N\,s\,m^{-5}$)
η = Viscosity (in units of $N\,s\,m^{-2}$)
x = Channel Length (in units of m)
w = Channel Width (in units of m)
h = Channel Height (in units of m)
Q = Flow Rate
Vmax = Max Velocity
P = Pressure (in units of *Psi*)

NB: Widths are assumed to be independent of x. In cases where this is not true (channels are tapered) the average of the channel width is used and this is denoted by a subscript of "2".

```
R[x_, w_, h_] := 12 η x / (h^3 w)
```

```
η = 0.0089
```

```
0.0089
```

Resistance of center input channel :

```
h1 = 25 × 10^-6 ;
xc = 19.286 × 10^-3;
xc2 = 0;
wc = 100 × 10^-6;
wc2 = 0;
```

```
Rc = N[R[xc, wc, h1]]
```

$$1.318236672 \times 10^{15}$$

Resistance of side input channels :

```
xs = 26.328 × 10^-3;
xs2 = 2.9995 * 10^-3;
ws = 150 × 10^-6;
ws2 = N[(ws + (100 * 10^-6)) / 2];
```

```
Rs = N[R[xs, ws, h1] + R[xs2, ws2, h1]]
```

$$1.3637317632 \times 10^{15}$$

Total input resistance :

```
Rinput = 1 / (1 / Rc + 2 / Rs)
```

$$4.4940726108911956 \times 10^{14}$$

Resistance of mid - section

```
xm = 1.032 × 10^-3;
```

```
wm = 150 × 10^-6;
```

```
Rm = N[R[xm, wm, h1]]
```

$4.702617600000001 \times 10^{13}$

Resistance of outputs :

```
xo = 25.9497 × 10^-3;
xo2 = 2.1213 * 10^-3;
wo = 200 × 10^-6;
wo2 = (wo + (100 * 10^-6)) / 2;
```

```
Ro = N[R[xo, wo, h1] + R[xo2, wo2, h1]]
```

$9.835203456 \times 10^{14}$

Total Output resistance :

```
Routput = Ro / 2
```

$4.917601728 \times 10^{14}$

Total Device Resistance :

```
TotalDeviceResistance = N[Rinput + Rm + Routput]
```

$9.881936098891195 \times 10^{14}$

Necessary Pressure for velocity of (input below) :

```
Vmax = 0.005;
```

In Hele - Shaw limit :

```
Q[h_, w_, v_] := 2 h w v / 3
```

```
FlowRate = N[Q[h1, wm, Vmax]]
```

$1.2499999999999997 \times 10^{-11}$

```
P = FlowRate * TotalDeviceResistance / 6894.7
```

```
1.7915819576796657
```

Appendix B

Microfluidic Cleaning and Setup Procedure

B.1 General Rules

•No microfluidics or any part of the device holder can leave the optics table tent without being sealed in a jar. They can never be exposed to ambient air.

•Never touch any microfluidics or any parts of the device manifold (white manifold, "o" rings, and orange rubber stoppers) with anything other than tweezers.

•Make sure that the water level of the sonicator is never higher than the lids of the containers since they are not water proof jars. However, keep the water level at minimum level indicated on sonicator tank.

•If you need to change the liquids in the reservoirs, use tweezers and put the orange stoppers into their water jar. The metal lid and screws do not go into the water jar.

•Try to never use high pressure (>20 PSI). With high pressure more debris will likely appear.

•Every liquid (except cells) goes through 0.2 μm filter

•Ultrapure water does not need to be filtered for cleaning purposes but does need to be filtered if being pumped through the microfluidic.

•Refrigerate any solutions other than bleach and water.

•Use a new syringe and filter each day.

•Never store anything other than glass chips in bleach solutions.

•If liquid backs up into the tubes, disconnect them from the device but leave them connected to the pressure controllers and run air through them at high pressure until dry.

•If you need to use new tubes or want to clean the tubes, cut them to the required length and sonicate them in ultrapure water for >40 minutes in a sealed jug. Then, attach them to the 20 PSI air (on microscope) and run air through them to dry them out for >20 min.

•Fill reservoirs with ¡ 150 μL of solution.

•Fill and empty reservoirs using micropipettes.

B.2 Pre-Run

•Sonicate the device in the same ≈10% bleach solution that it was stored in overnight for 40 minutes.

•Simultaneously sonicate the jar of "o" rings and orange rubber stoppers (could add a small amount of alconox before).

•Hold the jar with the manifold and ultra pure water (could add a small amount of alconox before) in the sonicator for a few minutes (do not want it to change temperature though, temperature swings will distort the plastic (Kel-F) manifold).

•Rinse white manifold three times with ultrapure water (leave third rinse water in container to store manifold in when experiments are over).

•Rinse the "o" rings and stoppers three times with ultrapure water and then leave them in third aliquot of water.

•Remove the microfluidic from the jar with tweezers and hold it over the waste bucket to rinse off with the ultrapure water.

•Put microfluidic into bottom of metal device holder.

•Place "o" rings on manifold with tweezers.

•Place manifold on top of microfluidic.

•Screw manifold retaining ring on.

•Fill reservoirs with ≤150 μL 0.2 μm filtered ultrapure water.

•Place stoppers into holes with tweezers.

•Attach metal lid with two screws (can be done without tweezers).

•Clean outsides of device interrogation region (top and bottom) with pink objective cleaner and/or MeOH with lens tissue (after it is mounted so that ports are covered!) so that lasers to not scatter from possible dirt.

•Pump water through device at 10-20 PSI for 5-10 minutes.

•Replace water with BSA-containing (if running cells) buffer solution (at this point, bubbles should not have appeared and so the device is primed and you should not use or need to use >2 PSI for buffer solutions or any solutions with proteins/cells in them) and pump buffer solution at 2 PSI for >30 min. Throughout this procedure "buffer" refers to the desired running buffer chosen according to the sample one is running (*e.g.* cells or beads). If running beads, the buffer solution is 20% w/v glycerol/ultrapure water and should NOT contain BSA.

•Empty outlets.

•Read to run! (remember to filter cells with 40 μm filter and buffers with 0.2 μm filter).

•If you want to recover the cells after the experiment, load the outlet reservoir ("keep" reservoir) with 75 μL phenol-containing cell media.

B.3 Post-Run

•Remove cells.

•Run buffer through device for 5-10 minutes to try and get rid of as many cells as possible at 2 PSI.

•Empty outlets.

•Replace buffer with water and run for ≈10 min at 10-20 PSI.

•Empty outlets.

•Replace water with 100% filtered bleach from bottle (use a different pipette tip each time you dip into bleach bottle) and run ≈10 minutes at 10-20 PSI.

•Empty inlets and outlets.

•Disassemble device holder and all parts of manifold except stainless steel quick connects.

•Put microfluidic into its conical tube with new ≈10-20% bleach solution (filtered bleach and ultrapure water, neither of which need to be re-filtered at this point).

•Sonicate for 40 minutes (can put on timer and leave overnight in sonication bath).

•Everything else is stored in water overnight with possible addition of alconox. Bleach will cause rust to metal and degrade rubber so never leave these parts in bleach for any length of time longer than ≈10 min.

Appendix C

Microfluidic Fabrication Procedure

C.1 General Procedure

The microfluidic devices are made by first anodically bonding 2 in diameter silicon wafers to 2 in diameter pyrex glass wafers ($\approx$ 1.78 mm thick). These pieces are then sent to a commercial polishing facility which polishes the unit down to 1.78 mm plus 25 μm (the final thickness of the silicon. The silicon is then masked and etched to create the channels. The holes for the channel ports are drilled in the top piece of glass (which may have the silicon channels or not depending on the desired final configuration of detection). The unit is then anodically bonded to a second pyrex wafer of desired thickness.

C.2 Anodic Bonding

•Soak pyrex and silicon wafers in Piranha etch solution at 65° C for >30 min in clean room.

•Rinse pyrex and silicon wafers in ultra pure water in clean room.

•Rinse pyrex and silicon wafers in ethanol in clean room.

•Dry wafers with nitrogen air stream in clean room.

•Place glass wafer on top of silicon wafer in clean room.

•Keep wafers in contact and bring to anodic bonding setup and align as shown in Figures C.1, C.2, and C.3.

•Raise temperature on brass slab to >270° C and then begin raising the voltage 100 V at a time (making sure that the current stays < 1 mA) until it is at 1000 V. Then wait until Newton's

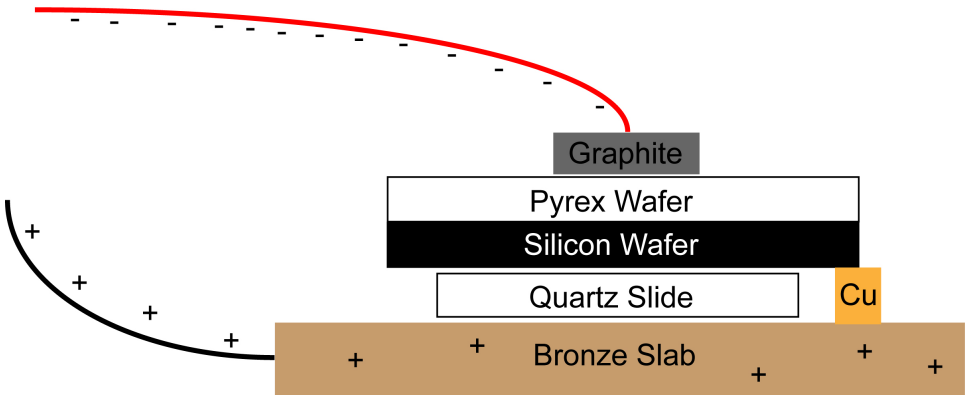

Figure C.1: Anodic bonding setup.

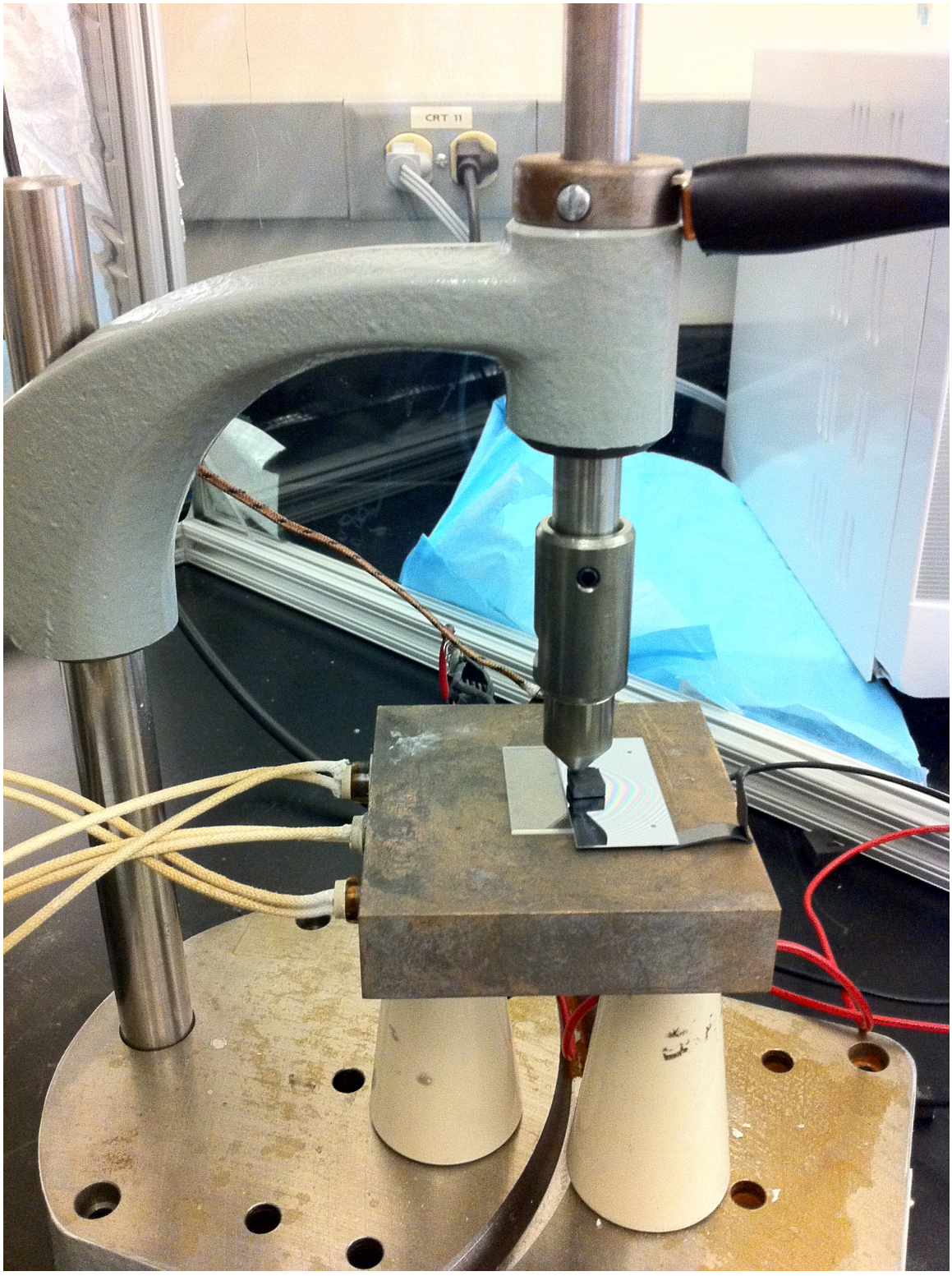

Figure C.2: Anodic bonding setup.

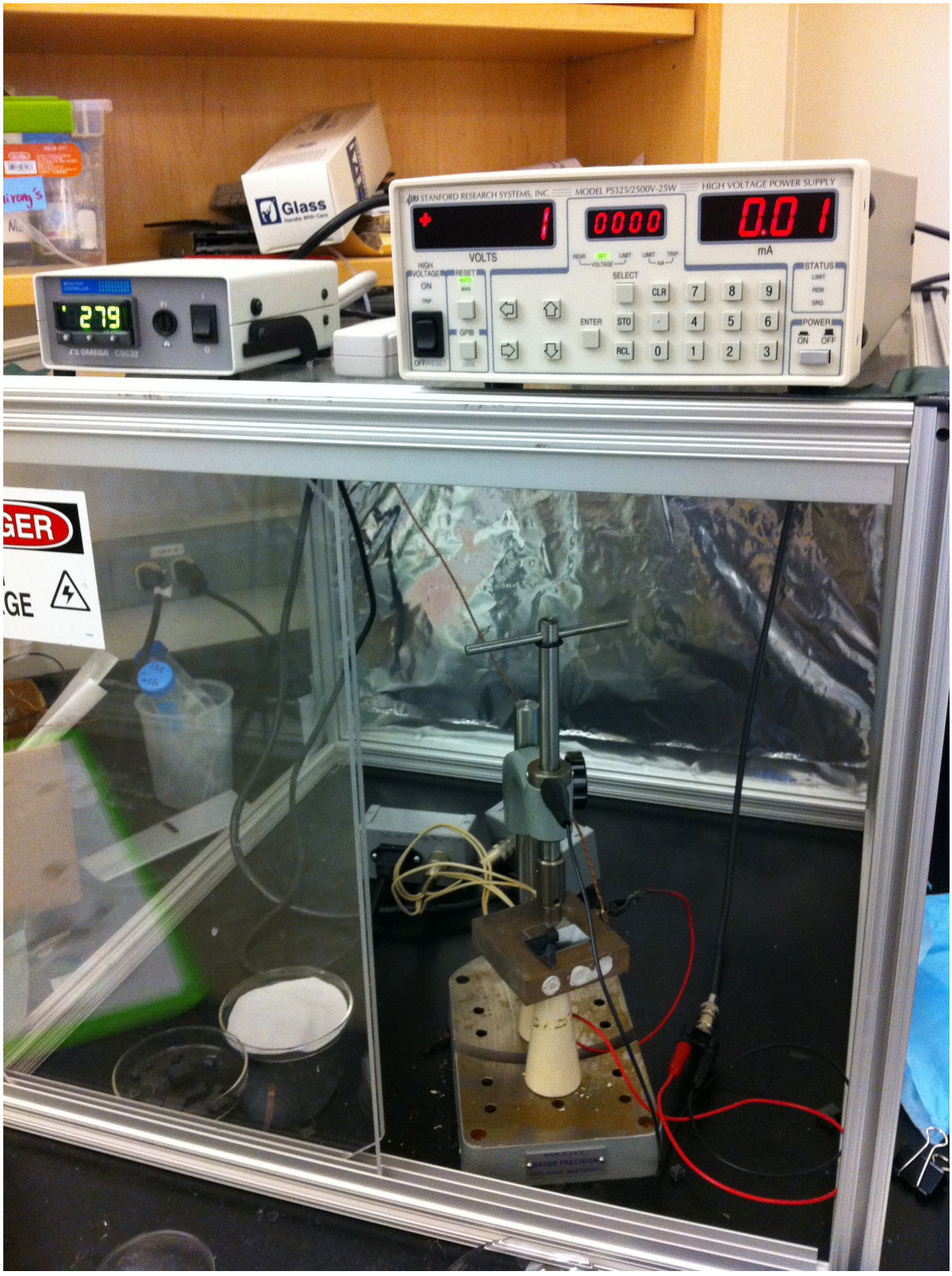

Figure C.3: Anodic bonding setup.

rings disappear.

•Turn off temperature controller and let cool.

C.3 Etching Channels

•Soak pyrex/silicon unit in Piranha etch solution for >30 min at 65° C in clean room.

•Rinse pyrex and silicon wafers in ultra pure water.

•Rinse pyrex and silicon wafers in ethanol.

•Dry wafers with nitrogen air stream.

•Follow manufacturer's instructions for coating with SU-8 2015 (MicroChem). Bake device at 200° C for 2 min to evaporate residual water.

•Center and mount device (silicon side up) on spin coater and dispense a few milliliters of SU-8 2015 (MicroChem) on top. Follow directions to achieve a final thickness ≈38 μm (spin at 500 RPM for 10 s then 1000 RPM for 30 s).

•Continue to follow manufacturer's instructions. Pre bake on hotplate at 65° C for 2 min.

•Soft bake on hotplate at 95° C for 2 min.

•Let cool.

•Cover with channel mask and expose with UV for 30 s (follow clean room procedure for aligning wafers and masks).

•Post bake on hotplate at 65° C for 1 min.

•Post bake on hotplate at 95° C for 3 min.

•Rinse in SU-8 developer until channels are dissolved.

•Etch away channels in REI etcher according to clean room procedure. Use SF_6 flow rate of 22 at 450 W. Continue etching until all of the silicon is removed from the channels when examined under a microscope (≈1.5 hrs).

•Remove remaining SU-8 by soaking device in Remover PG with heat.

C.4 Drilling Port Holes

•Bond a sacrificial cover glass to a piece of aluminum and then bond the 2 in pyrex wafer onto that cover glass using crystal bond.

•Create water dam with putty (modeling clay) and fill with rustlick.

•Drill holes using diamond core bit ($\approx$ 1 mm diameter) held in sensitive chuck on mill. Do not cut into aluminum (it will ruin the bit). Unclog the bit after each hole with wire or sonicator. Drill with short taps using fingers to lower the sensitive chuck.

•Use hotplate to release crystal bond when finished and use acetone to clean remaining crystal bond.

Appendix D

Electrical Diagrams

D.1 Custom Operational Amplifier

V1

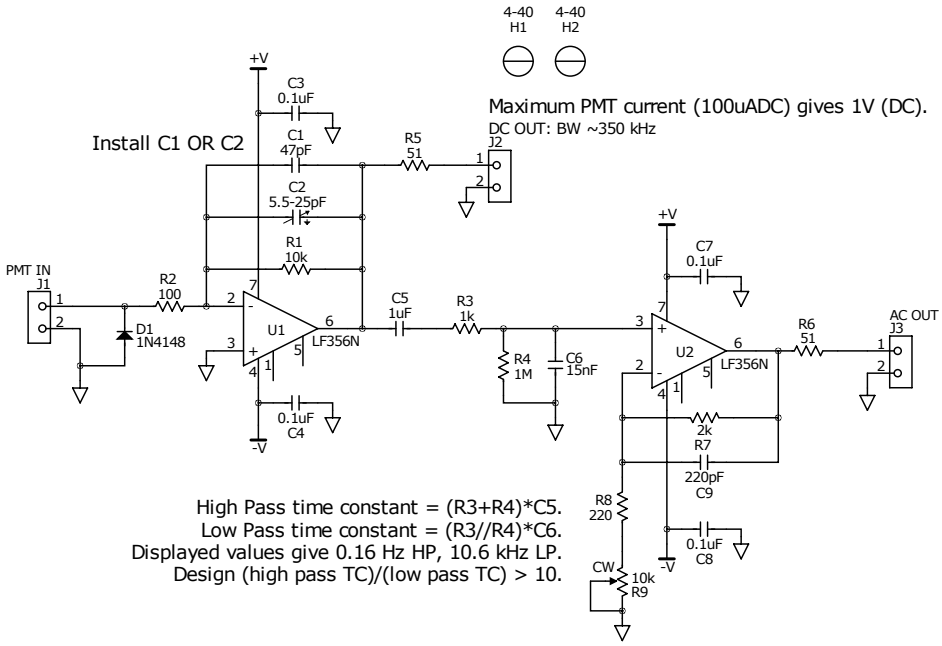

Maximum PMT current (100uADC) gives 1V (DC).
DC OUT: BW ~350 kHz

High Pass time constant = (R3+R4)*C5.
Low Pass time constant = (R3//R4)*C6.
Displayed values give 0.16 Hz HP, 10.6 kHz LP.
Design (high pass TC)/(low pass TC) > 10.

LF356 gives 500kHz BW at gain 10.
For 3 MHz BW use AD825 with a SOIC8 to DIP8 adapter.

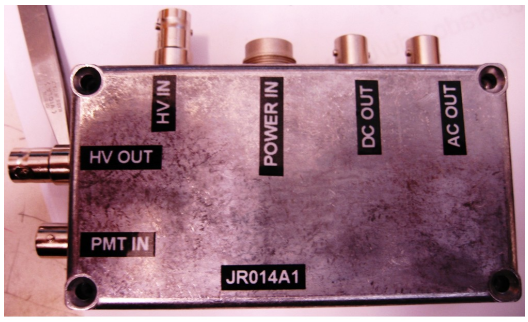

MOUNTED IN A CU-124 BOX
JILA #: 0211

Power Input Connector:
Lumberg PN: SFV50, JILA #: 2550
+V: PIN 1
RTN: PIN 4
-V: PIN 2

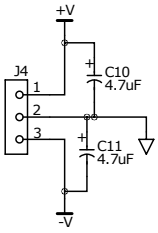

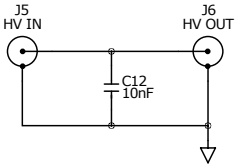

SOLDER SIDE VIEW

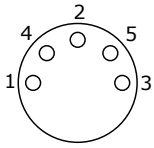

JILA ELECTRONICS LAB		
PMT Transimpedance Amplifier		
DESIGN BY: T. Brown		BUILT FOR: Jimemez / Gibson
UPDATE: 12/16/2008	VERSION: V1	DRAWN BY: T. Brown
DN: JR014A1	DATE: 12/02/2008	SHEET 1 OF 1

D.2 Custom I/Q Demodulator

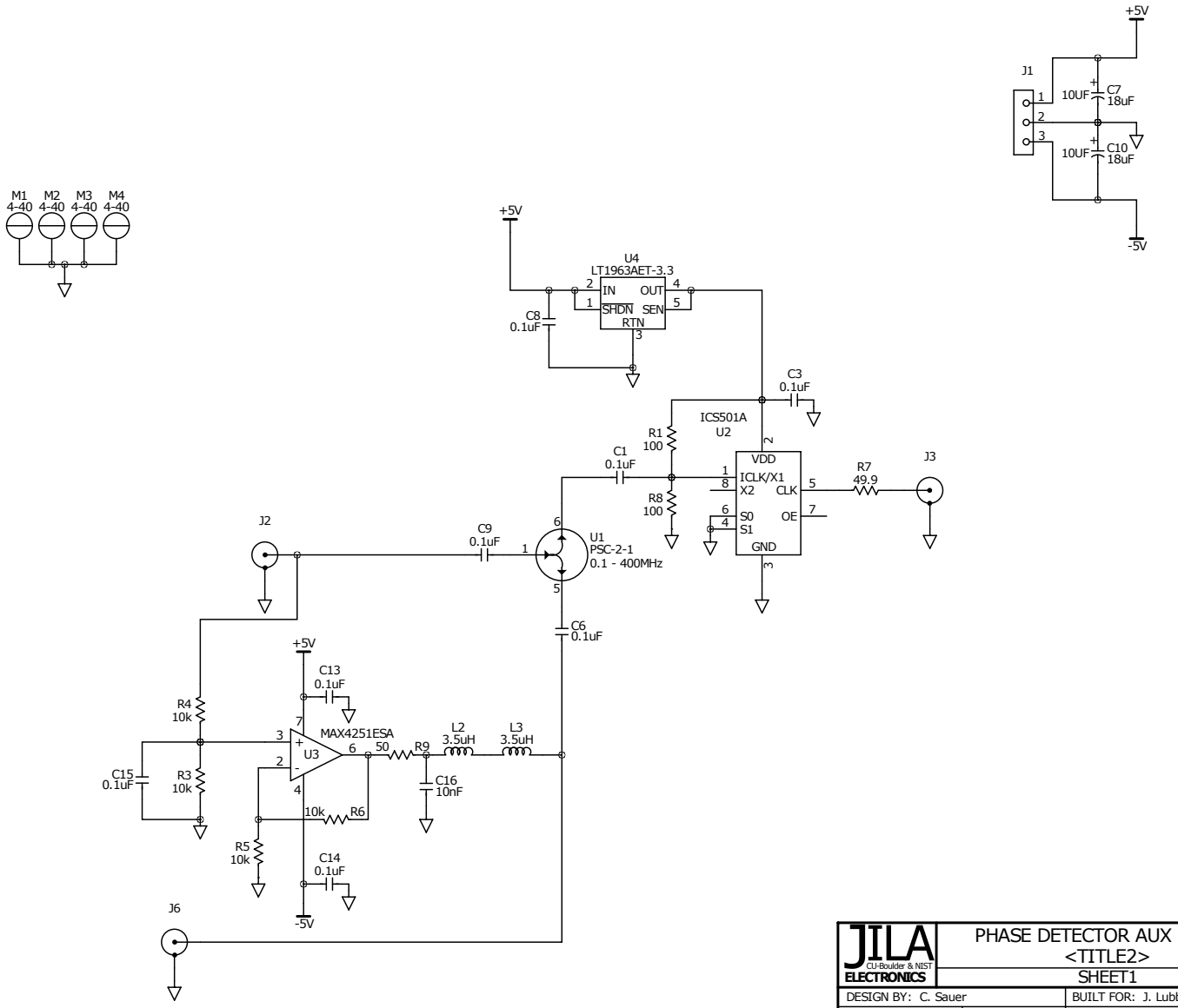

JILA CU-Boulder & NIST ELECTRONICS	PHASE DETECTOR AUX BOARD <TITLE2>	
	SHEET1	
DESIGN BY: C. Sauer		BUILT FOR: J. Lubbeck
UPDATE: 5/18/2012	VERSION: A2	DRAWN BY: CS
DN: JR021	DATE: 5/2012	SHEET 1 OF 1